

2011-01-01

Microstructural Architecture Developed In The Fabrication Of Solid And Open-Cellular Copper Components By Additive Manufacturing Using Electron Beam Melting

Diana Alejandra Ramirez

University of Texas at El Paso, daramirez2@miners.utep.edu

Follow this and additional works at: https://digitalcommons.utep.edu/open_etd



Part of the [Materials Science and Engineering Commons](#), and the [Mechanics of Materials Commons](#)

Recommended Citation

Ramirez, Diana Alejandra, "Microstructural Architecture Developed In The Fabrication Of Solid And Open-Cellular Copper Components By Additive Manufacturing Using Electron Beam Melting" (2011). *Open Access Theses & Dissertations*. 2372.
https://digitalcommons.utep.edu/open_etd/2372

This is brought to you for free and open access by DigitalCommons@UTEP. It has been accepted for inclusion in Open Access Theses & Dissertations by an authorized administrator of DigitalCommons@UTEP. For more information, please contact lweber@utep.edu.

MICROSTRUCTURAL ARCHITECTURE DEVELOPED IN THE FABRICATION OF
SOLID AND OPEN-CELLULAR COPPER COMPONENTS BY ADDITIVE
MANUFACTURING USING ELECTRON BEAM MELTING

DIANA ALEJANDRA RAMIREZ

Materials Science and Engineering

APPROVED:

L.E. Murr Ph.D., Chair

S.W. Stafford, Ph.D.

F.S. Manciu, Ph.D.

R.R. Chianelli, Ph.D.

Benjamin C. Flores, Ph.D.
Acting Dean of the Graduate School

Copyright
by
Diana A. Ramirez
2011

Dedication

This would have not been possible if I did not have the support of my family, friends and co-workers and I want to take the time to dedicate this work to all of you. To my family, thank you for inspiring me always to further my studies. This is dedicated to my grandfather, Armando Olivas, who has always been someone I have looked up to as a father. To my brothers and sister let this prove you that every dream you may have is possible with hard work and dedication. Thank you to my grandmother for her continuous prayers so that everything would always work out for me. To my mother thank you for always being my # 1 fan. Life would not be the same without friends and to you all thank you for the encouraging words, support, and for always taking the time to listen. A special dedication goes to the very special people in my life who always pushed me to excel in everything I do and never let me throw the towel; Ana Laura Olivas, and Susie Martinez. In addition, I would like to dedicate this to my musketeers: Alba A. Prieto and Andrea N. Tarantino for the long hours of studying together and the support in every challenging experience I have had. Dre, thank you so much for all that you have done for me especially in those times that nothing seemed to make sense. Your words, support, and friendship made this journey possible. Finally, this accomplished dream is dedicated to my angel from heaven, my brother Jaime Ramirez.

MICROSTRUCTURAL ARCHITECTURE DEVELOPED IN THE FABRICATION OF
SOLID AND OPEN-CELLULAR COPPER COMPONENTS BY ADDITIVE
MANUFACTURING USING ELECTRON BEAM MELTING

by

DIANA ALEJANDRA RAMIREZ,
B.S. Metallurgical and Materials Engineering

DISSERTATION

Presented to the Faculty of the Graduate School of
The University of Texas at El Paso
in Partial Fulfillment
of the Requirements
for the Degree of

DOCTOR OF PHILOSOPHY

Materials Science and Engineering
THE UNIVERSITY OF TEXAS AT EL PASO
December 2011

Acknowledgements

I would like to extend special thanks to Dr. Lawrence E. Murr for his patience, guidance and support throughout my studies and the preparation of this dissertation. I would like to also express my gratitude to Dr. Stephen Stafford for his support and for being part of my committee as well as Dr. Felicia S. Manciu and Dr. R. Chianelli for critically reviewing my proposal and serving as committee members. In addition, I would like to thank the entire research group. Special thanks to Edwin Martinez, Dr. Brenda I. Machado, Dr. Sara Gaytan, and Jose Luis Martinez for their help and suggestions. Finally, I would like to add a special note of appreciation for Dr. Ryan Wicker, Mr. Frank Medina and the Keck center team for the fabrication of the Cu samples.

This research was supported by the Air Force Research Laboratory through Clarkson Aerospace Contract #UTEP-10-5567-013-02-C2 (Task Order 2.10.2). Copper EBM fabrication was also partially supported by the US Department of Energy SBIR Grant DE-SC0000867. Mr. and Mrs. MacIntosh Murchison Endowments and the University of Texas at El Paso, the Institute of Metal Research, Shenyang, China, the Chinese Academy of Science (CAS) and Mr. Pedro Frigola, RadiaBeam Technologies, Santa Monica, CA for the provision of the Cu powder.

Abstract

The fabrication of Cu components were first built by additive manufacturing using electron beam melting (EBM) from low-purity, atomized Cu powder containing a high density of Cu_2O precipitates leading to a novel example of precipitate-dislocation architecture. These microstructures exhibit cell-like arrays (1-3 μm) in the horizontal reference plane perpendicular to the build direction with columnar-like arrays extending from ~12 to >60 μm in length and corresponding spatial dimensions of 1-3 μm . These observations were observed by the use of optical metallography, and scanning and transmission electron microscopy. The hardness measurements were taken both on the atomized powder and the Cu components. The hardness for these architectures ranged from ~HV 83 to 88, in contrast to the original Cu powder microindentation hardness of HV 72 and the commercial Cu base plate hardness of HV 57.

These observations were utilized for the fabrication of open-cellular copper structures by additive manufacturing using EBM and illustrated the ability to fabricate some form of controlled microstructural architecture by EBM parameter alteration or optimizing. The fabrication of these structures ranged in densities from 0.73g/cm³ to 6.67g/cm³. These structures correspond to four different articulated mesh arrays. While these components contained some porosity as a consequence of some unmelted regions, the Cu_2O precipitates also contributed to a reduced density. Using X-ray Diffraction showed the approximate volume fraction estimated to be ~2%. The addition of precipitates created in the EBM melt scan formed microstructural arrays which contributed to hardening contributing to the strength of mesh struts and foam ligaments. The measurements of relative stiffness versus relative density plots for Cu compared very closely with Ti-6Al-4V open cellular structures – both mesh and foams. The Cu reticulated mesh structures exhibit a slope of $n = 2$ in contrast to a slope of $n = 2.4$ for the stochastic Cu foams, consistent with the Gibson-Ashby foam model where $n = 2$. These open cellular structure components exhibit considerable potential for novel, complex, multi-functional electrical and thermal management systems, especially complex, monolithic heat exchange device.

Table of Contents

Acknowledgements	v
Abstract	vi
Table of Contents	vi
List of Tables	ixx
List of Figures	x
List of Illustrations	xii
Chapter 1: Introduction	1
Chapter 2: Background	3
2.1 Background of Copper	3
2.1.1 The Cu-O Phase Diagram	3
2.2 Atomized Powder	5
2.2.1 Atomized Copper Powder	6
2.3 What is Additive Manufacturing	8
2.4 Overview of Arcam A2 Electron Beam Melting Machine	9
2.5 History of Metal Foam Fabrication and Process	13
2.6 Heat Transfer in Metal Foams	16
2.7 Research Studies of Open-Cellular and Stochastic Mesh and Foams	17
2.7.1 Novel Precipitate – Microstructural Architecture	20
Chapter 3: Experimental Procedure / Methodology	22
3.1 Analysis of powder	22
3.1.1 Flow of Copper Powder	23
3.1.2 Powder Size Distribution	24
3.1.3 Microstructural Analysis of Copper Powder	26
3.1.4 Optical Metallography and SEM Analysis of Copper Powder	28
3.2 EBM Parameters for the Fabrication of Copper Components	30
3.2.1 Fabrication of Copper Components	30
3.3 Optical Metallography on Copper Components	32
3.4 Scanning Electron Microscopy	5
3.5 Transmission Electron Microscopy	32
3.6 Fabrication of Reticulated Mesh Structures	33

3.7 Elastic Moduli (E) Testing.....	36
Chapter 4: Result and Discussion.....	39
4.1 Microstructural Analysis on Copper Components	39
4.4.1 Microstructural Analysis of rectangular block and geometry prototype components ..	49
4.2 Transmission Electron Microscopy.....	57
4.3 Open – Cellular of Cu Mesh and Foam Specimens	65
4.4 Young’s Moduli (E)	71
Chapter 5: Summary and Conclusions.....	76
References	79
Appendix	82
Curriculum Vita	106

List of Tables

Table 2.1.1: Copper Crystallographic Data.....	5
Table 2.2.2: Characteristics of Commercial Copper Powders.	9
Table 2.3.1: Technologies and Base materials for Additive Manufacturing	10

List of Figures

Figure 2.1.1: Unit cekk of the cubic structure Cuprite.	4
Figure 2.4.1: Arcam A2 EBM machine	13
Figure 2.5.1: Structure of metal foam and dodecahedron	15
Figure 2.5.2: SEM image comparison for a reticulated mesh strut microstructure (a) and stochastic open cellular foam ligament microstructure (b).....	16
Figure 2.7.1: 3D CAD model for open cellular foams	20
Figure 3.1.1: Vacuum powder and precursor air –exposed powder.....	25
Figure 3.1.2: Measurement of particle size distribution	26
Figure 3.1.3 Precursor copper particle distribution.	27
Figure 3.1.4: Precursor copper powder SEM.....	28
Figure 3.1.5: Precursor copper powder particle internal microstructure for embedded, ground, polished, and etched particles.....	30
Figure 3.2.1: Examples of components and component (build) geometries fabricated by EMB.	33
Figure 3.6.1: Schematic showing software (CAD) using Materialized dode-thin mesh build.	36
Figure 3.6.2: Examples of Open cellular mesh foam specimens fabricated from CAD.....	37
Figure 4.1.1: Optical representation of microstruture in horizontal direction for components. ...	40
Figure 4.1.2: 3D image composite representing a section of the cylindrical components.	41
Figure 4.1.3: 3D image composite representing a typical section from cylindrical components.	43
Figure 4.1.4: XRD Spectra of Cu ₂ O	45
Figure 4.1.5: SEM views of regular, cube/rectangular etch pits corresponding to elongated cell-like structures.....	46
Figure 4.1.6: SEM views (A and B) for etch pits characterizing Cu ₂ O column-like architectures in the vertical plane parallel to the build direction.....	47
Figure 4.1.7: Optical and SEM images representing the Cu ₂ O precipitate showing etching details for the cellular columns composed of Cu ₂ O precipitates in the horizontal plane..	48
Figure 4.1.8: EBM scan geometry ideally forming precipitate-dislocation architectures in fabricated Cu components.....	50
Figure 4.1.9: Optical Microscopy image 3D composite section from rectangular block.....	51
Figure 4.1.10: Higher Magnification 3D image of rectangular block.	52
Figure 4.1.11: Spatial composite showing horzntal reference plane	53
Figure 4.1.12: Section from Copper component illustrating surface structure.	55
Figure 4.1.13: Typical grain and sub-grain spatial precipitate-dislocation arrays in the horizontal reference plane.....	56
Figure 4.2.1: Illustrates TEM bright-field image showing precipitation-dislocation arrays corresponding to the horizontal reference.....	58
Figure 4.2.2: Magnified TEM bright-field image showing horizontal reference plane precipitate-dislocation array microstructure.	60
Figure 4.2.3: TEM bright-field image showing precipitate-dislocation architecture features in the vertical reference plane selective etching at precipitates.	61
Figure 4.2.4: TEM bright-field image in the vertical plane.....	63
Figure 4.2.5: Illustrates TEM bright-field image in the horizontal plane.....	64
Figure 4.3.1: Reticulated mesh structures in comparison to stochastic open cellular foam and “solid build”.	66
Figure 4.3.2: Comparison of EMB fabrication non-isotropic-geometry for reticulated mesh.....	67

Figure 4.3.3: Horizontal and vertical plane constructions typical of reticulated mesh strut microstructure (a) and stochastic foam ligament microstructure.	69
Figure 4.3.4: TEM bright-field image for horizontal plane microstructural arrays observed in the “solid” sample.	70
Figure 4.4.1 Stiffness (E) vs density (ρ) for Cu and relative stiffness (E/E_0) versus relative density (ρ/ρ_0) for Cu and Ti-6Al-4V	72
Figure 4.4.2: SEM image comparison for a reticulated mesh strut microstructure and stochastic open cellular foam ligament microstructure.	74
Figure 4.4.3: SEM micrograph showing impact-shear fractography views for mesh strut and foam ligament fracture surface.	75
Figure 5.1: 3 Novel property-performance an extension for the materials, science and engineering paradigm: structure – properties – processing – performance plus architectures.	77

List of Illustrations

Illustration 1.1.1: Cu-O Phase Diagram.....	6
Illustration 2.2.1: Schematic of Atomization Process.....	7

Chapter 1:

Introduction

The necessity of having new materials that can have the capabilities of low densities, light-weight structures, energy absorption, thermal applications and high mechanical properties has given additive manufacturing by Electron Beam Melting (EBM) opportunity to rise as one of the technologies capable of creating such structures. The physical property of the metal foam structures makes of this technology a fundamental solution to the thermal management problems. This form of fabrication does not only offer great properties, but it also offers the opportunity to be cost effective. Currently additive manufacturing has shown prosperous advances in the aerospace and biomedical industry. This has involved the creation of complex functional (biocompatible) mesh arrays as well as other custom designed components.

In this research work, the fabrication of complex copper mesh and open cellular foams fabricated by additive manufacturing using EBM for the future use of its thermal applications are examined. Furthermore, we illustrate the mechanical and physical properties of copper mesh and foams prototypes, and prospects for applications to advance heat exchange devices, and the thermal applications of open cell metal foams. In addition, the use of optical microscopy scanning and transmission electron microscopy will allow for explanation of innovative observations of the microstructural architecture composed of Cu_2O precipitate columns in the EBM build direction. The component microstructure exhibits a novel Cu_2O precipitate columnar architecture. The precipitation- related columnar architecture was unintended and occurred as a consequence of oxygen in the manufactured Cu powder. Nonetheless, this occurrence provided a unique opportunity to observe and characterized a new directional

solidification phenomenon. In addition, this will be the first direct fabrication of Cu open cellular structures. The measurements of density, stiffness plots of relative stiffness versus relative density will allow copper open cellular structures to be compared with classical foam models described by Ashby.

Chapter 2:

Background

2.1 BACKGROUND OF COPPER

Copper has very attractive properties that make the metal useful for many applications such as excellent corrosion resistance, outstanding workability, good mechanical properties, toughness, antimicrobial properties, and electrical and thermal conductivity. The thermal conductivity of copper, 394W/mK, is approximately twice that of aluminum and thirty times that of stainless steel, which allows for a broad area where copper can be useful such as in components where rapid heat transfer is vital. Examples include saucepan bottoms, heat exchangers, car and vehicle radiators and heat sinks in computers, disk drives and TV sets. The main advantage of copper is its low electrical resistivity and high resistance to electro-migration and stress-migration, when compared with aluminum.

2.1.1 The Cu-O Phase Diagram and Crystal Structure

Copper has primarily three phases that appear in the Cu-O phase diagram are Cu_2O (Cuprite), Cu_4O_3 (paramelaconite), and CuO (tenorite) as shown in the Illustration 2.1.1. Table 2.1.1 shows the crystallographic data of the three different phases. The Cu_2O shown in figure 2.1.1 with 2:4 coordination. The oxygen atoms are located at the corners and center of the unit cell, and the copper atoms with the copper atoms occupying the center of four of the eight corners into which the cell may be divided. This arrangement is cubic close packing. The structure has an oxygen atom co-ordinated by four copper neighbors at each corner of a regular tetrahedron; however, each copper atom has only two oxygen neighbors symmetrically on a straight line as shown in figure 2.1.1.

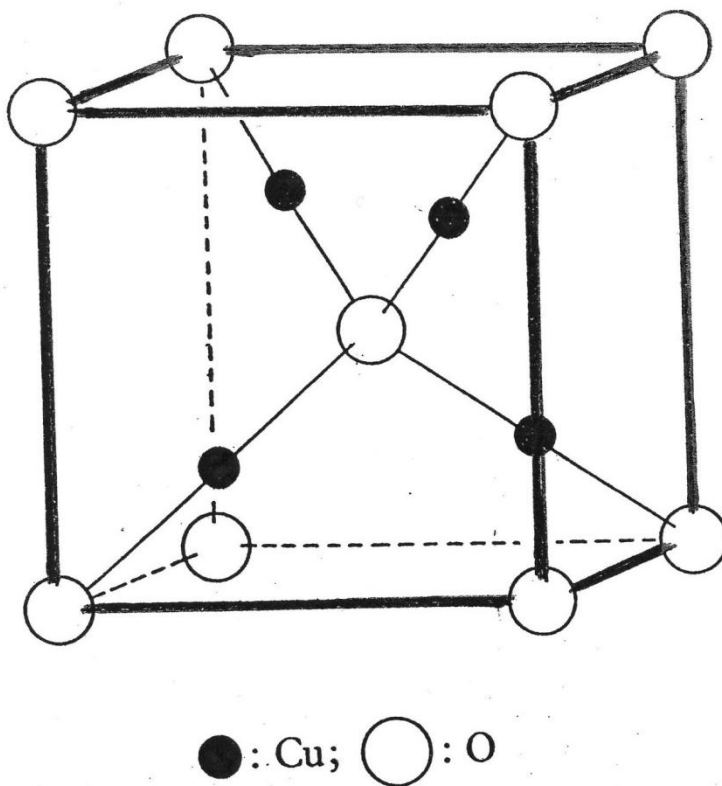


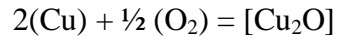
Figure 2.1.1 Unit cell of the cubic structure of Cu_2O , cuprite.

This structure is very unique because it consists of two identical interpenetrating frameworks that are not directly bonded together: any one atom can reach half, but only half of the other atom in the Cu-O bond.

Thus the bond can be formulated as in Cu_2O :



The affinity of copper for oxygen is often so great, that even under the most stringent inert environments, the copper particles will include some oxygen. The oxidation of copper is a well known process. The reaction of the copper oxide formation can be represented by as follows:



The retention of oxygen allows for the formation of copper oxides including Cuprite oxide, (Cu_2O), or retention of interstitial oxygen which will form Cu_2O during Electron Beam Melting (EBM). Table 2.1.1 illustrates the different phase compositions and additional information such as space group. This becomes more important and will further be analyzed in the Discussion section.

Table 2.1.1: Copper Crystallographic Data [1]

Phase	Composition Wt% O	Pearson Symbol	Space group
(Cu)	0 to 0.008	<i>cF4</i>	<i>Fm$\bar{3}m$</i>
$\text{Cu}_2\text{O}^{(a)}$	11.2	<i>cP6</i>	<i>Pn$\bar{3}m$</i>
$\text{CuO}^{(b)}$	20	<i>mC8</i>	...
Cu_4O_3	15.9	<i>tI28</i>	<i>I4/mcm</i>

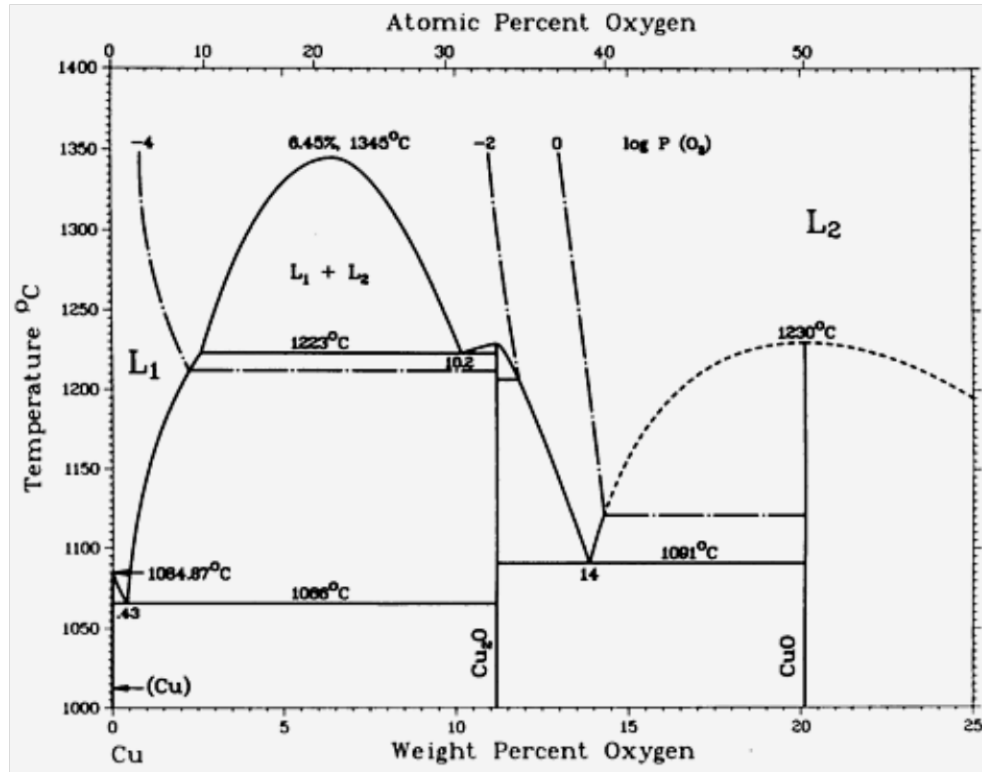


Illustration 2.1.1: Cu-O Phase Diagram [2]

2.2 ATOMIZED POWDER

In the atomization of metals, molten metal flows from a tundish through a refractory nozzle and the liquid stream is disintegrated into droplets by impact of water or gas jets [2] thus breaking the molten metal into particles which solidify fast. Inert gas atomization produces spherical particles. The particle size and shape are influenced by the atomization medium, pressure and flow rate. There is no refining during atomization or solid state reduction and the purity of the material depends on that of the raw material; however, purity is generally over 99%.

The atomization process includes different variations such as impulse atomization, oil atomization, vacuum atomization and gas atomization. Gas atomization process is the process where

“liquid metal is dispersed by a high-velocity jet of air, nitrogen, argon, or helium” [2]. This process is mostly used for the commercial production of powders of copper alloys, copper, titanium and nickel-base alloys. Air atomization is another method use for the fabrication of aluminum, zinc and copper as well. This process utilizes inert gasses when the oxygen content needs to be kept low. Illustration 2.2.1 shows a basic schematic of the different stages involved in atomization.

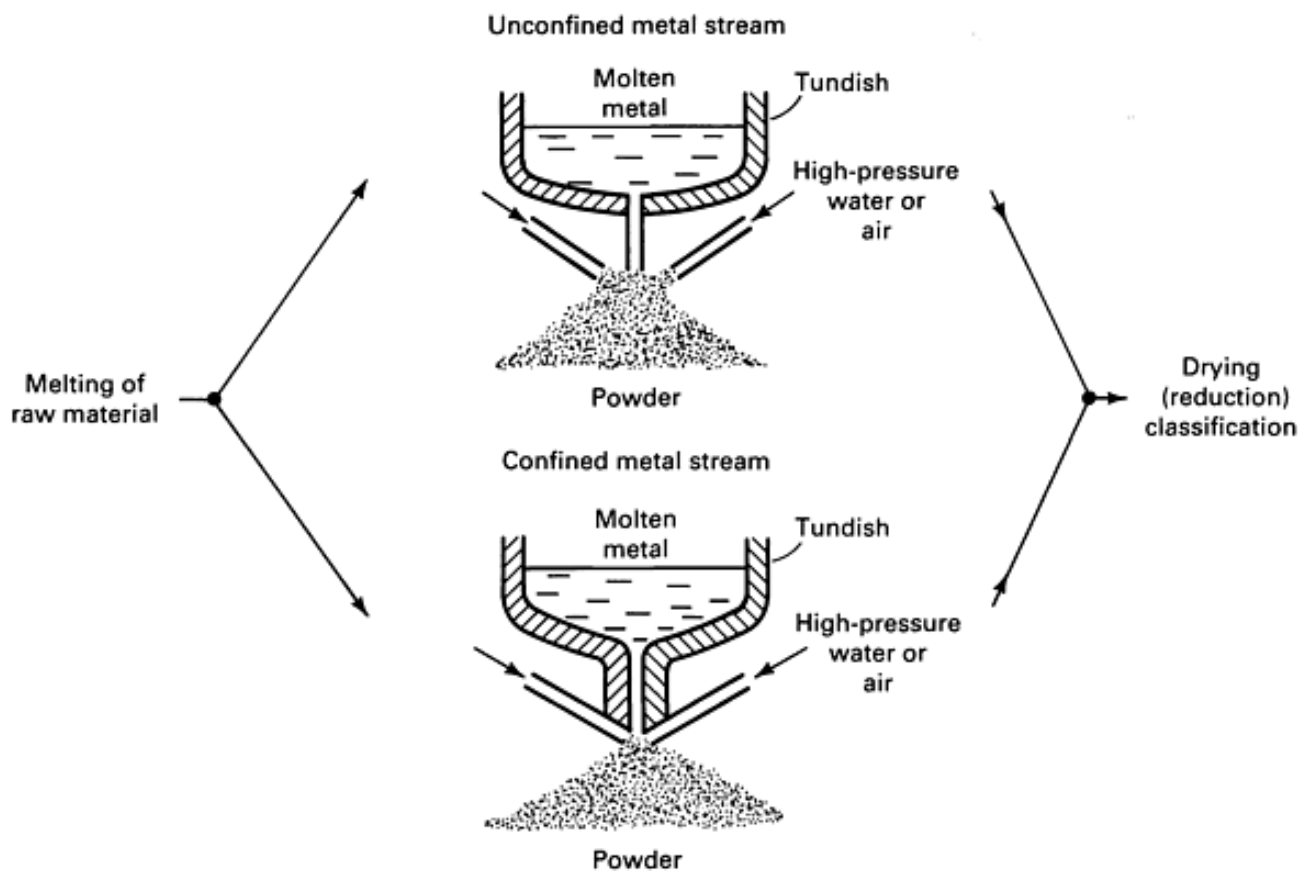


Illustration 2.2.1 Schematic of Atomization Process [3]

2.2.1 Atomized Copper Powder

The conductivity of copper is highly dependent on the impurities of oxygen free copper; oxygen of course being a major impurity. Thus it is very important to control the impurity content during melt preparation to acquire high conductivity and better fluidity. This creates the need for oxygen control because an increase in oxygen content results in the production of more irregular powder. The copper compounds are produced as powders by the controlled reaction of oxygen with copper powders. When copper is used in the as-atomized state, lower oxygen content is essential because of the effects of oxygen in many applications. Table 2.2.1 illustrates some of the fundamentals of commercial copper powders produced by different atomization processes.

Table 2.2.1: Characteristics of Commercial Copper Powders [3]

Type of powder	Composition, %			Particle shape	Surface area
	Copper	Oxygen	Acid insolubles		
Electrolytic	99.1-99.8	0.1-0.8	0.03 max	Dendritic	Medium to high
Oxide reduced	99.3-99.6	0.2-0.6	0.03-0.1	Irregular; porous	Medium
Water atomized	99.3-99.7	0.1-0.3	0.01-0.03	Irregular to spherical; solid	Low
Hydrometallurgical	97-99.5	0.2-0.8	0.03-0.8	Irregular agglomerates	Very high

2.3 WHAT IS ADDITIVE MANUFACTURING

Additive manufacturing (AM) has become an exciting and growing process in industry. It is defined by American Society for Testing and Materials as “the process of joining materials to make objects from 3D model data, usually layer upon layer” [4]. The advances in this technology have made it possible for machines to be more affordable and has allowed for the commercialization of the machines for different industries [5]. This technology allows the use of any metal in powder form.

Powder layers are melted to the exact geometry that has been established by a 3D CAD model by successively stacking selectively melted powder layer by layer. This allows for the building of very complex geometries without any sort of tools or fixtures through electron beam melting (EMB) and without producing any waste material as well. Thus, AM technology presents great benefits for the production of different components. This new technology allows the exploration of different engineering design without any manufacturing constraints due to its geometrical freedom. Moreover, this can allow the fabrication of extreme light-weight designs, reduced part counts, and even improve the ability of bone in-growth for a medical implant. Table 2.3.1 indicates the different types of techniques that are available with additive manufacturing and the base material that are used with each technique.

Table 2.3.1: Technologies and Base Materials for Additive Manufacturing [6, 7, 8]

Prototyping technologies	Base materials
Selective laser sintering (SLS)	Plastics, ceramics, metal powders
Direct Metal Laser Sintering (DMLS)	Almost any alloy metal
Fused deposition modeling (FDM)	Thermoplastics
Stereolithography (SLA)	photopolymer
Laminated object manufacturing (LOM) Paper	Paper
Electron beam melting (EBM)	all metals powders
3D printing (3DP)	Various materials

2.4 OVERVIEW OF ARCAM A2 ELECTRON BEAM MELTING MACHINE

During the EBM process, the electron beam melts the metal powder in a layer-by-layer process to build complex components. The Arcam A2 EMB machine can produce multiple parts in the same build. These parts are built in a vacuum environment at elevated temperatures and are free from residual stresses and do not suffer distortion in stress-relieved parts with material properties better than cast and comparable to wrought material. The electron beam high power guarantees a high rate of deposition and an even temperature distribution within the part, which gives a fully melted metal with excellent mechanical and physical properties. This is due to the fact that the beam is managed by electromagnetic coils rather than optics in the case of a laser beam, and moving mechanical parts which allows a superior beam control and very fast beam translation. Figure 2.4.1 illustrates a schematic of the Arcam EMB used to fabricate components in this research.

This operating system is very similar to that of an electron beam welding system. The current is approximate 10A (DC) that drives a tungsten filament in the electron gun operating at an anode potential of 60kV, referred to as number 1 in figure 2.4.1. The electromagnetic lenses utilized to focus the electron beam and the scanning coils are reference by 2 and 3 respectively. In 4, are the two powder cassettes located at each side of the system that feed the building table, 7, allows to provide uniform layer of copper powder. 5 shows where the rake is located at the designed component is built into a solid form in the building chamber noted by number 6. The build chamber mechanism is under a vacuum of $\sim 10^{-4}$ Torr and in normal building it uses helium gas bleed at $\sim 10^{-2}$. This allows easier build cooling and thermal stability. As previously mentioned, the melt scan only melts the desired sections of the powder layer. This is due to the fact that the melt scan is driven by a three dimensional 3D computer aided design (CAD) program. Before melting the powder, the machine preheats the layer by scanning the

beam ~11 times at a velocity of ~15,000 mm/s followed by melt scan at 400mm/s. The desired temperature is maintained uniform throughout the entire process.

The advantage of fabricating structural materials by additive manufacturing using EBM can allow for the development of properties, processing and performance features can be manipulated in the desired microstructures. The most common metal foams fabricated have been with aluminum or aluminum alloys metals by liquid or semi liquid foaming technologies. This will be analyzed more in the Discussion section.

Copper is an exceptional candidate for the fabrication of open-cellular mesh and foam structures because of its high thermal conductivity at a given temperature. The rate of heat transfer is dependent upon the temperature gradient and the thermal conductivity of the metal or material. At a given temperature, thermal and electrical conductivities are proportional, thus; raising the temperature increases the thermal conductivity and decreases the electrical conductivity. This becomes very important in the fabrication of open-cellular metal core sandwich panel wingskins for aeronautic or aerospace applications.

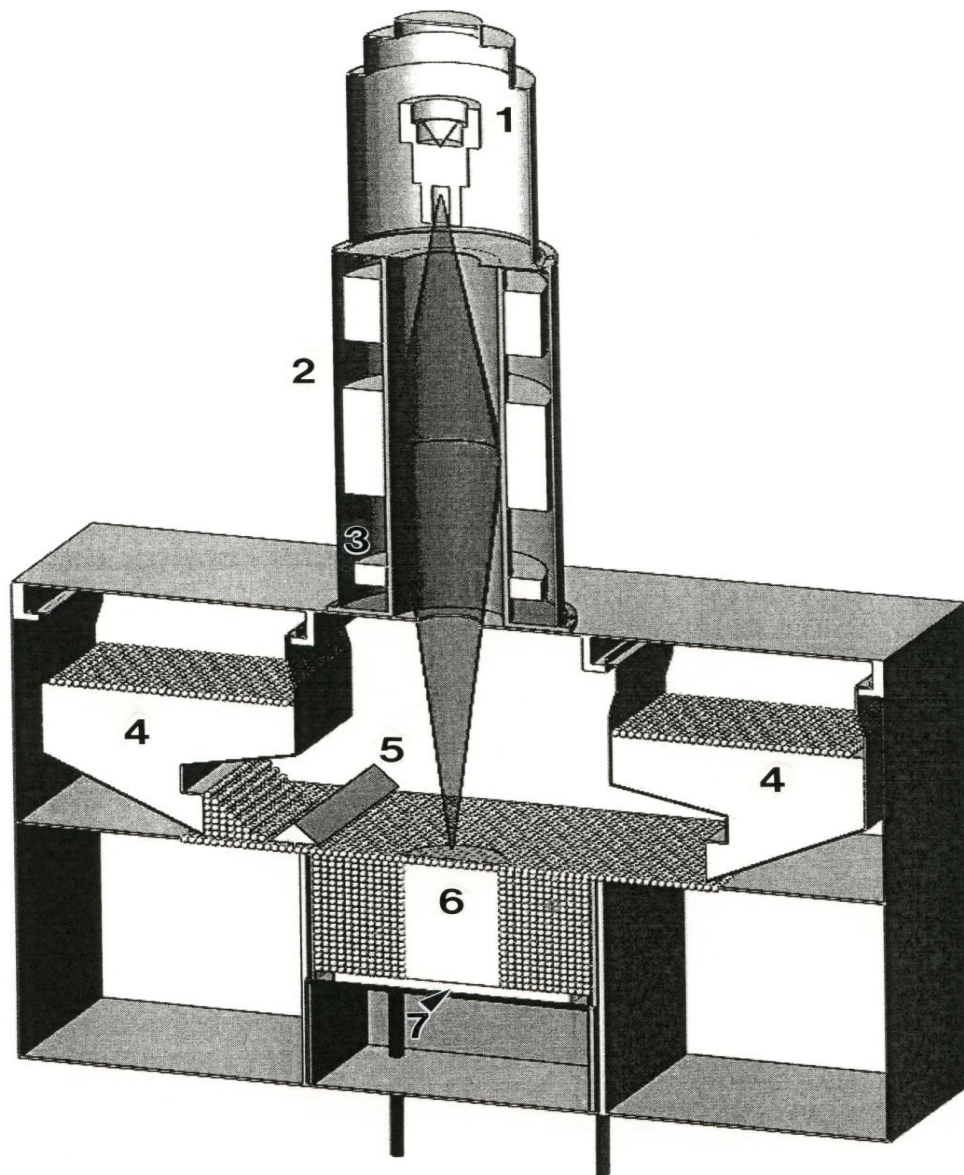


Figure 2.4.1. Arcam A2 EBM facility it is gravity fed from cassettes and raked into a layer $\sim 100\mu\text{m}$ where the focused electron beam rasters to pre-heat the layer and finally melt prescribed areas.

2.5 HISTORY OF METAL FOAM FABRICATION AND PROCESS

Recently the need to fabricate different components with more complex geometries and used in potential applications has allowed for many rapid prototyping (RP) techniques for metals. Metal foams have been fabricated in the past two decades using a variety of novel techniques. Metallic sintering, metal deposition through evaporation, chemical vapor decomposition (CVD) or electrodeposition, are some of the technologies that have created open cell foams. Other techniques used to fabricate metal part with complex geometries and faster builds are EMB, Electron Beam Solid Freeform Fabrication (EBSFF), Epitaxial Laser Metal Forming (E-LMF), Laser Engineered Net Shaping (LENS) and Sprayforming. These techniques have indicated to melt the metal material melts locally which allows for a “small volume to melt and solidify within a short period of time” [9].

Open-cell metal foams have very complex geometries consisting of small filaments of ligaments structures and cell structures. They are used to fabricate lightweight structures to develop energy absorption devices and for thermal applications as a result of their thermal, mechanical, and electrical properties. The base metal used for the fabrication of the foam will determine the properties of the foam such as the strength and the relative density. The foam properties are also influenced by anisotropy as well as structural defects. Other properties that can influence different characteristics such as heat transfer are; pore size, strut or ligament size and cell shape can influence certain characteristics. Pore size and relative density are two characteristics that are fundamental to identify for a foam material and for the applications giving flexibility in product design. Relative density is defined as the percentage of the solid material, ρ/ρ_s , where ρ_s is the solid density and whether the foam has open or closed cells. It is the volume of solid foam material relative to the total volume of metal foam. Figure 2.5.1 is a picture of the metal foams and mesh structures. Porosity is highly desirable for weight, cost reduction, improving

specific strength and thermal characterization. Porosity is also important very important when dealing with structural applications.

The foam structure consists of ligaments forming a network of inter- connected dodecahedral-like cells which are randomly oriented and mostly homogeneous in shape and size. Figure 2.5.1 and 2.5.2 can be used to illustrate the ligament connection and dodecahedron having 12 pentagon shape facets.

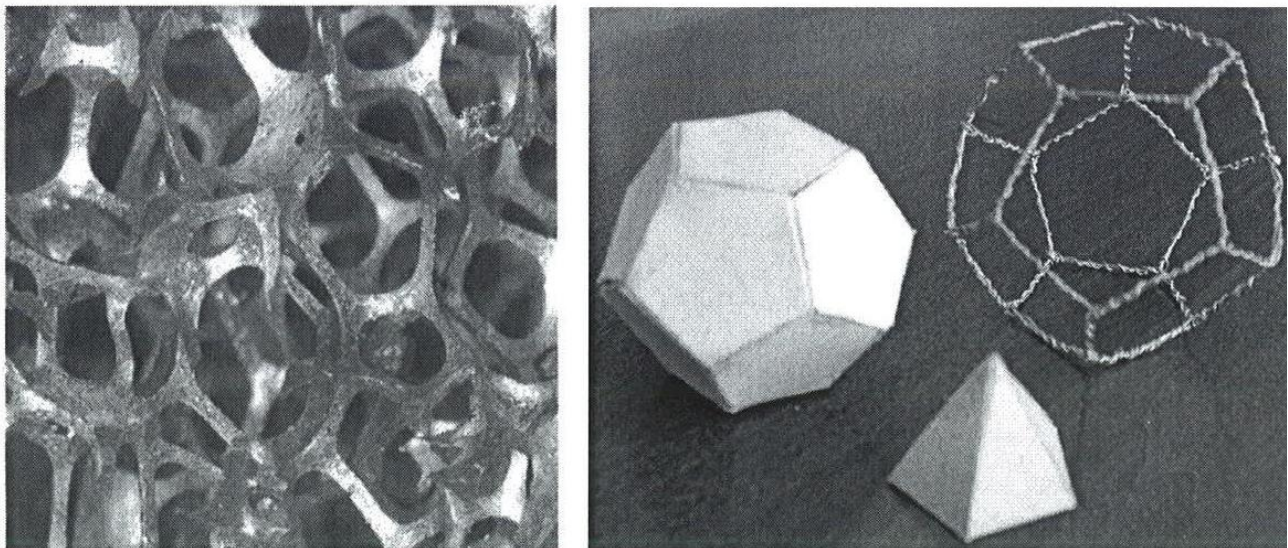


Figure 2.5.1. Structure of metal foam and dodecahedron having 12 pentagon shaped facets [10]

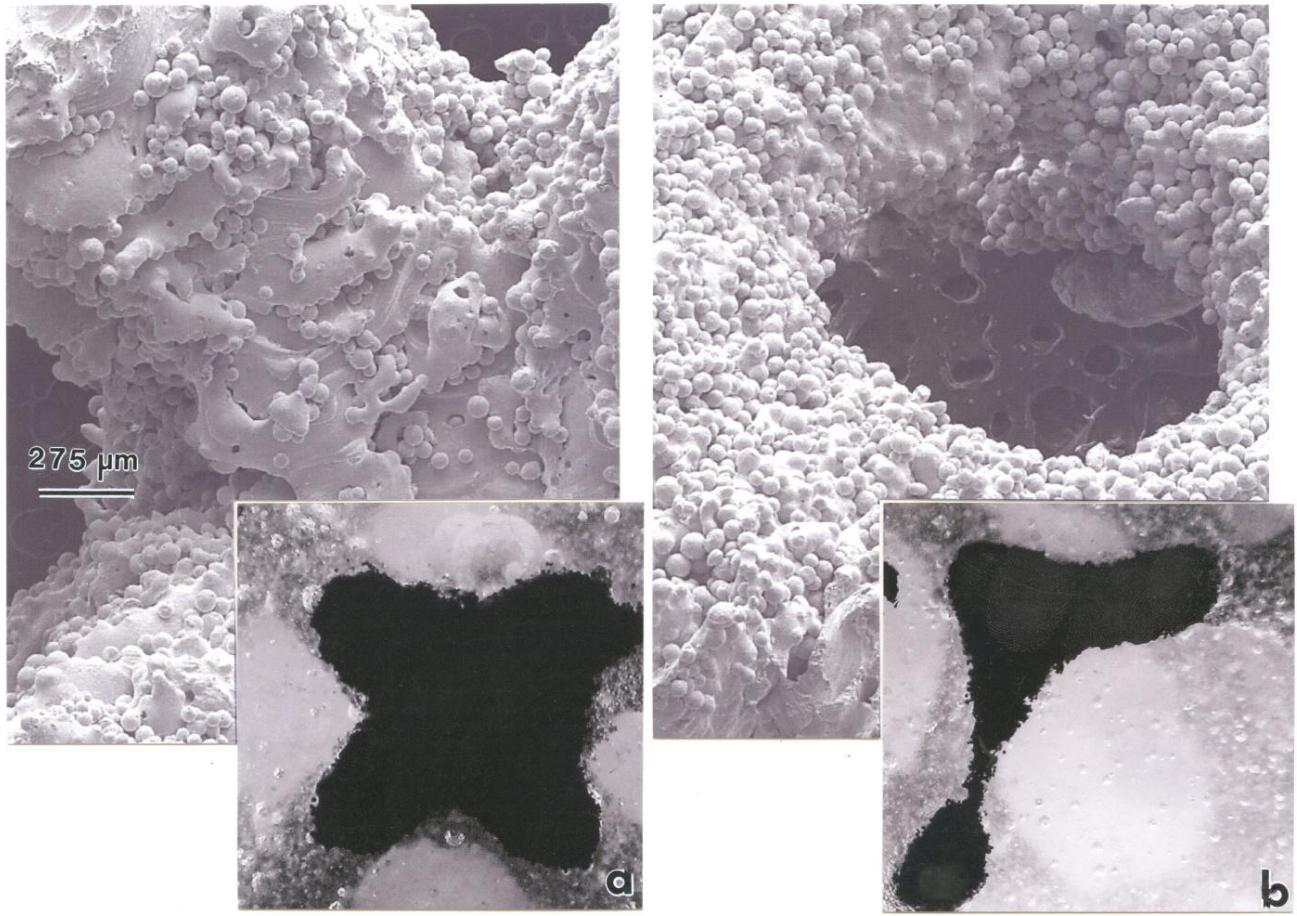


Figure 2.5.2. SEM image comparison for a reticulated mesh strut microstructure (a) and stochastic open cellular foam ligament microstructure (b). Inserts in (a) and (b) show strut and ligament cross-sections viewed by optical metallography

Gibson and Ashby have described open cellular foam structures generally by

$$E = E_o \left(\frac{\rho}{\rho_o} \right)^n ,$$

where E and E_o are the Young's moduli of the foam or cellular structure material and the fully dense material respectively, ρ and ρ_o are the corresponding porous and fully dense material densities and n has a value shown to vary between 1.8 and 2.3" [11]. Similar studies have shown that both reticulated mesh

structures and open cellular foam structures for the fabrication components of Ti-6Al-4V have similar log-log plots with $n \approx 2.3$. This will be reference further in the comparison of the copper mesh and foam fabrication relative densities and young modulus of elasticity due to the fact that there is no real data to compare copper foam or mesh structure stiffness with density or relative density with and other properties.

2.6 HEAT TRANSFER

It is important to remember that certain properties influence how well the foam will transfer heat. The pore size, filament size, and cell shape are some examples of characteristics that can influence the heat transfer through the foam. This has been a topic of interest which has been studied in recent years. Heat transfer by conduction involves energy transfer without any material motion, and the rate of heat transfer is dependent upon the temperature gradient and the thermal conductivity of the material. The thermal and electrical conductivities of metals are proportional at some specific temperature. By raising the temperature, the thermal conductivity increases and electrical conductivity decreases. Likewise, metals that have high electrical conductivity have high thermal conductivity at a given temperature.

Furthermore, an important application of metal foams is to construct compact heat exchangers. Boomsma et.al [12] performed a study where open-cell aluminum foams were compressed using various factors and then shaped in to heat exchangers for electronic cooling applications, which disperse large amounts of heat. Other studies were performed to determine the most efficient heat exchanger for particular heat transfer requirements. Previously, Bastawros was able to demonstrate the efficiency of metallic foams in forced convection heat removal [13]. This proved that a high performance cellular aluminum heat sink removed 2-3 times the usual heat flux removed by a pin-fin array. Writz research involved the study of combined conduction and convection heat transfer in a thin porous wall [14]. This was done through a semi-empirical model in a one-dimensional conduction in the porous matrix as well

as a one-dimensional flow of the coolant through the foam wall. This provided an estimate of about 1.5 times more heat transfer surface in comparison to the offset strip fin array.

2.7 PREVIOUS RESEARCH STUDIES OF OPEN-CELLULAR AND STOCHASTIC MESH AND FOAMS

There are two types of cellular metal structures which can be characterized as either stochastic or non-stochastic geometries. The difference between stochastic and non-stochastic is that stochastic foams are either open or closed cells and non-stochastic foams have repeating lattices structures. Various methods have been used to fabricate stochastic metal foams [15]. The fabrication of closed cell stochastic foams is usually achieved by producing gas bubbles in a melt pool. This is achieved by either adding gas directly to the melt, adding gas releasing blowing agents, or causing precipitation of gas bubbles [16]. In order to achieve the desire pore size, shape, and pore distribution needs to follow controlled processes, which influence the material properties [17-19]. These structures have potential use in acoustic damping and energy absorption [16]. The fabrication of open cell stochastic foams can be fabricated by melt processing, powder processing and deposition methods [16].

Other studies have shown that the use of non-stochastic open cell structures can enhance mechanical properties in comparison to stochastic foams [20-22]. While melt-processing of aluminum and aluminum alloys have produced cellular foams with open or closed cells for at least the past 30 years[23-27], in recent decades, highly-porous metals and alloy products such as titanium alloys have numerous potential applications as a consequence of their light weight, corrosion resistance, and isotropic mechanical properties [27]. Murr et al. [28] have fabricated Ti-6Al-4V open cellular foams using electron beam melting (EBM). The model for these foams were developed from CT-scans of aluminum open cellular foams and embedded in CAD for EBM. The CAD models created by the CT-scans served as building parameters which allowed spatial replication similar to crystal unit cells [28]. Figure 2.7.1 shows a 3D model of cell structure solid ligaments based on the CT-scan for aluminum

alloy foams. The CAD system includes the CT-scan and the melt scan is driven by the CAD system allowing to selectively melting each layer to build the foams. The building of these foams showed that hollow structures were lower in density than the solid structure cellular foams with identical porosity or pores/inch (ppi) [28]. The use of direct manufacturing of metals structures through the use of selective laser melting (SLM) process by the MCP group has revealed that in the use of three-dimensional structures of stainless steel and cobalt-chrome resulted in nearly 90% percent reduction [29]. Murr et al. [28] have shown the ability to fabricate Ti-6Al-4V open cellular foams and shown that elastic moduli vary with density (relative stiffness versus relative density) showing consistence with the Gibson-Ashby foam model.

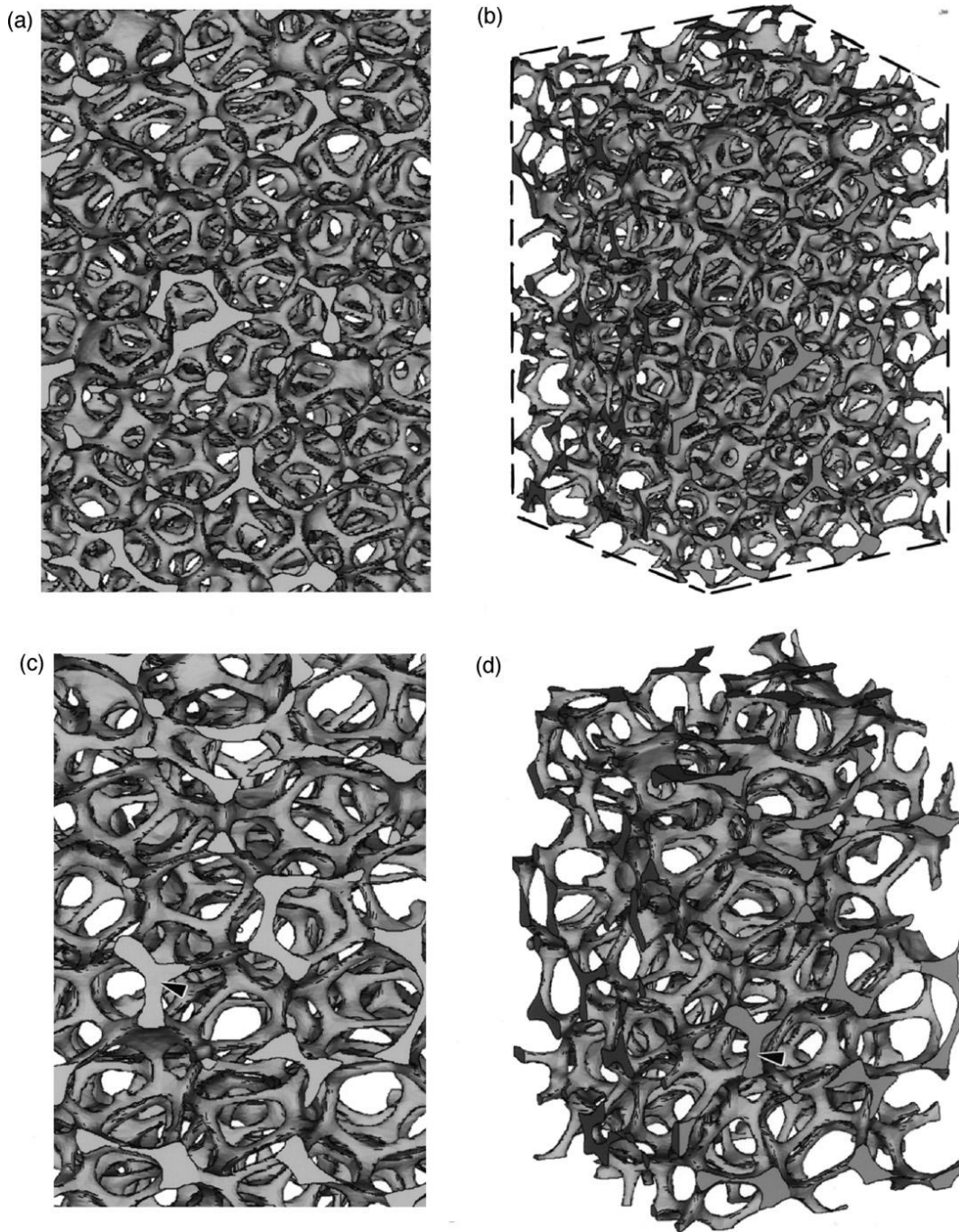


Figure 2.7.1. 3D CAD models for open cellular foams developed by CT-scans for aluminum alloy foams. From Murr et al. [28]

The foams were fabricated both in solid cell structures as well as hollow cell structures and demonstrated tolerable stiffness and strength. This proved that using Ti-6Al-4V open cellular foams have innovative applications for biomedical implants.

2.7.1 Novel Precipitate – Microstructural Architecture

In recent studies Co-base alloy containing 0.2% C, fabricated using EBM displayed spatial carbide arrays and shown to extend into carbide columns as the layer grows [30]. This type of microstructural structure has also been observed in Ni-base alloy (Inconel 718) and in SLM Ti-6Al-4V alloy has shown the grains to grow epitaxial due to no nucleation barrier to solidification [31]. This is related to the process parameters, showing that grain direction is therefore parallel with the local conductive heat transfer. This has also revealed the possibility for the prospects of controlled microstructural architecture and hence powerful tool to control grain orientation [31].

It has been demonstrated that the electron beam raster and the melt scan parameters create spatial arrays that extend into carbide columns as the layer growth. Strondl et al. [9] have also demonstrated that Inconel 718 samples produced by additive manufacturing (AM) using EBM of prealloyed powder have demonstrated columnar grains perpendicular to the solidified layers. The microstructure displayed lines of precipitates parallel to the elongated grains were present on the grain boundaries and within the grains. In similar studies, Murr et al., [31] using Inconel 625 prealloyed precursor powder produced elongated grains extending hundreds of microns parallel to the build direction as the work of Strondl et al.,[9] where they also noted a [100] columnar grain texture.

These studies have indicated unique examples of the prospects for controlled microstructural architecture development in material processing. Although the growth in controlled manner of columnar

grains might be considered a form of microstructural architectures, it represents the spatial and geometrical manipulation of grains or grain structures [30]. Manipulation of microstructure can be performed by strain, heat treatment or aging in alloy compositions, however, these are not true architectures because they represent only spatial arrays or are confined to the grain matrix making the morphology of the microstructure vary in geometry due to the crystal orientation of each grain. The process manipulation of precipitates to form even simple architectures transgressing grain structures or grain boundaries as indicated by Co-base alloy and Ni-base alloy fabrication [30] illustrates the prospects for manipulating microstructures to form architectures which can extend the materials science and engineering paradigm.

Chapter 3:

Experimental Procedure / Methodology

3.1 ANALYSIS OF POWDER

The composition, shape and size distribution of the precursor powder is able to significantly be influenced by the EBM process parameters. Thus, initial efforts were focused on evaluating and optimizing best possible powders from manufactures that would be able to facilitate the fabrication of copper components and fabrication of copper mesh and foam structures as well. This proposed research began with the investigation of two copper powders. The powders were fabricated by two different manufacturers in which one was air-exposed and the other was a vacuum powder. The “air-exposed” was a grade 153A copper powder manufactured by AcuPowder International and the process consisted of air atomized and a purity of 99.8%. The “vacuum powder” was an oxygen free high conductivity (OFHC) copper powder manufactured by Sandvik Materials Technology. This was argon atomized with purity of 99.99%.

3.1.1 Flow of Copper Powder

The flow of a powder is dependent on the shape, apparent density and surface contamination which can be important factors to be considered for the EBM process because it directly affects the packing and raking of the powder. These factors were in accordance with the ASTM standards B703-10 and B855-06 respectively for the apparent density and volumetric flow rate of both precursor powders analyzed.

Both powders were examined using the SEM to study their morphology, particle distribution and chemical composition using the EDS. The shape of atomized powder can vary significantly in size and shape. In this case the vacuum powder exhibited very irregular shapes and less spherical than the air-exposed powder. Fig. 3.1.1 illustrates the particle shape and size of both powders. Fig. 3.1.1(a) corresponds to the vacuum powder which shows the irregularity in shape and size in comparison to (b) where the air-exposed is more spherical and similar size and shape throughout. The small particles attached to the surface of large particles as shown in (a), cause a poor flow, whereas, particles with relatively equal size increase flowability.

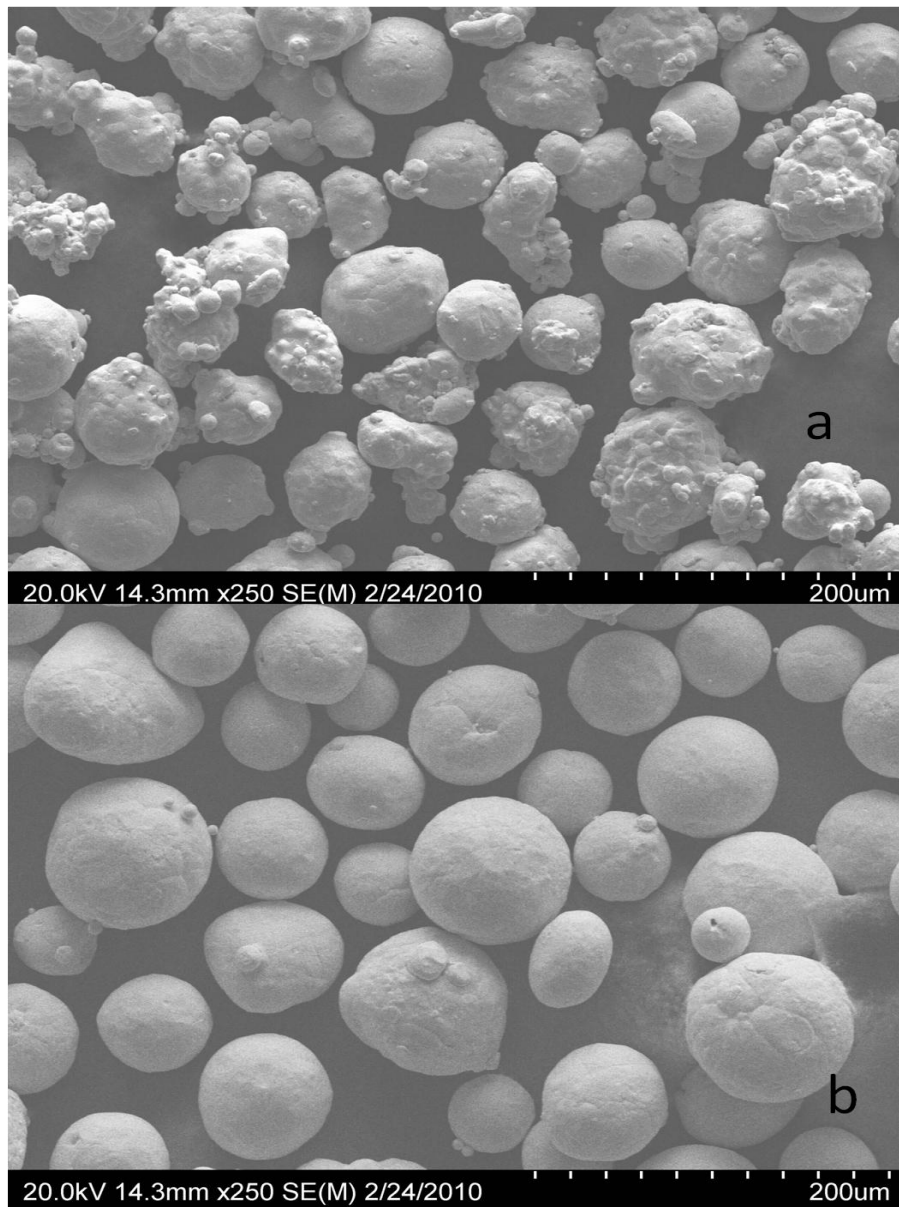


Fig. 3.1.1 illustrates the (a) vacuum powder and (b) precursor air-exposed powder.

3.1.2 Powder Size Distribution

The distribution of particle size and the average of particle size is important to be considered during the EBM process. Particles that are too small become a health issue and a safety risk, while large

particles are not deposited by the raking system. This can also lead to a significant influence on thermal conductivity due to relative packing density and the contact area between the particles. The size distribution was analyzed on both powders. Powder A (argon atomized with purity of 99.9%) showing two distributions: one separating the satellite particles from the distribution measurements and the overall particle diameter. Powder B (nominal purity of 99.8%) shows a bimodal with average size of $\sim 54 \mu\text{m}$.

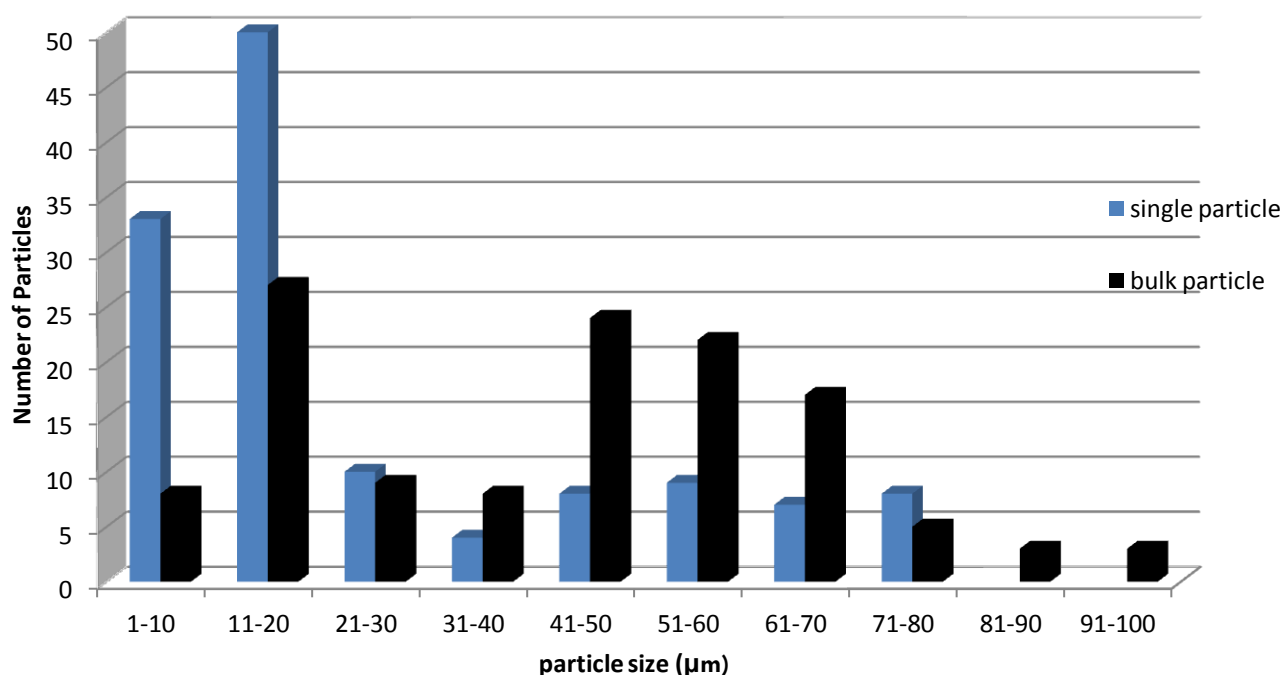


Figure. 3.1.2 Measurement of particle size distribution for Argon Atomized Powder showing both satellite particles and overall particle diameter.

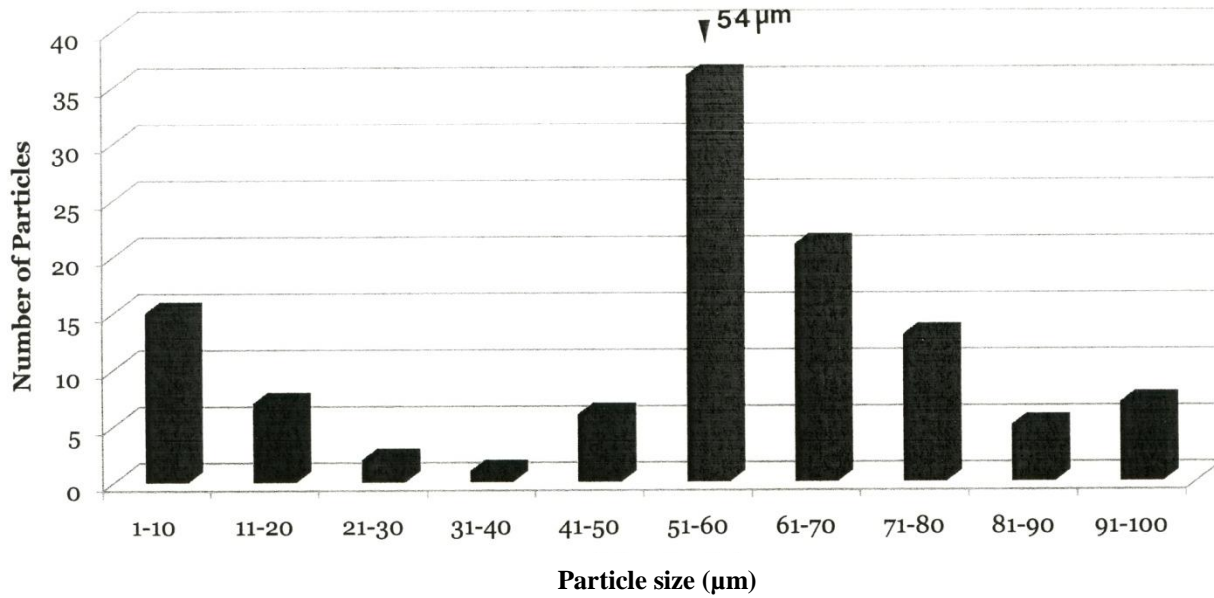


Figure 3.1.3 Precursor copper powder particle size distribution with an average size of 54 μm (arrow).

3.1.3 Microstructural Analysis of Copper Powder

The atomized copper powder with nominal purity of 99.8% Cu was utilized for the fabrication of all the components. We utilized this powder because it was more regular and presumably more tractable for EBM processing as shown in Fig. 3.1.2. The balance of this composition was primarily oxygen, which formed a high volume fraction of copper oxides (Cu_2O) (Cuprite) which segregated to the powder grain boundaries. Cu_2O has a cubic crystal structure with a lattice parameter of 4.27 Å as well as a space group $\text{PN}3\text{M}$. By the use of the scanning electron microscopy (SEM) the copper powder size and surface characteristics can be shown in figure 3.1.4. The particle size distribution consisted of primarily of large particles ranging from 40-100 μm, with smaller attached particles as seen in figure 3.1.3.



Figure 3.1.4. Precursor copper powder (SEM images). The magnified insert shows particle surface features delineating grains having average diameters of $\sim 6 \mu\text{m}$. [30]

3.1.4 Optical Metallography and SEM Analysis of Copper Powder

The use of light optical microscopy is an important part of this research because it allows for microstructural analysis to be performed both on the precursor powder and samples components fabricated by the EBM. The powders were encapsulated in mounting epoxy which was ground, polished (mirror-like using a final polish with 0.05 μm alumina) and etched using a solution consisting of 100mL water, 8mL sulfuric acid, 4 mL sodium chloride (as a saturated solution) and 2g potassium perchlorate and rinsed with ethanol for analysis purposes. Etching times varied from ~2 -3 seconds and were observed in a Reichart MF4 A/M optical metallograph using a digital image converter. The etchant revealed the particle interior microstructures as illustrated in Fig. 3.1.5 where the grain size averages 6 μm , a relatively small size giving rise to an instrumental Vickers microindentation hardness of 72 as indicated in Fig. 3.1.5(a). The magnified view shown in Fig. 3.1.5(b) illustrates the selective etching of precipitates within the grain boundaries forming regular, often square or rectangular pits.

The residual Vickers microindentation hardness (HV) samples were measured in a Struers Doramin A-300 digital test station using a 100 gf load, with a dwell time of 10s for the precursor powder, EBM components and open-cellular mesh and foams structures.

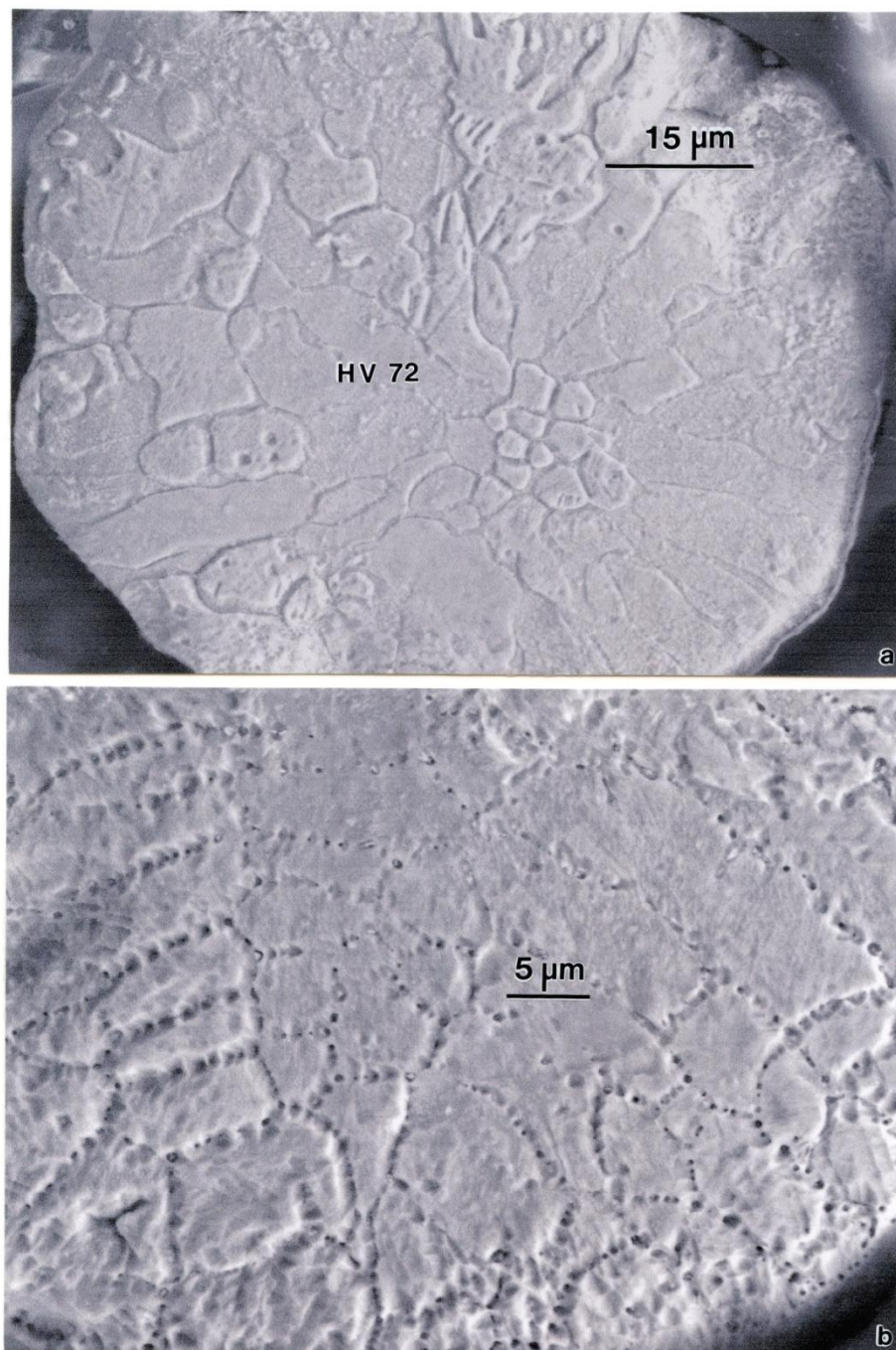


Figure 3.1.5. Precursor copper powder particle internal microstructure for embedded, ground, polished, and etched particles. (a) single-particle observation in the SEM showing grain structures apparent from the surface views. (b) Magnified view showing preferential etch/etch pits having regular (cubic-like) geometries within the grain boundaries.

3.2 EBM PARAMETERS FOR THE FABRICATION OF COPPER COMPONENTS

This section provides the parameters utilized for the building specimens and the fabrication of copper mesh and foams. The Cu precursor powder was gravity fed to the build table where it was raked into successive layers roughly 100 μm thick. The electron beam had an accelerating voltage of 60kV, focused by magnetic lenses and scanned by scan coils to pre heat and selectively melts the powder layer by layer through computer-aided design (CAD) program. The table consisted of a commercial copper plate preheated (with the beam) to 550°C. The powder layers raked and selectively melted were also preheated by scanning the beam (in a vacuum of $\sim 10^{-4}$ torr) and a rate of $\sim 10^4$ mm/s in 10 passes with a beam current of 13.4 mA. The melt scan had a scan rate of 80mm/s at a beam current of 10mA. The pre-melt scan also followed at a scan rate of 2×10^3 mm/s and 30mA beam current. The scan domain (the x-y zone) created especially in the melt scans is dependent on the beam focus, with directs maximum energy at varying depths within each powder bed in the x- and y-directions [30]. For the purpose of this work, the so called beam focus offset, was varied using focus numbers which varied from 10 to 35, with 35 being the deepest focal length. This does not cause a change in beam spacing; however, the change in scan spacing comes from the beam focus offset and by varying the beam focus offset, thus the spacing increases. The scanning strategies have also been addressed by Thijs et al. [32] and Verhaeghe et al.[33] in SLM fabrication process.

3.2.1 Fabrication of Copper Components

In the fabrication of Cu components, the precursor Cu powder contained a high volume fraction of Cu_2O precipitates. These were retained and increased by reaction with internal oxygen in the components and distributed in spatial architectures along with dense dislocations substructures due to the powder-layer preheat and melt scan parameters. The specimens developed were characterized using optical microscopy and scanning and transmission electron microscopy.

Different components with different geometries were fabricated so that the built parameter sections were examined. These included small cylinders and rectangular blocks and other geometry variations. These components are illustrated in Figure 3.2.1.

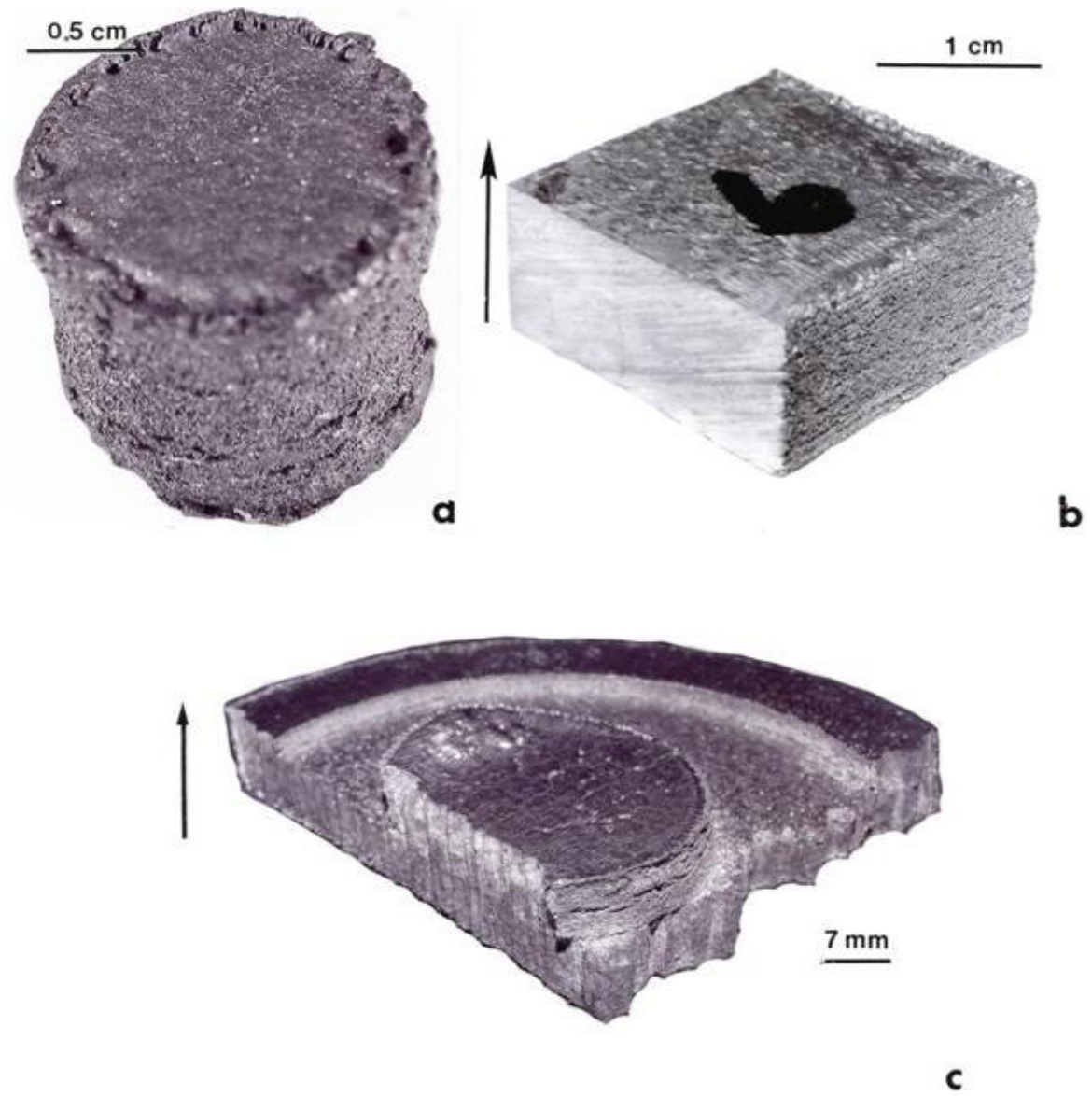


Figure 3.2.1. Examples of components and component (build) geometries fabricated by EBM. (a) small cylinder, (b) quarter section from 5 cm (25 cm^2) block, (c) structured-geometry prototype product.

3.3 OPTICAL METALLOGRAPHY ON COPPER COMPONENTS

From the components in Fig. 3.2.1, coupons or smaller specimens were extracted and cut into sections which were perpendicular to or parallel to the build direction. The sections viewed in these orientations were designated horizontal (H) and vertical (V). Both the horizontal and vertical cross sections were analyzed using the Reichert MEF4 A/M. These oriented sections were mounted, ground, polished (mirror-like using a final polish with 0.05 μ m alumina) and etched using a solution consisting of 100mL water, 8mL sulfuric acid, 4 mL sodium chloride (as a saturated solution) and 2g potassium perchlorate and rinsed with ethanol for analysis purposes.

For the reticulated mesh structures, after stiffness measurements, selective test structures were sectioned into small areas to be mounted, polished and etched for optical metallographic analysis as well. The same etchant was utilized as in the sample component specimens.

3.4 SCANNING ELECTRON MICROSCOPY

A Hitachi H-8500 field emission SEM operating at an accelerating voltage of 20 kV in secondary electron emission mode was used to analyze the polished and etched samples fabricated in the Arcam A2 system, the reticulated mesh structures, as well as the precursor copper powder utilized in the building process. The Energy Dispersive X-ray Spectroscopy (EDS) was used to perform the chemical analysis of the powder and components fabricated as well.

3.5 TRANSMISSION ELECTRON MICROSCOPY

Different samples were cut from the various build components and sliced into thin sections to a thickness less than 0.2mm. Three-millimeter discs were punched and mechanically dimpled on each

side. Electrojet polish was performed using a Struers Tenupol-3 dual-jet unit operating at 8V with a solution temperature of 15°C using a solution consisting of 825ml of water, 375ml of ethanol, 300ml of phosphoric acid, 75 ml of propanol and 2.5 of urea. This created shiny (hole induced) polished samples and were examined in a Hitachi H-9500 transmission electron microscope (TEM), operating at a accelerating potential voltage of 300 kV. A goniometer-tilt stage and a CCD digital imaging camera were utilized as well with the TEM.

3.6 FABRICATION OF RETICULATED MESH STRUCTURES

Using the program Materialize/Magics® software, reticulated mesh structures based on geometry elements were fabricated. The CT-scans of commercial open-cellular aluminum alloy foams were geometrically scaled to create monolithic density or porosity variations [34]. This is shown in figure 3.6.1 by software (CAD) model showing the open cellular mesh and foam structures [34]. Reticulated mesh structures ranging in density from 1.20 to 6.67 g/cm³ as well as a virtually solid component with a density of 8.02 g/cm³ used for comparison with fully dense Cu having an ideal density of 8.9 g/cm³. The stochastic foam densities vary from 0.73 to 1.70 g/cm³. These are shown in figure 3.6.2.

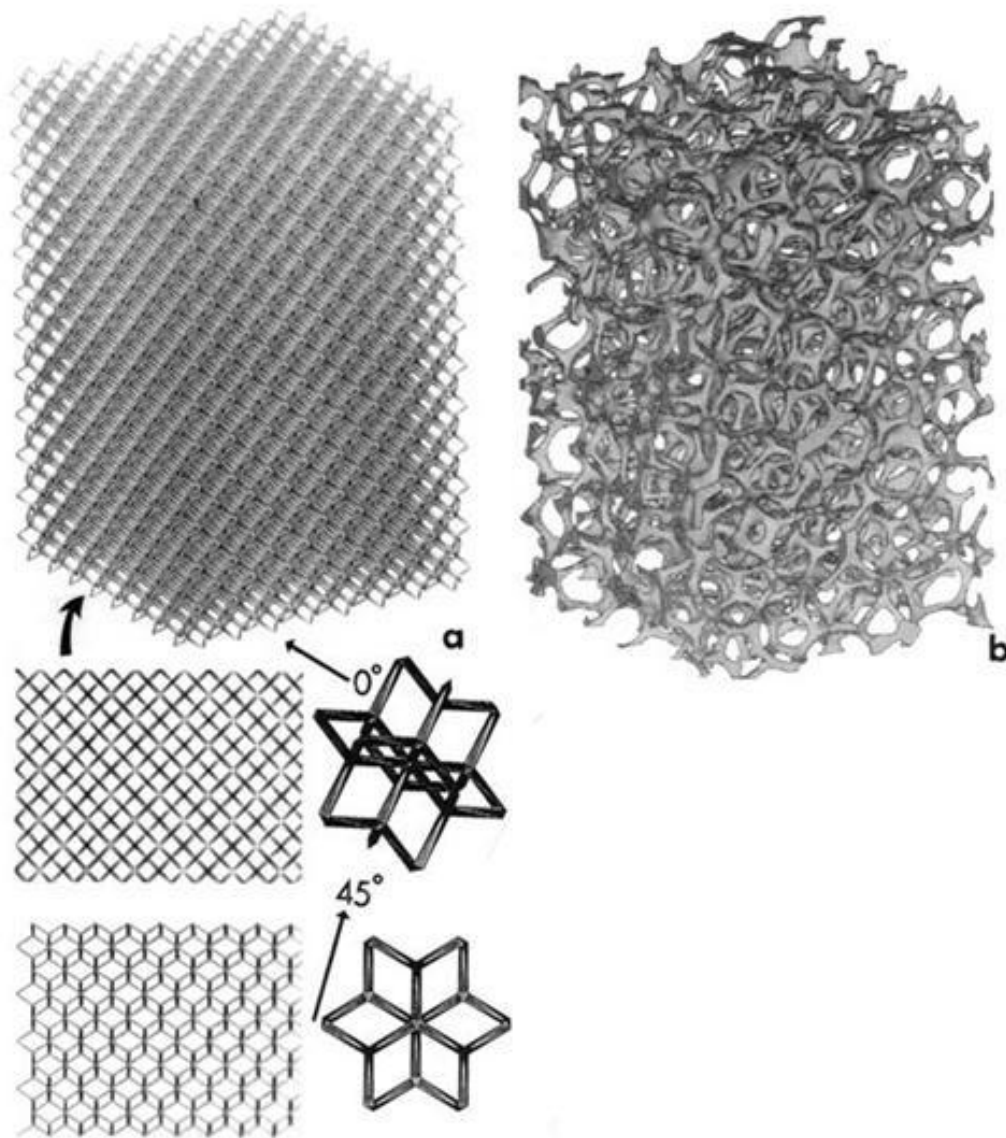


Figure 3.6.1. Schematic showing software (CAD) model using Materialized dode-thin mesh build (a) and open cellular foam model (b)

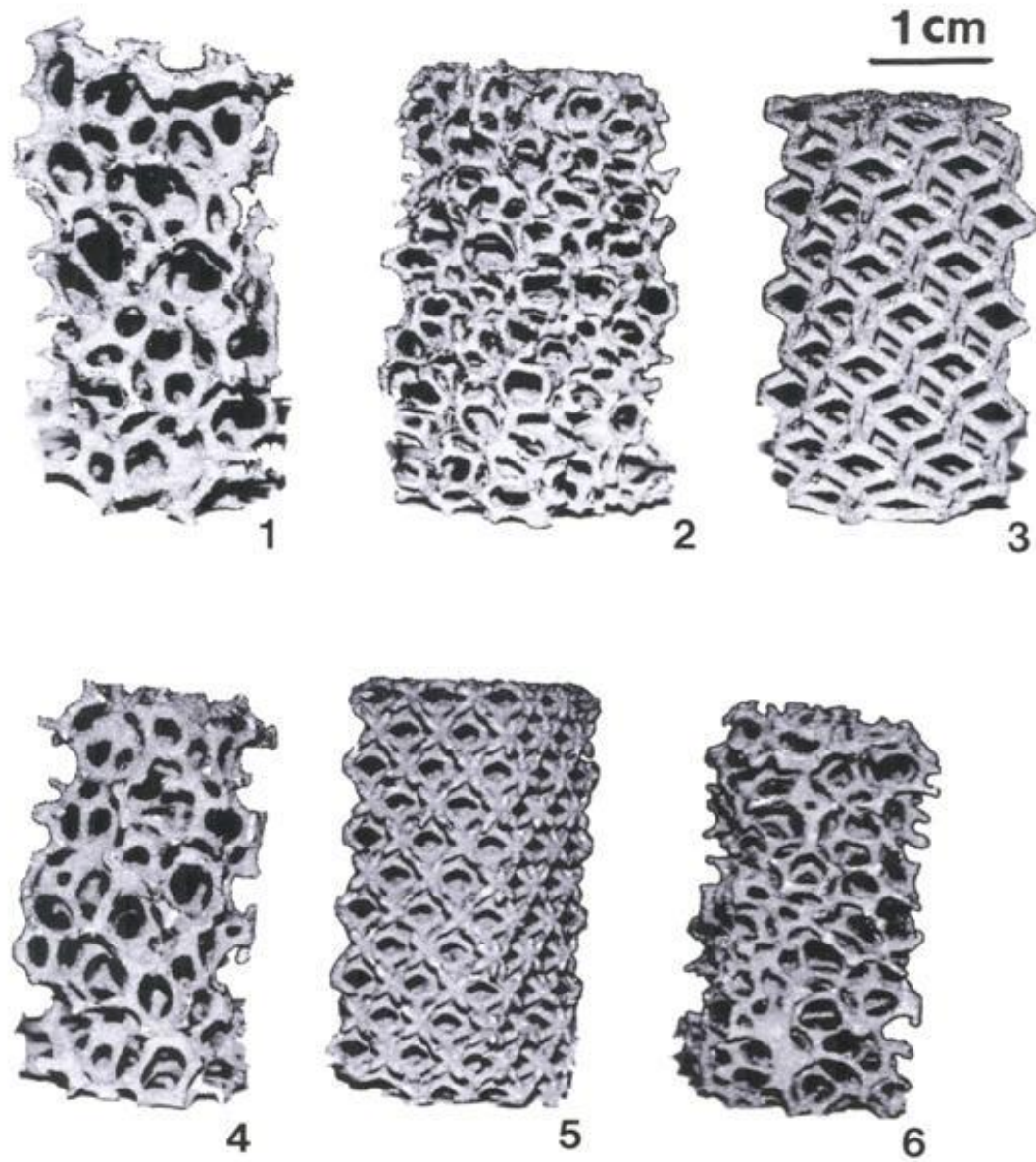


Fig. 3.6.2. Examples of open cellular Cu mesh and foam specimens fabricated from CAD models. The corresponding densities, ρ , and pore densities in pores/inch [ppi], are as follows: (1) 0.84 g/cm^3 [4 ppi]; (2) 0.73 g/cm^3 [6 ppi]; (3) 1.20 g/cm^3 [3ppi]; (4) 1.28 g/cm^3 [3 ppi]; (5) 1.69 g/cm^3 [5 ppi]; (6) 0.93 g/cm^3 [6 ppi]. Stochastic foams are shown in (1), (2), (4) and (6): Reticulated mesh samples are shown in (3) and (5). [34]

3.7 ELASTIC MODULI (E) TESTING

The elastic moduli (E) for the fabricated open-cellular structures were measured using a resonant frequency analyzer RFD AHTVP1750-C. This process measures the resonant frequency in the samples arising from a mechanically induced vibration where the stiffness (E) is given generally by

$$E = \xi m f_r^2,$$

where ξ is a geometrical, specimen shape factor (generally constant for these measurements), m is the sample mass and f_r is the measured, resonant frequency [34]. This is a non-destructive testing that measures the dynamic stiffness in comparison to the static stiffness of more conventional, tensile or compressive testing which is destructive testing. All the open cellular structures followed the requirements described by Ashby [34] height/width > 1.5 height > 7 times the cell size, and open channel size. The samples sizes were 2.3 cm x 2.3 cm x 3.6 cm and in some cases carefully machined to size in larger samples.

Chapter 4

Result and Discussion

4.1 MICROSTRUCTURAL ANALYSIS ON COPPER COMPONENTS

Figure 4.1.1 illustrates an optical representation of microstructure in the horizontal direction for component (Fig.3.2.1(c)) with beam offset (focus setting) of (a) 10, (b) 25, and (c) 35, with 35 being the deepest focal length. This is similar to the process variations for SLM fabrication [32] and shows refinement in the microstructure with thermal variations due to the beam focus variations. Each of the beam-scanning steps included orthogonal beam rastering over the powder bed in the x- and y- directions.

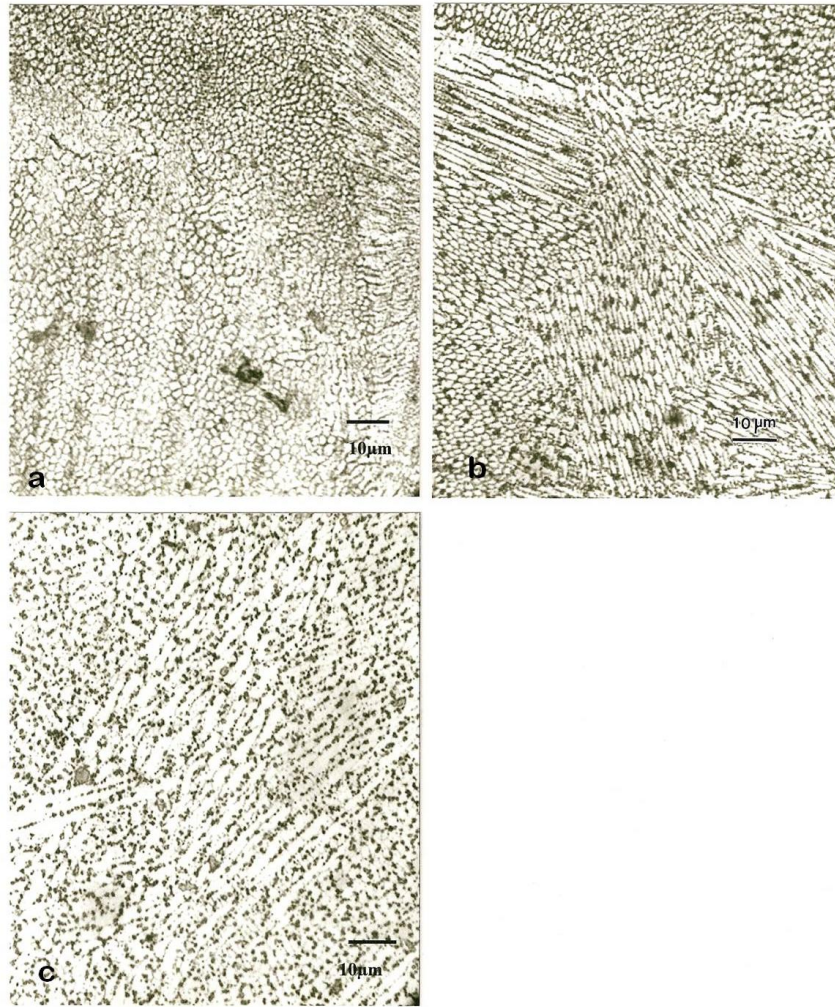


Figure 4.1.1 Optical representation of microstructure in the horizontal direction for component (Fig. 3.2.1 C). Beam offset: (a) 10, (b) 25, and (c) 35; with 35 being the deepest focal length

Figure 4.1.2 illustrates a 3D image composite representing typical microstructure of a section of the cylindrical component as shown in Fig.3.2.1(a). This 3D image illustrates small, equiaxed cell or domain structures in the horizontal plane and elongated structures in the vertical plane. The vertical section is parallel to the build direction as indicated by the arrow.

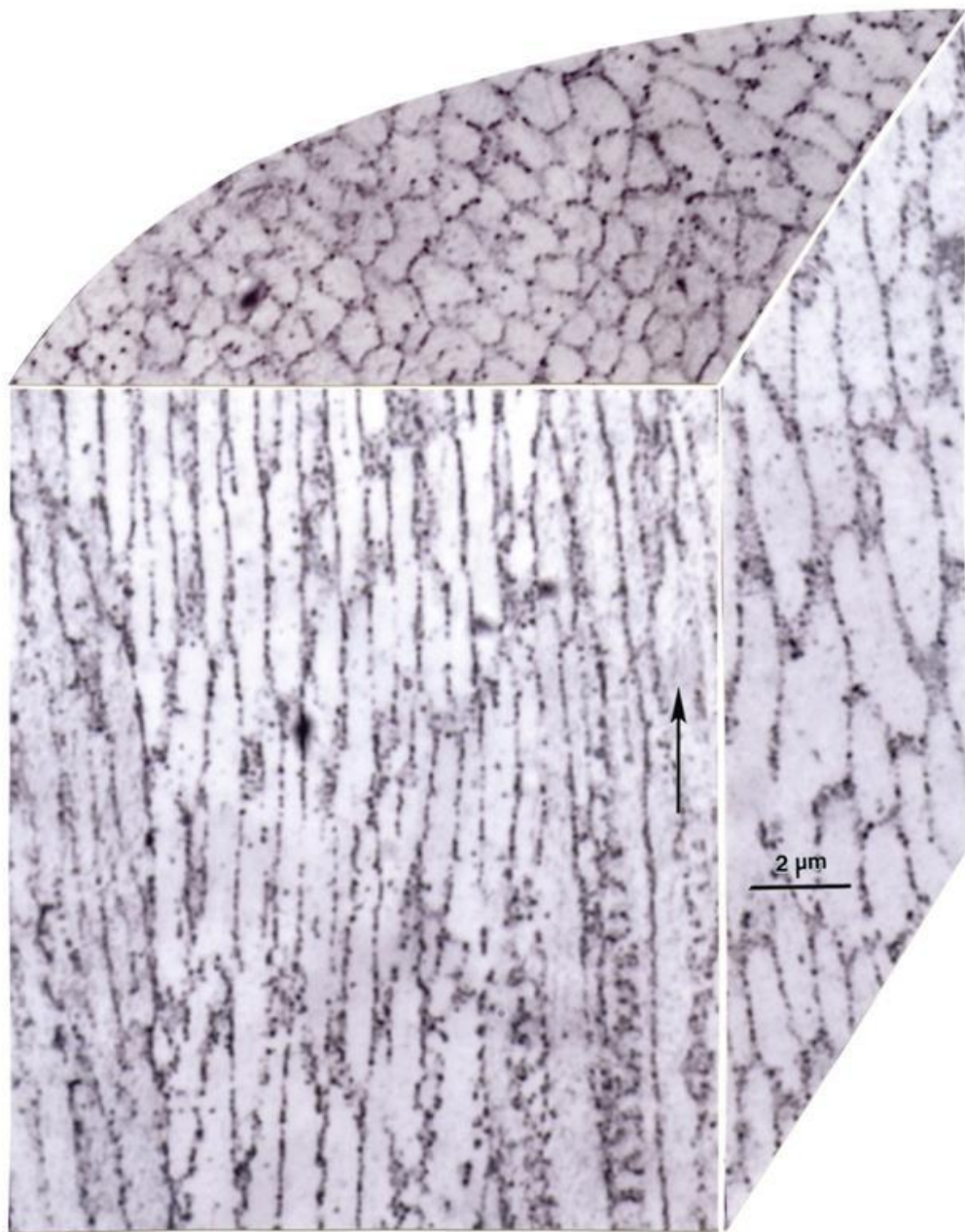


Figure 4.1.2 3D image composite representing a section of the cylindrical components.

Figure 4.1.3 is also 3D- image composite from a cylindrical section of Fig. 3.2.1 that indicate the hardness measure (a) that shows small equiaxed cell or domain structures in the horizontal plane which is perpendicular to the build direction and the elongated structures variations in the vertical plane parallel to the build direction. These areas are very small in comparison to the equiaxed grain structures previously seen in the precursor powder shown in Fig.4.1.3. This explains in part the increase in hardness in both the horizontal and vertical planes and as indicated in Fig.4.1.3. Furthermore, while the average of both the horizontal and vertical planes microindentation hardness is ~HV 83 and has a 15% increase over the precursor powder, there is a 7% difference between the softer horizontal plane in comparison to the vertical plane. This has been explain by Murr [28] where it was noted that microstructures and residual microindentation hardness were different for reticulated mesh structures due to the variations in cooling rates for thin struts in comparison to larger, solid, monolithic components build by electron beam melting. Furthermore, the microstructure refinement in the cellular ligaments promotes higher microindentation hardness for the foam cell structures in comparison to solid, fully dense monoliths as high as 40%.

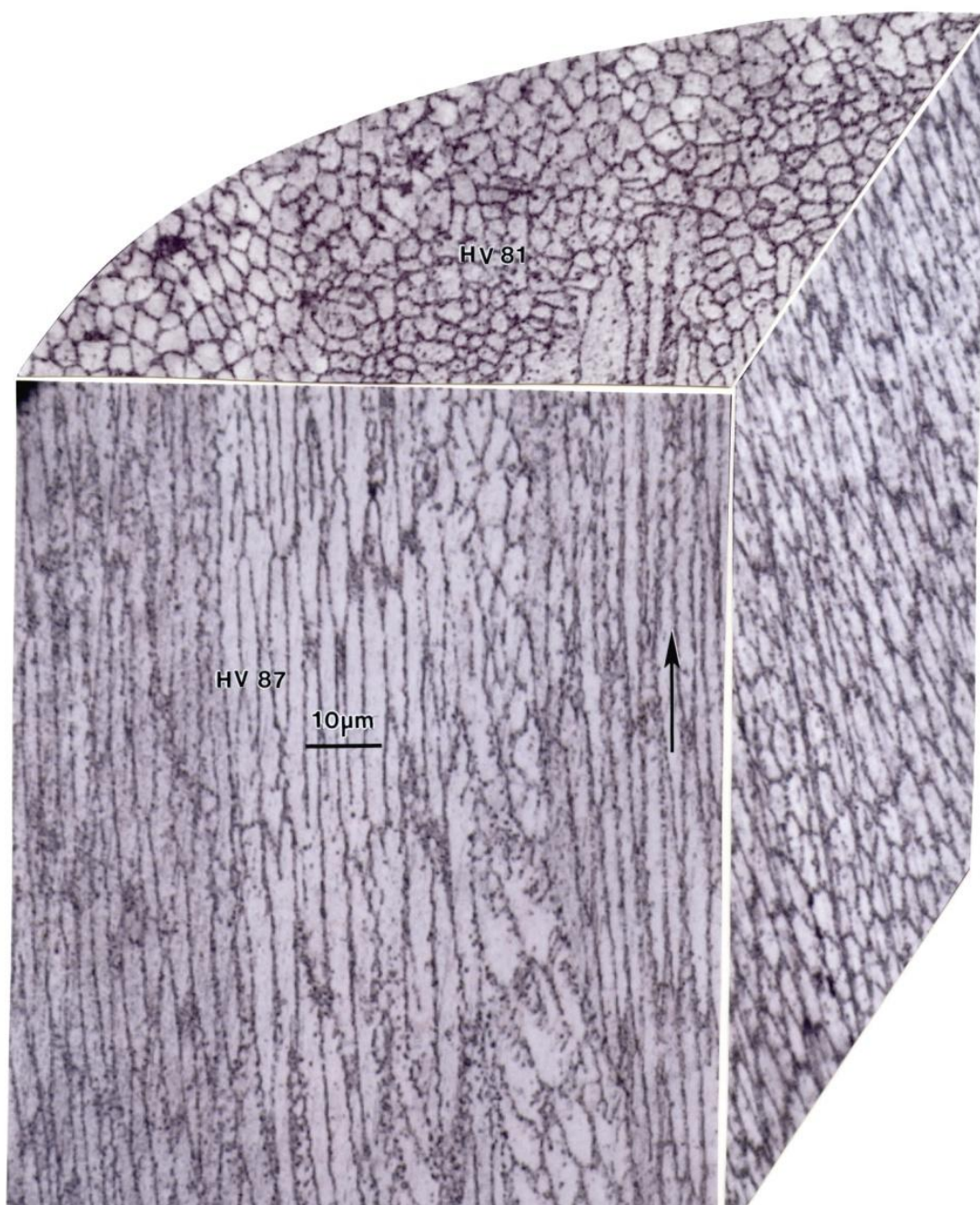


Figure 4.1.3 3D image composite representing a typical section from cylindrical components illustrated in Fig. 3.2.1 (a). Corresponding horizontal and vertical reference-plane microindentation hardness (HV) averages are indicated. Arrow indicates the layer building direction.

From figure 4.1.3 it can also be noted the irregular etching pits outline the cellular-like structures which can be seen how the etch-pit features to be regular cubic or rectangular pits comparable to those etched and previously shown in the grain boundaries in the precursor powder. This unique precipitate/dislocation-like cell structure, with non-coherent (Cu_2O) precipitates attached to dislocations which form these spatial arrays that are selectively etched forming pits in the optical and SEM images. This can be seen in Fig. 4.1.5 and Fig. 4.1.5(b) displays the cubic like geometry which propose having a relative common orientation with precipitate particles. As indicated these features are an indication of the precipitate column spacing is essentially the same ($\sim 2\text{ }\mu\text{m}$) as a consequence of the same electron beam scan parameter in the electron beam process.

This can be shown by the XRD spectrum representing the EMB-fabricated microstructural architectures. In addition the Energy Dispersive X-ray Spectroscopy (EDAX) was used to perform a chemical analysis of the powder particles used in the EBM process as well. Figure 4.1.4 illustrates the XRD spectrum representing the EBM-fabricated microstructural architecture. The enlarged insert highlights the Cu_2O (111) reflection peak and the Cu_2O peak fraction represents ~ 2 volume percent.

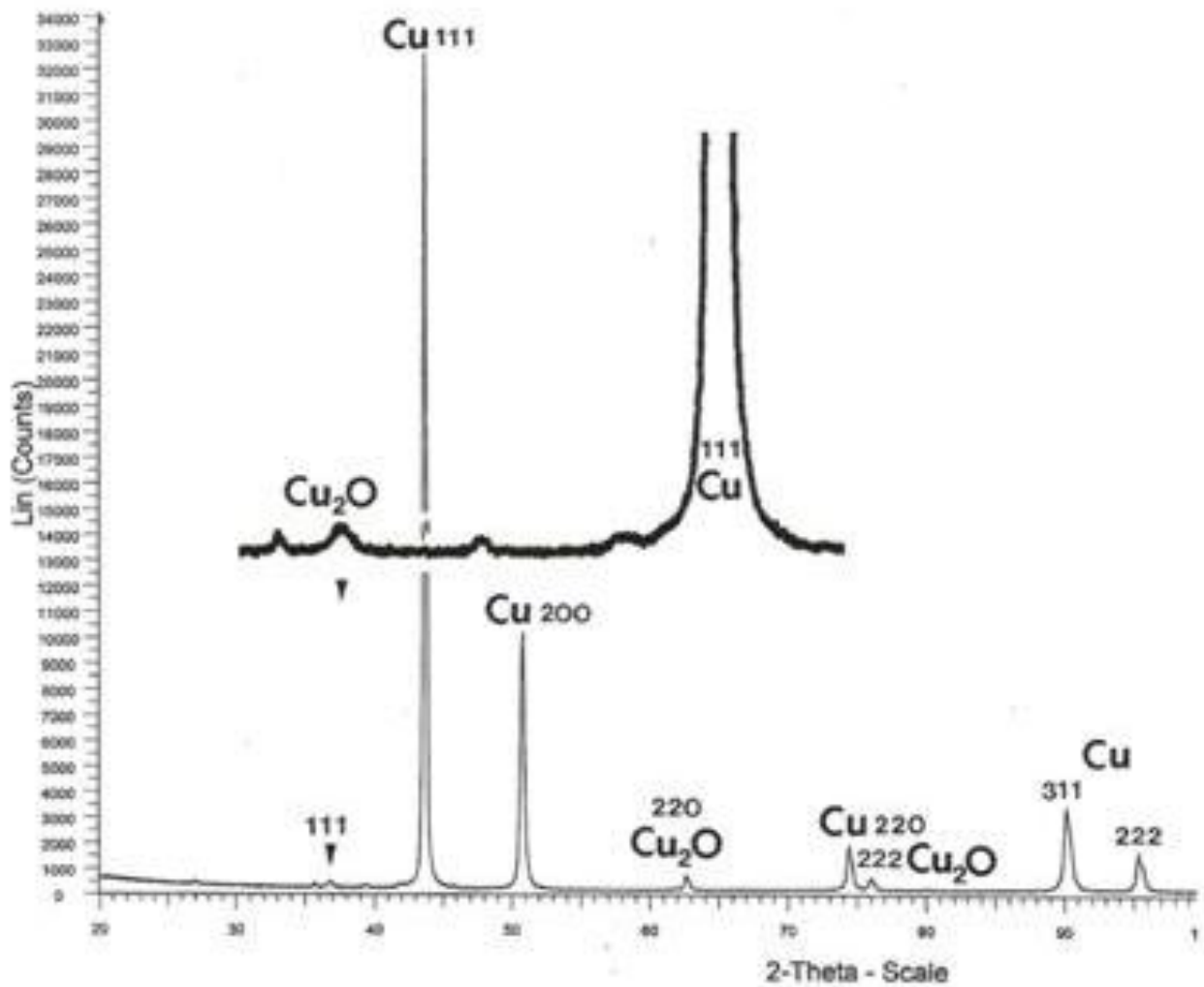


Figure 4.1.4 Illustrates the XRD Spectra shows Cu_2O representing the EBM-fabricated.

This allows for the formation of copper oxides, (Cu_2O), or retention of interstitial oxygen which will form Cu_2O during EBM fabrication creating the directional Cu_2O columns or precipitate architecture displayed shows long precipitate (Cu_2O) columns as indicated previously.

The reactions of the etchant produces systematic etch pits that replicate the cubic structure of Cu_2O . It is well known that copper oxides reaction to acids and acid etchants such as CuO and Cu_2O

produces systematic etch pits which will emulate the cubic structure of cuprite or Cu_2O . This is illustrated in figure 4.1.5 and 4.1.6 representing the vertical plane.

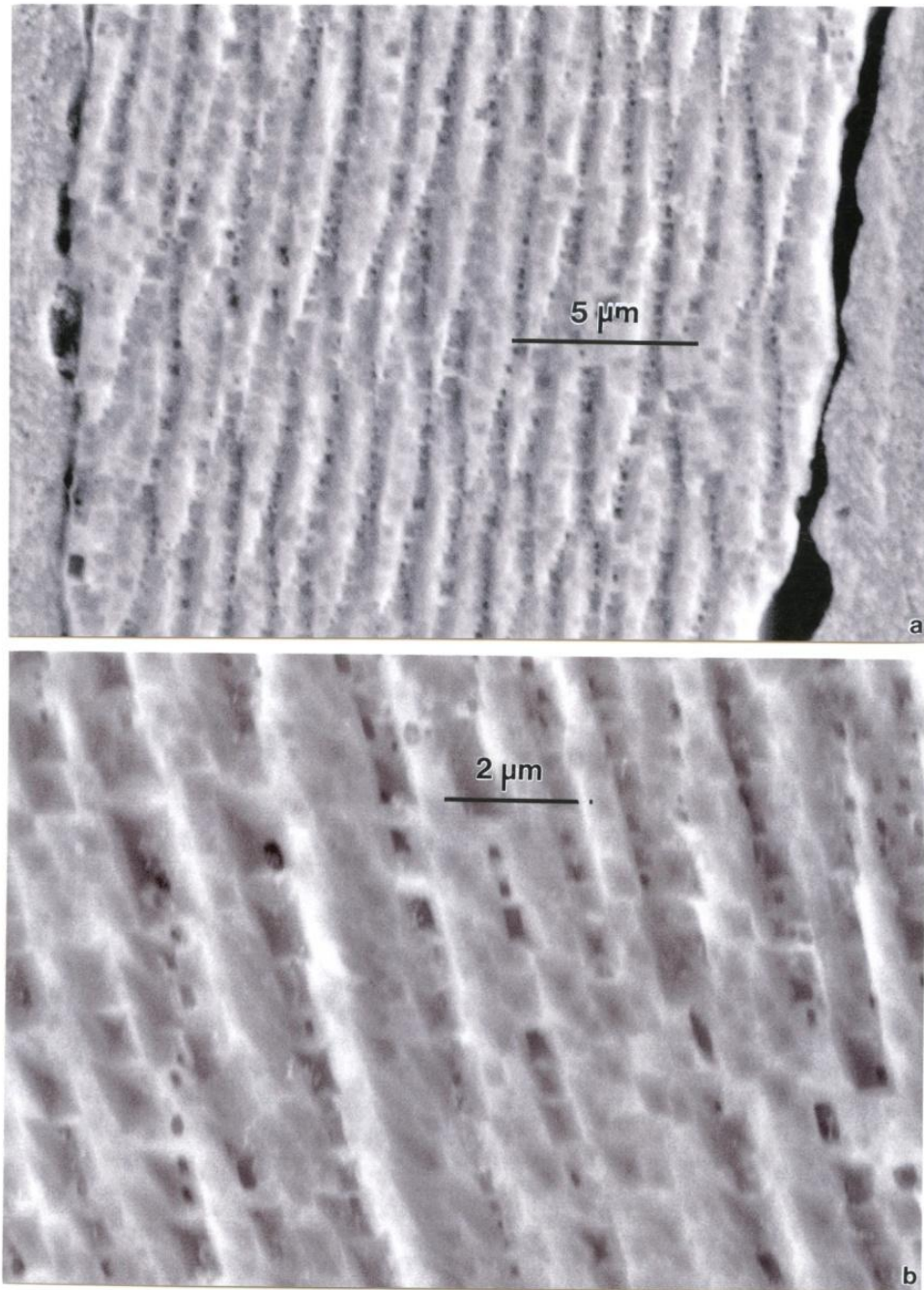


Figure 4.1.5. SEM views of regular, cube/rectangular etch pits corresponding to elongated cell-like structures in Fig. 4.1.2. (a) Vertical reference plane structures matching those in Fig. 4.1.2. (b) Magnified view showing etch-pit geometry.

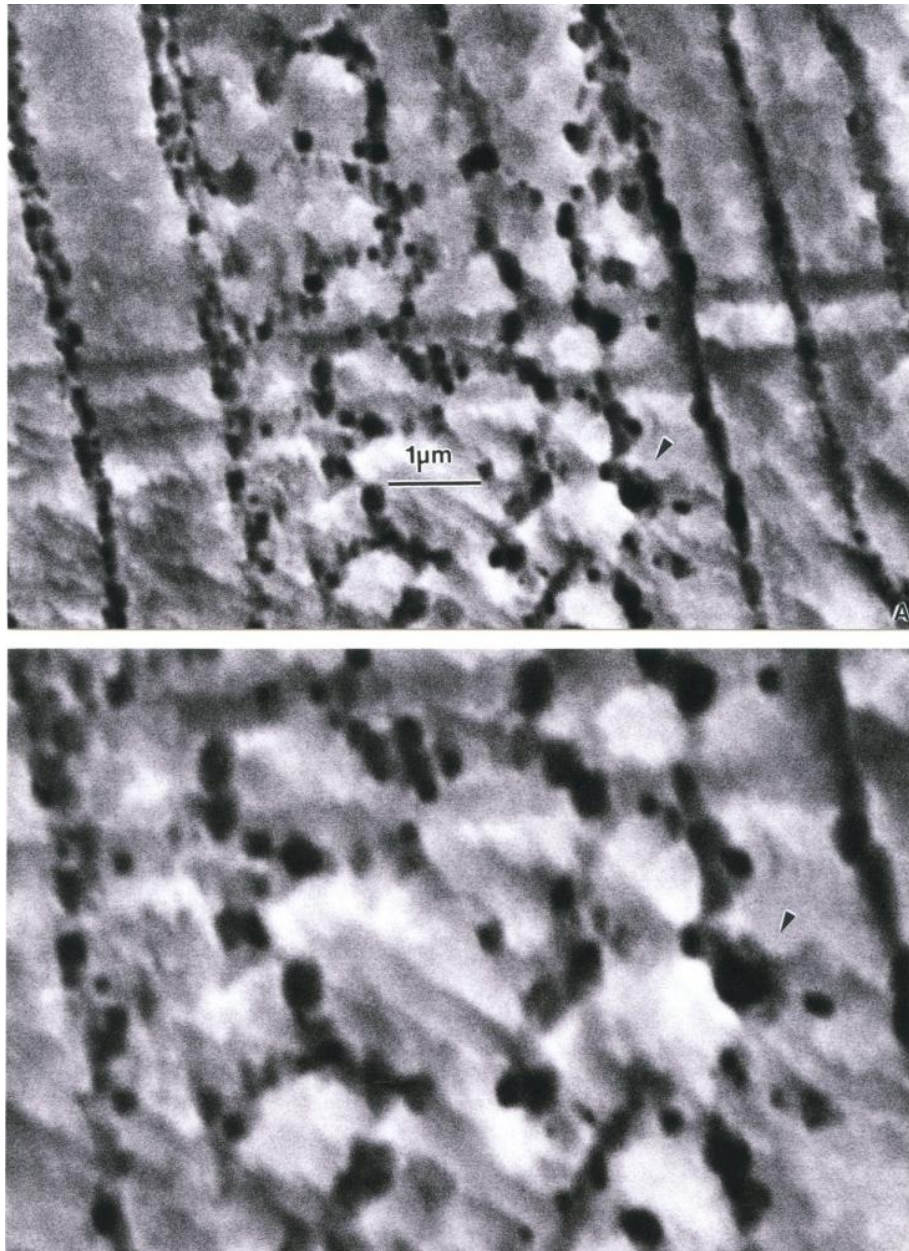


Figure 4.1.6. SEM views (A and B) for etch pits characterizing Cu_2O column-like architectures in the vertical plane parallel to the build direction. (B) shows a magnified view for reference marked by arrow in (A) and (B)

The square and orthogonal pits are evident in both SEM images (Figs. 4.1.5 and 4.1.6). This is evident in Fig. 4.1.7 showing optical metallograph image cell domain, showing a these spatial arrays, that are selectively etched and form pits in the optical microscope and SEM images.

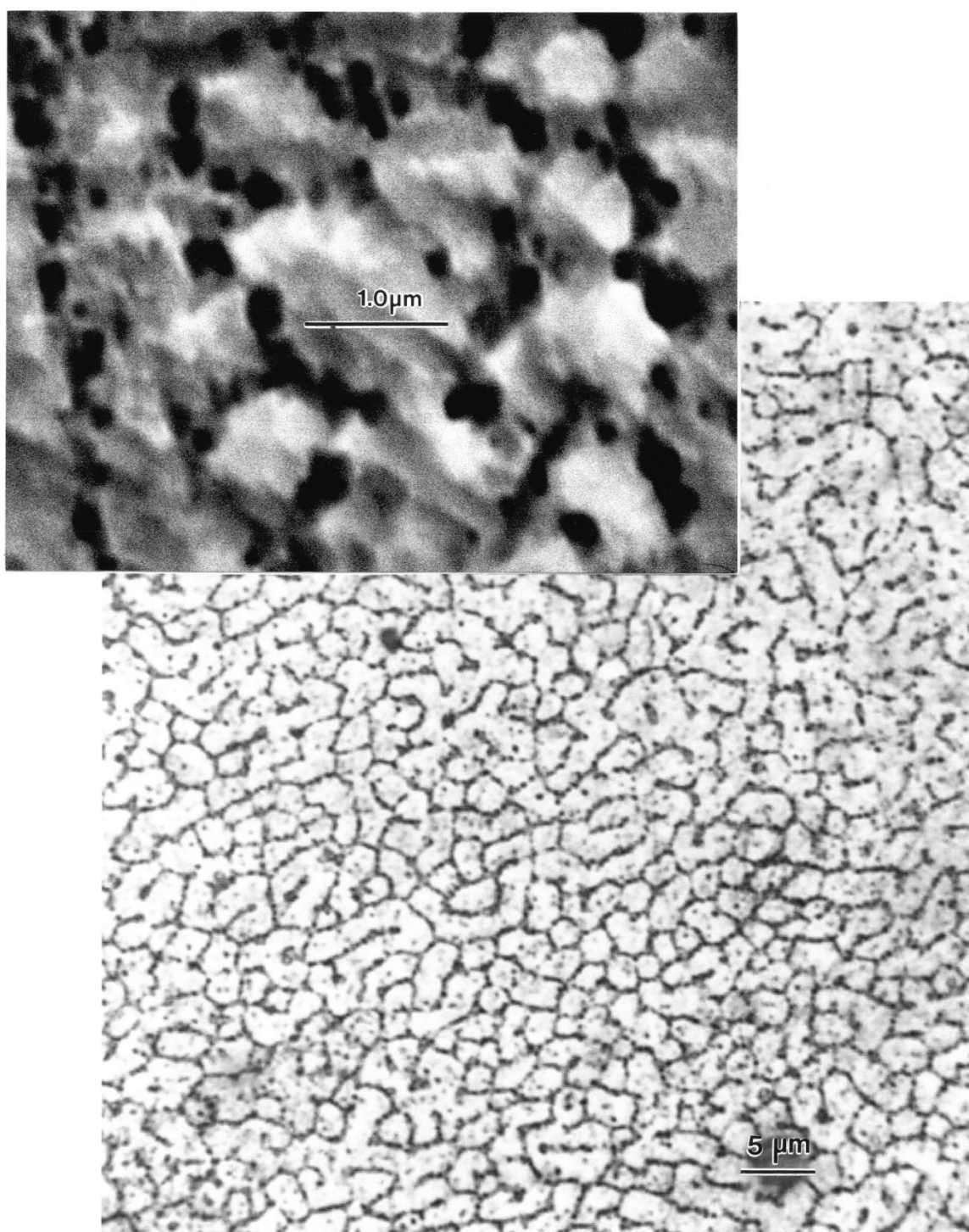


Figure 4.1.7 Optical and SEM images representing the Cu_2O precipitate showing etching details for the cellular columns composed of Cu_2O precipitates in the horizontal plane.

4.1.1 Microstructural analysis of rectangular block and geometry prototype components

The same microstructural features can also be seen in the EMB component fabricated in Fig. 3.2.1 (b) and (c). This microstructural architecture which is unique appears to be the cause of either reprecipitation in the preheat and melt scans or in can be associated with the rearrangement of precipitates during the melt scan or both. In addition, as the beam focus changed and the melt-related heating increased, the variance of precipitate-dislocation arrays between the horizontal and vertical reference plane became less apparent. These areas can create thermokinetic zones whose spatial features mainly depend on the EBM- scan dimensions or spacing. These features are illustrated schematically in figure 4.1.8 creating the microstructural architectures. Thus, as the electron beam parameters are altered, the regularity of the architectures varies as well.

This is similar to the SLM features that have been discussed for Ti-6Al-4V components fabricated by Thijs et al. [32], describing the parameter variations in terms of beam-scanning strategies and as well as the fabrication of Ni-base alloys via EMB described by precipitate architecture [9].

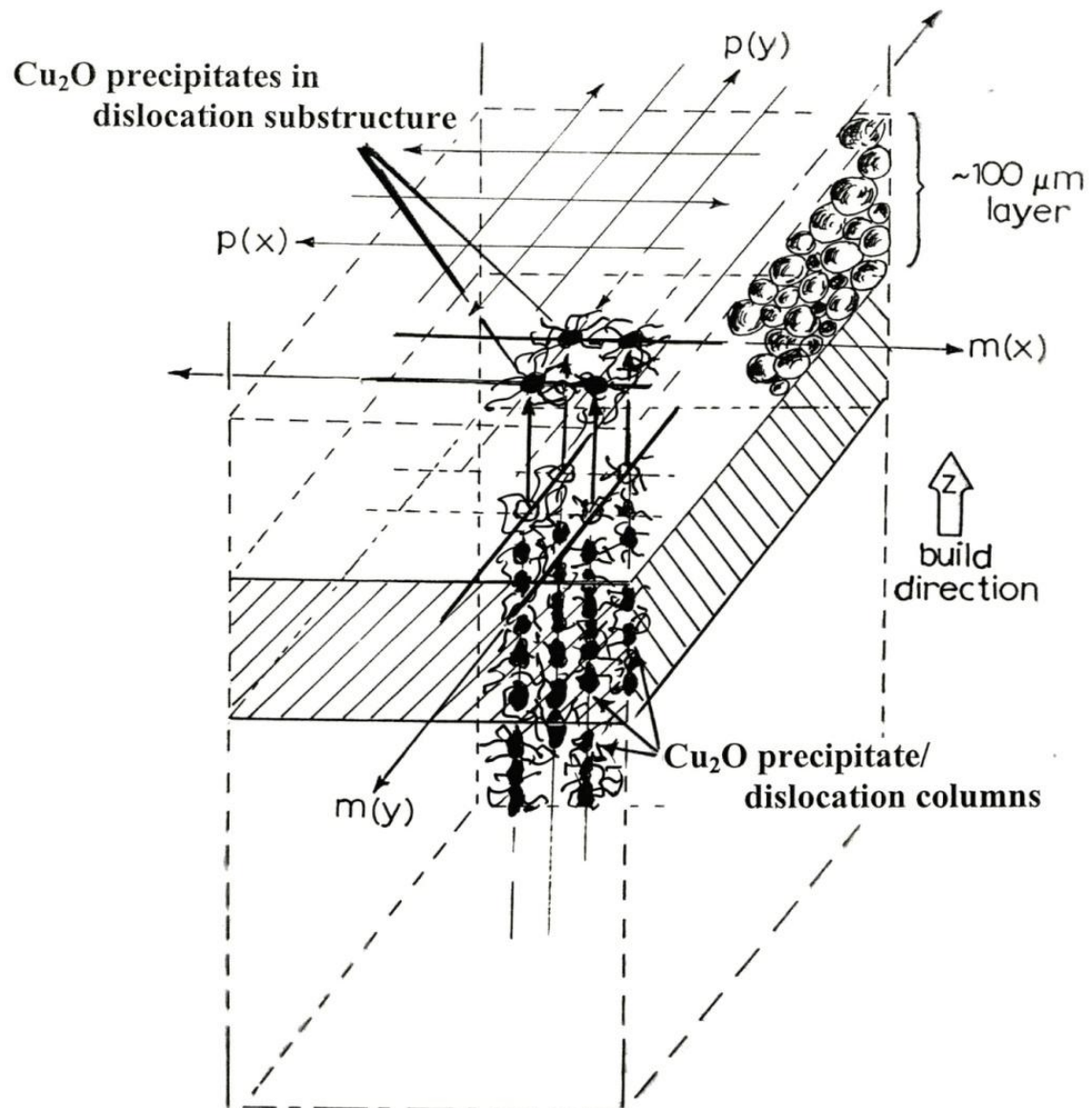


Figure 4.1.8. EBM scan geometry ideally forming precipitate-dislocation architectures in fabricated Cu components (Fig. 3.2.1). Preheat scans are marked $p(x)$, $p(y)$ while corresponding melt scans are denoted $m(x)$, $m(y)$

In the case of the rectangular EBM-fabricated component test blocks, irregular architectures can be seen in the 3-D optical microscope image composites as shown in Fig. 3.2.1 These irregular architectures can be represented by Figs. 4.1.9 and 4.1.10 and corresponds to the hottest energetic melt scan with a beam focus in comparison of the cylindrical specimen in Fig. 3.2.1(a). The architecture varies both in the horizontal and vertical reference planes in comparison to the previous Figs. 4.1.2 and 4.1.3, The Vickers microindentation hardness is essentially the same on average as that shown in Fig. 4.1.3.



Figure 4.1.9. Optical microscopy image (3D) composite section typical for extracted rectangular block specimens represented in Fig. 8(b).

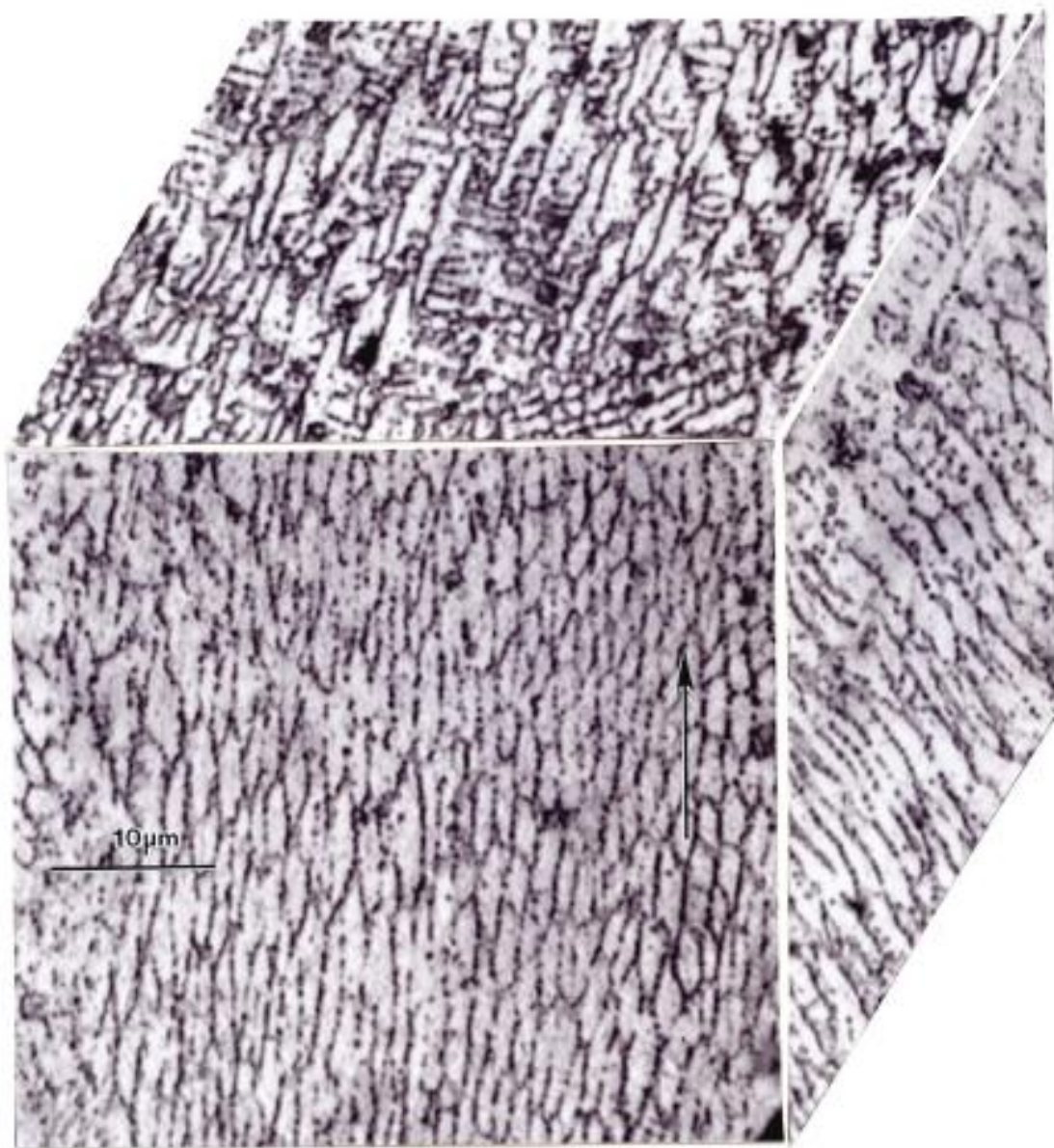


Figure 4.1.10 Higher Magnification 3-D image of Fig. 4.1.9

These 3-D image composites correspond to the electron beam focus offset of 35, demonstrates noteworthy embrittlement as evidenced by the fractures that replicate large intergranular fracture.

Figure 4.1.11 shows a failed section taken from the EBM copper components. The top view clearly outlines the large intergranular fracture areas and the lower 3-D cube composite is similar to Figs. 4.1.2

and 4.1.7. These columnar-like grains appear to be growing in two column portions roughly 0.8 cm in height and indicates some degree of epitaxial growth from the copper base plate.

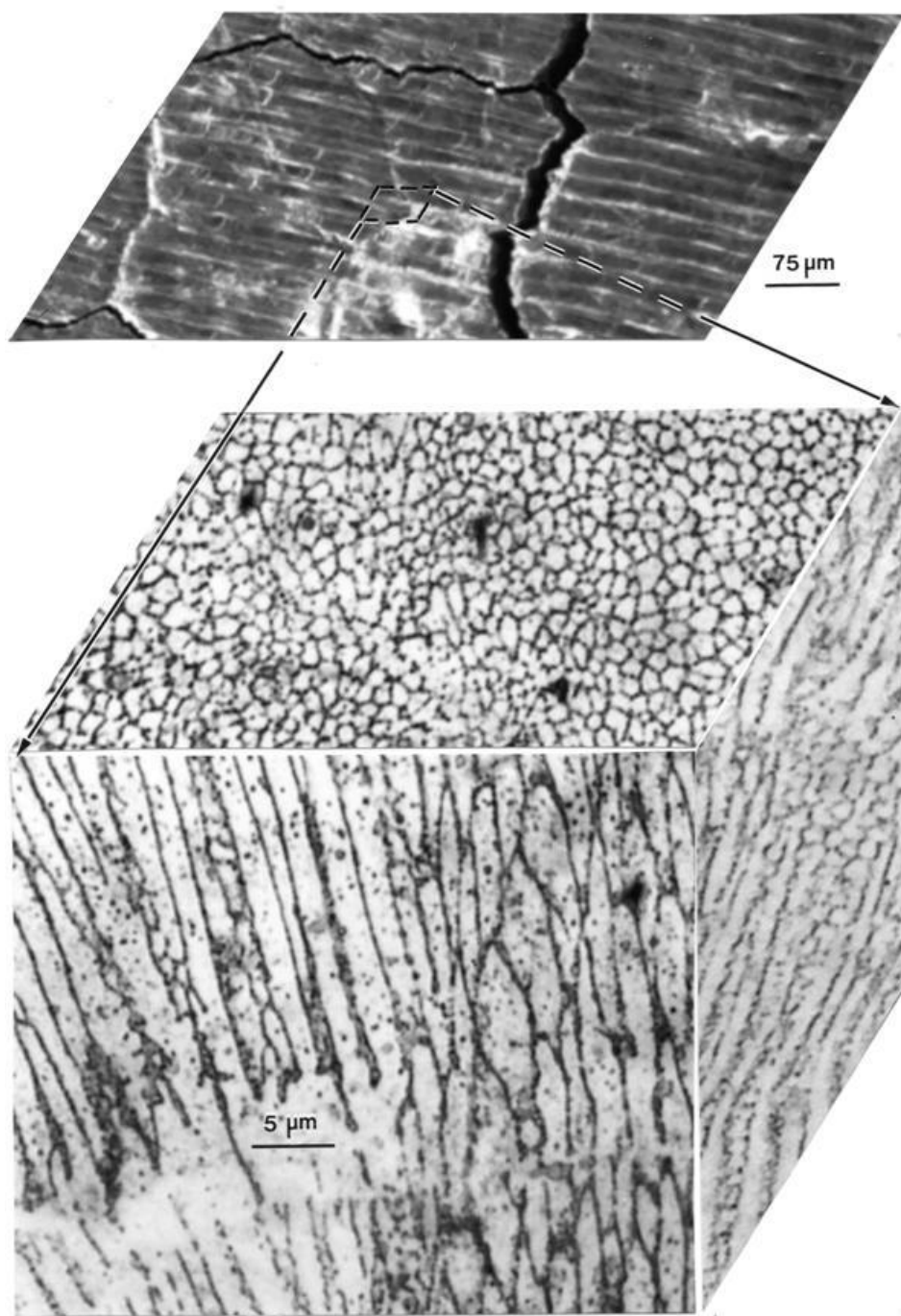


Figure 4.1.11. Spatial composite showing a typical horizontal reference plane section in a intergranular-like domain along with 3D image composite for the EBM component illustrated in Fig. 3.2.1(c)

In order to investigate this further, an area of the base plate was cut and mounted to allow images to be obtained from the back of the plate as well as from areas near the build or the build interface. These areas are illustrated by figure 4.1.13 in the views from 1-4, with 4 corresponding to the back of the base plate furthest from the build. In the first view (1) the top view is represented and it exhibits an intergranular-like fracture very similar to fig. 4.1.12. The following views (2) and (3) correspond to the upper base plate sections and about (~1 mm) just below the build base. The base plate bottom view corresponds to (4) showing not significant grain structure change, however it is clear to note that there is evidence of oxygen or oxygen precipitate segregation at the grains and grain boundaries especially the high-energy grain boundary portions. It is important to note that there is no cracking in the views corresponding to (2) and (3) in the straight-appearing, coherent twin boundaries. It is known that Copper has an interfacial free energy significantly less than the nominal grain boundary free energy which is roughly 75 vs. 750 mJ mm².

Hardness measurements were also taken between the base plate bottom and the top corresponding to (HV 57) for the base plate bottom and (HV 88) to the top, having an increase of 53%. In comparison to the precursor powder, the base plate bottom hardness is 26% softer respectively (HV 57 vs HV 72). This continues to support the precipitation-related hardening effect.

Although there is no clear evidence behind epitaxial growth for the build (as described in the fabrication of Ti-6Al-4V for the elongated grains by SLM fabrication [32]), the high amounts of oxygen content of the build has shown to have a high influence in the upper build grain structure.

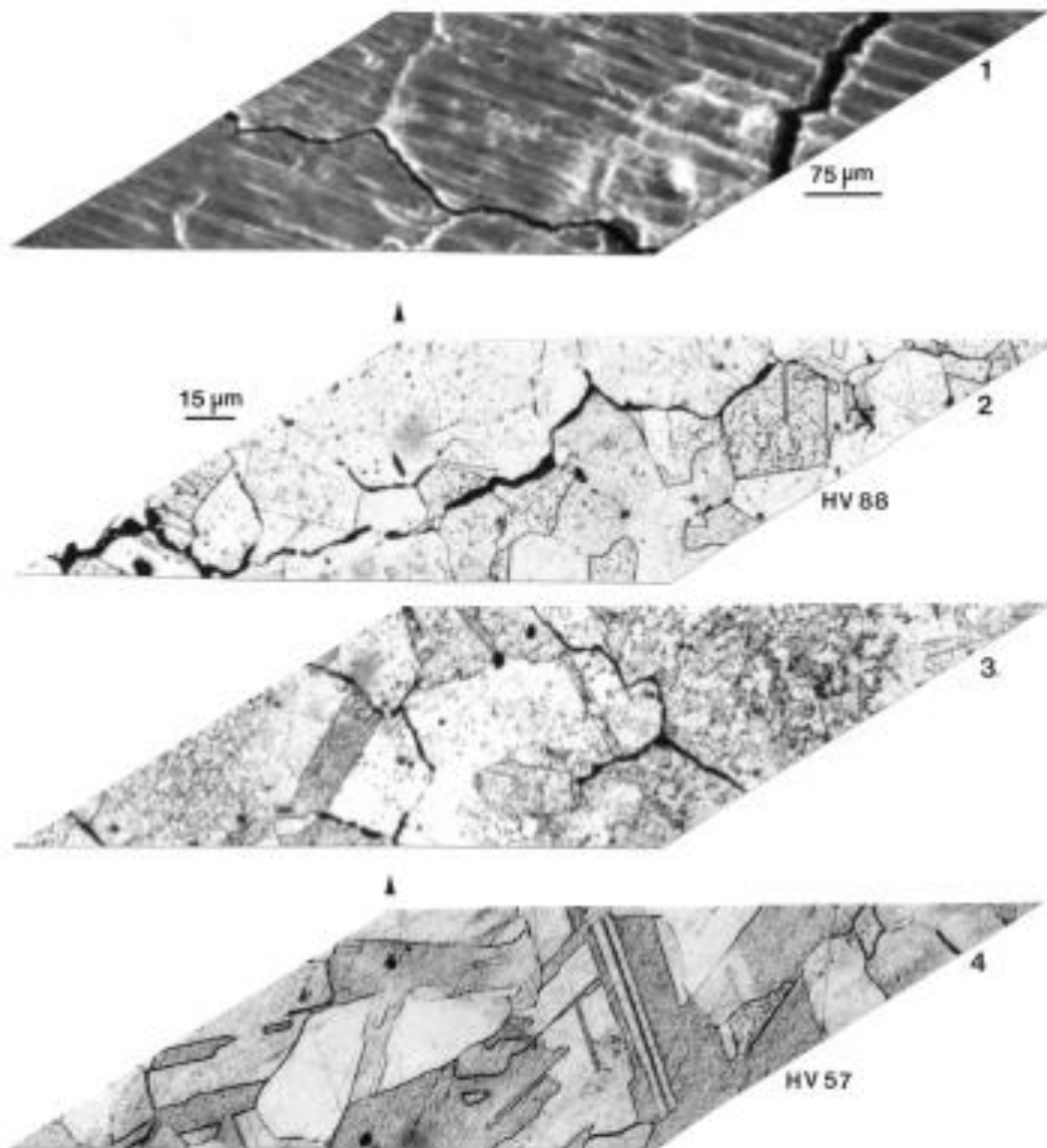


Figure 4.1.12 Section from Copper component fabricated by EMB (Fig. 3.2.1.(c)) illustrating the surface structure in relation to the top base plate microstructure, grain structure (2 and 3) and bottom of the plate (4) and microindentation hardness averages (HV) are also indicated.

Figure 4.1.13 shows apparent large, columnar grains suggested in figs. 4.1.11 and 4.1.12 do not correspond to single-crystal regimes but instead correspond to irregular, polycrystalline compositions having an average size of $\sim 60\ \mu\text{m}$ which is consistent with the precursor powder diameter and larger than the base plate grain size in fig 4.1.14 (2 and 3) of $\sim 15\ \mu\text{m}$. X-ray diffraction was also performed both in the horizontal and vertical reference planes.



Figure 4.1.13 Typical grain and sub-grain spatial precipitate-dislocation arrays in the horizontal reference plane corresponding to Figs.4.1.11 and 4.1.12. Note the irregular grain boundaries

4.2 TRANSMISSION ELECTRON MICROSCOPY ANALYSIS

As shown by figures 4.1.2 - 4.1.9 the cellular-like structures showing the etch pits having a regular cubic or rectangular pits similar to those in the grain boundaries of the precursor powder, TEM images provide more specifically delineated features. In figure 4.2.1 the horizontal plane shown by optical metallograph image reveals the cell/domain spatial reference for the TEM image which indicates a unique precipitate/dislocation-like cell structure. As previously mentioned, the non-coherent (Cu_2O) precipitates attached to dislocations (possibly generated at the precipitate/matrix interface) form these spatial arrays, which are selectively etched and form pits in the optical microscope and SEM images [30]. These domains contain high dislocation density of dislocation/vacancy loops indicated by the arrow near the top of the figure.

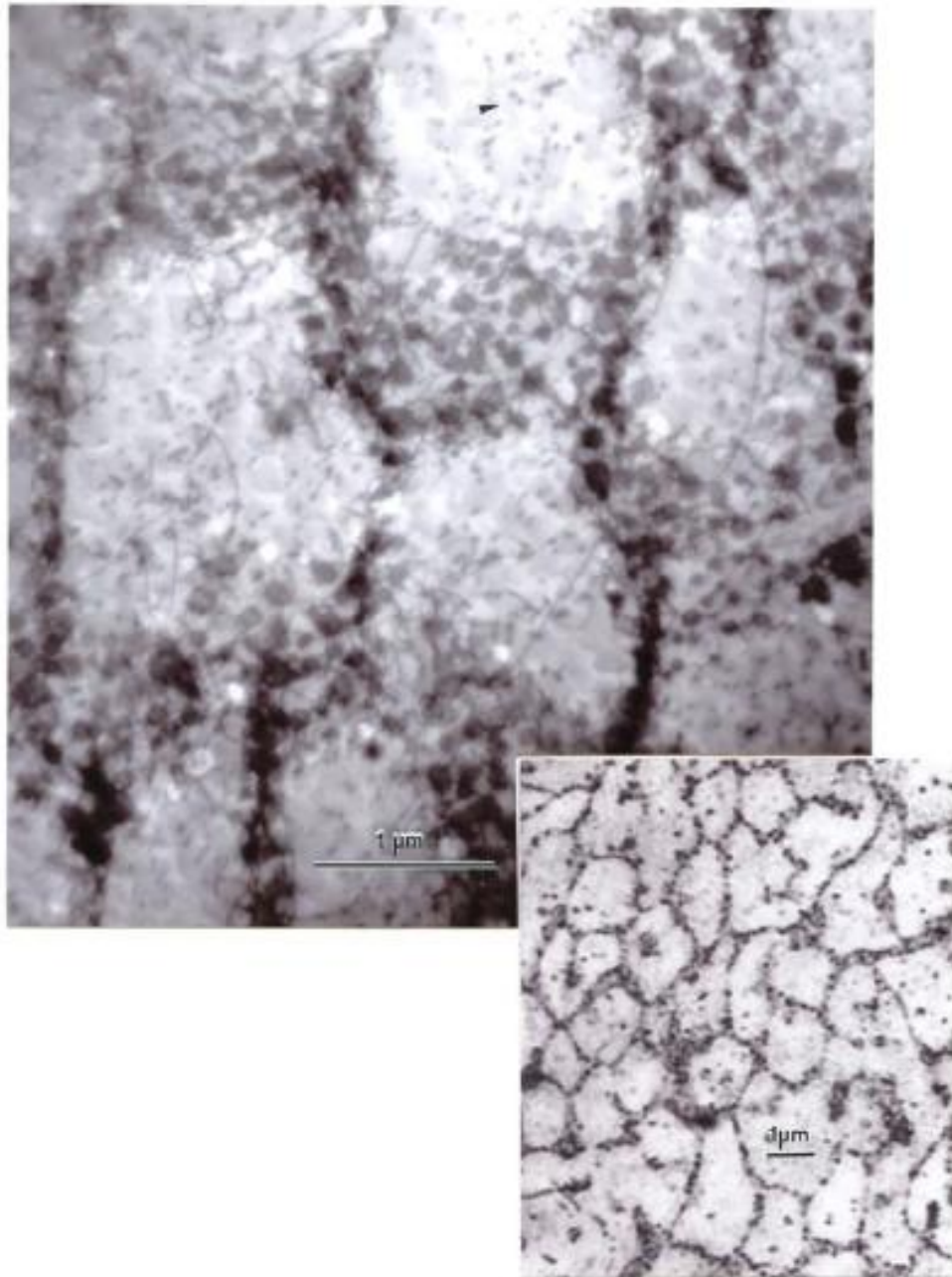


Figure 4.2.1 Illustrates TEM bright-field image showing precipitation-dislocation arrays corresponding to the horizontal reference plane as shown by the optical metallograph in the insert.

Figure 4.2.2 is another representation of these features including the vacancy dislocation loops indicated by the arrow at the bottom right. This figure shows the selective precipitates being etched out (white areas) and reveals the cubic or cube-related geometry as shown by the SEM analysis. SEM indicated that these precipitate particles had a relative common orientation which is confirmed by their geometric or crystallographic coincidence in the (1 1 0) grain surface orientation. This is indicated by the selected-area electron diffraction (SAED) pattern shown in figure 4.2.2. The SAED pattern indicates the operating reflection \mathbf{g} points out the $[\bar{1}10]$ trace direction, which shows many precipitates to be associated with along one edge.

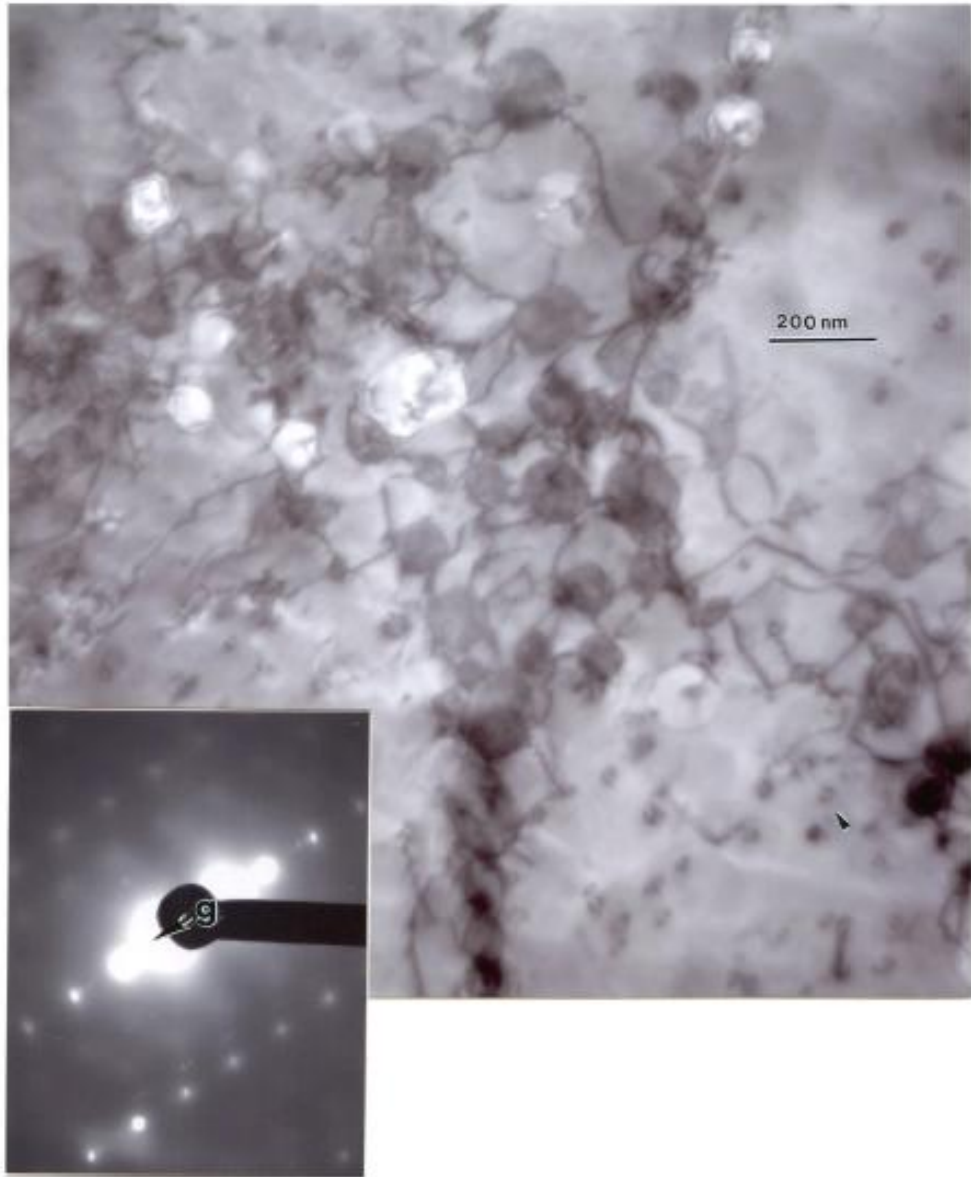


Figure 4.2.2 Magnified TEM bright-field image showing horizontal reference plane precipitate-dislocation array microstructure (as in Fig.4.1.5). The insert SAED pattern is a $[110]$ zone axis with $\mathbf{g} = [\bar{1}11]$. Arrow (lower right) shows typical dislocation loops

The precipitate-dislocation architecture in the vertical plane is associated with elongated cell-like precipitate/dislocation arrays as shown in Fig. 4.2.3 which are extremely visible by the precipitate etching along or closed to the build direction. This precipitate-dislocation (microstructural) architecture are closely associated with Fig. 4.1.5(b) and in coincide with Figs 4.2.1 and 4.2.2. The acid attack by the

etchant of the H_2SO_4 of the surface is stronger than the phosphoric acid etching in the TEM sample preparation. Thus on the precipitates create the etch pits. As noted these unique microstructures appear to be strongly related or the result of either precipitation in preheat and melt scans precipitates arranging during the melt scan or can be a cause of both.

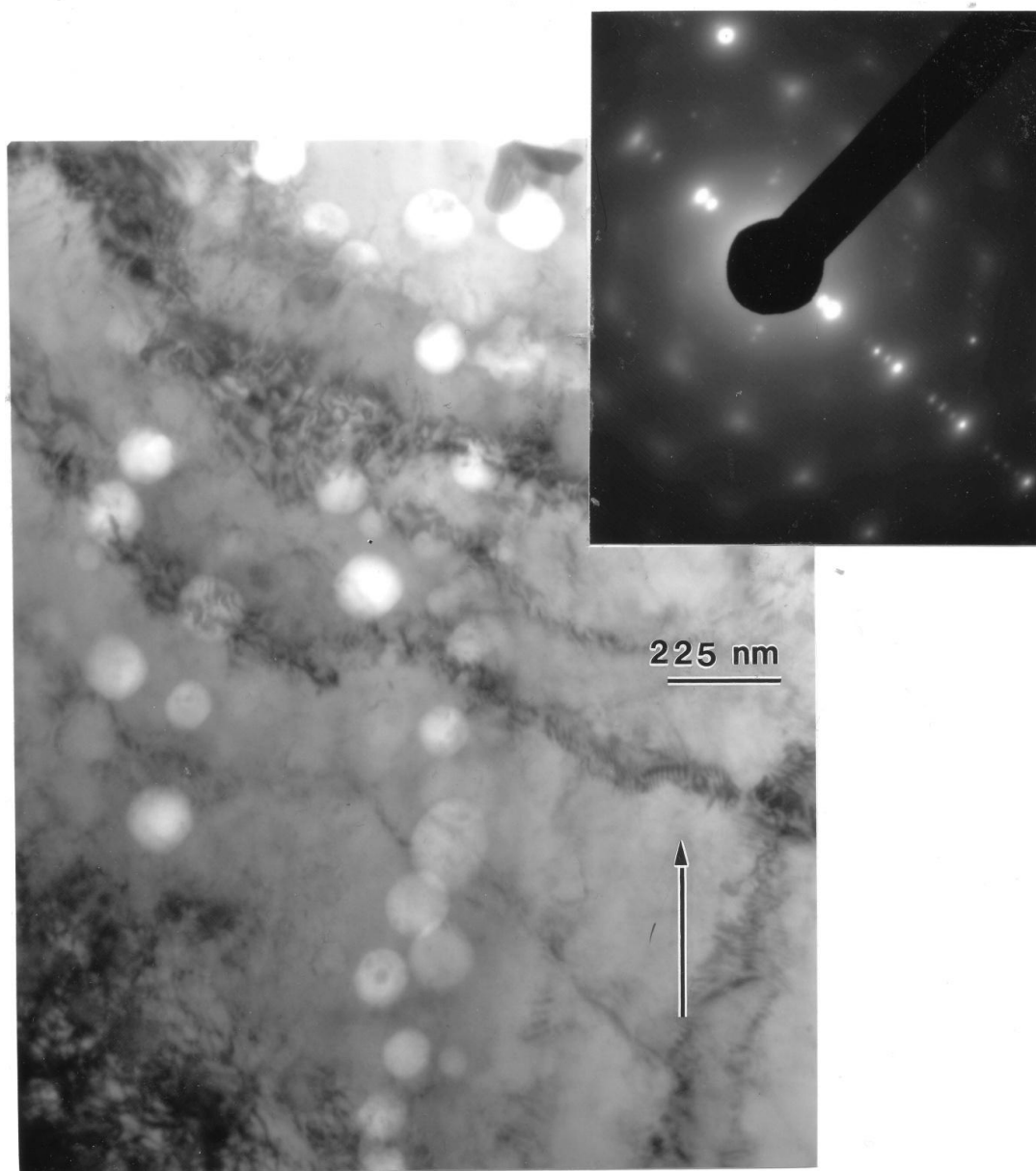


Figure 4.2.3. TEM bright-field image showing precipitate-dislocation architecture features in the vertical reference plane selective etching at precipitates. SAED pattern insert shows the Cu_2O precipitate diffraction spots.

Figure 4.2.4 and 4.25 illustrates the Cu_2O precipitates to have an average size of about 50 nm-100 nm. In certain regions these precipitates are highly concentrated in dense dislocation arrays, possibly generated due to the thermal stresses during the precipitation and rapid cooling during the EMB fabrication of the components.

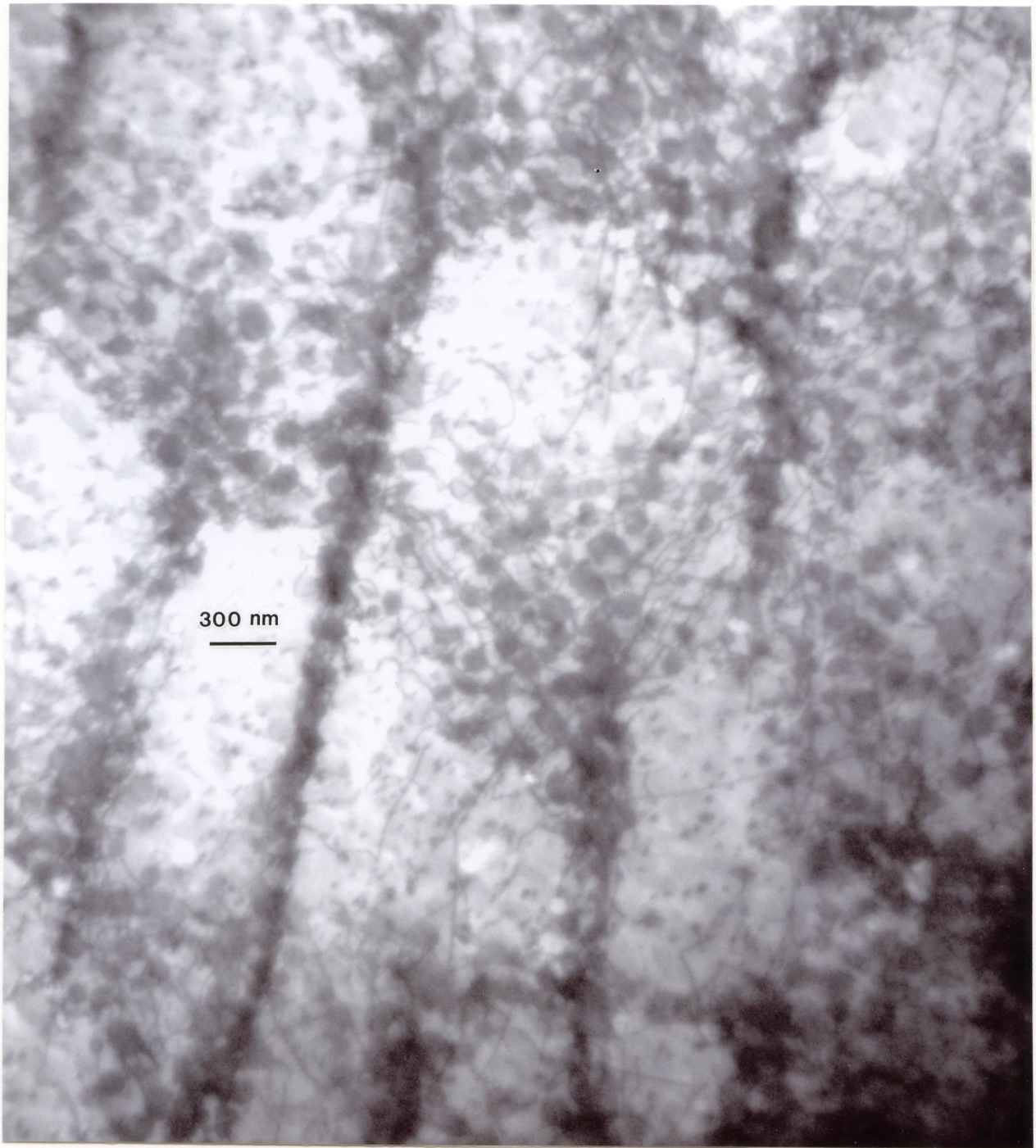


Figure 4.2.4. TEM bright-field image in the vertical plane

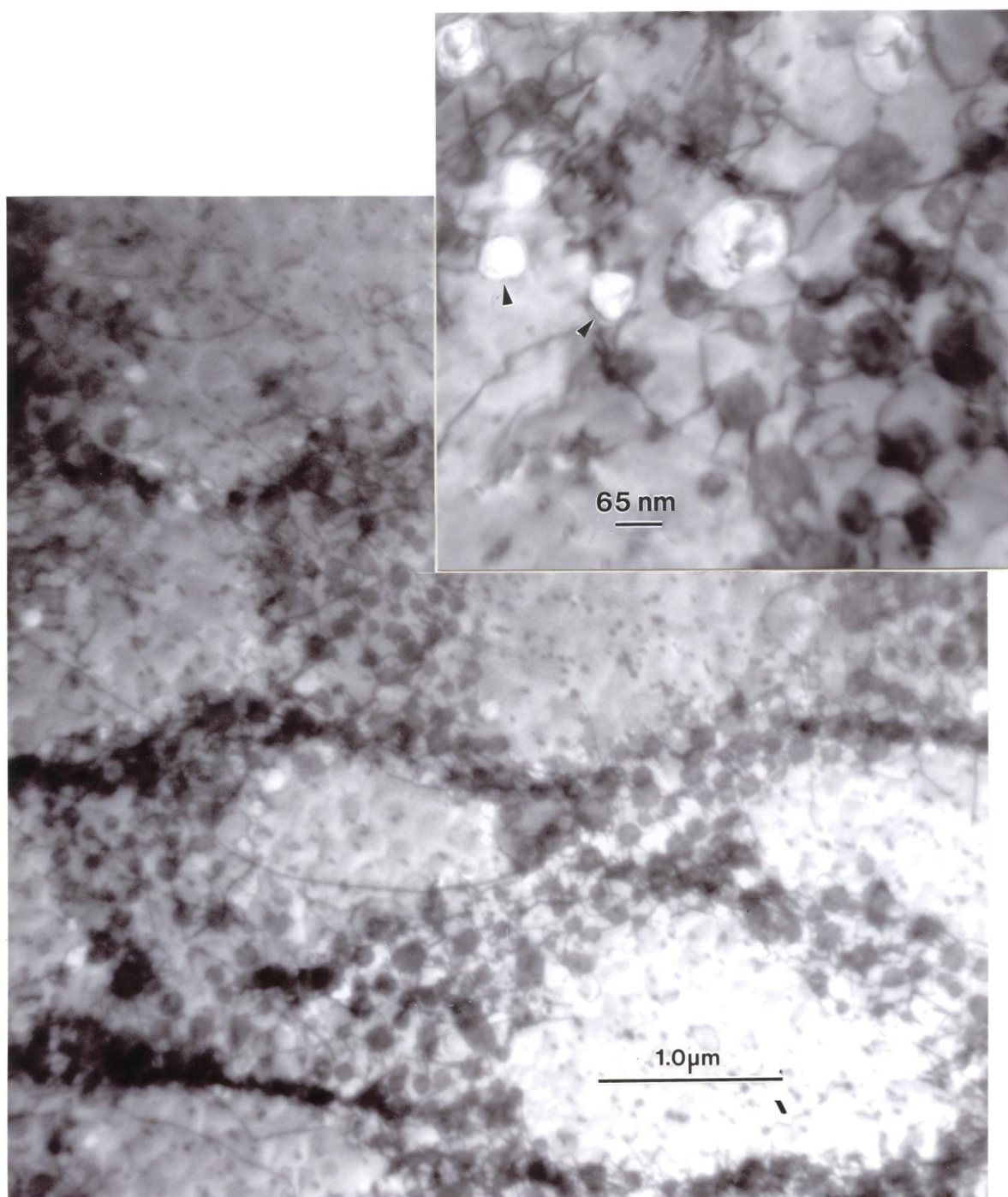


Figure 4.2.5. Illustrates TEM bright-field image in the horizontal plane. Arrow indicates the Cu_2O precipitate dissolution

4.3 OPEN- CELLULAR OF CU MESH AND FOAM SPECIMENS

Figure 3.6.2 illustrated the range of open cellular mesh and foams structures varying in densities that were fabricated for this project. These structures represented four different articulated mesh arrays. The most dense mesh array is illustrated by fig 4.3.1 as well as with a more dense solid section having a density of 8.02g/cm^3 . The presence of the Cu_2O along with the unmelted or unconsolidated regions contained in these components helped the reduction in density. As shown by the X-ray diffractometer spectral peaks, the volume fraction of Cu_2O precipitates was to be $\sim 2\%$. The anisotropic strut structures for reticulated mesh structures for isotropic stochastic foam samples are illustrated in Fig. 4.3.2. These structures are compared in corresponding to the reference planes of 90° and 45° in the samples views. The density for these foam arrays varied in densities of 0.73 to 1.70 g/cm^3 .

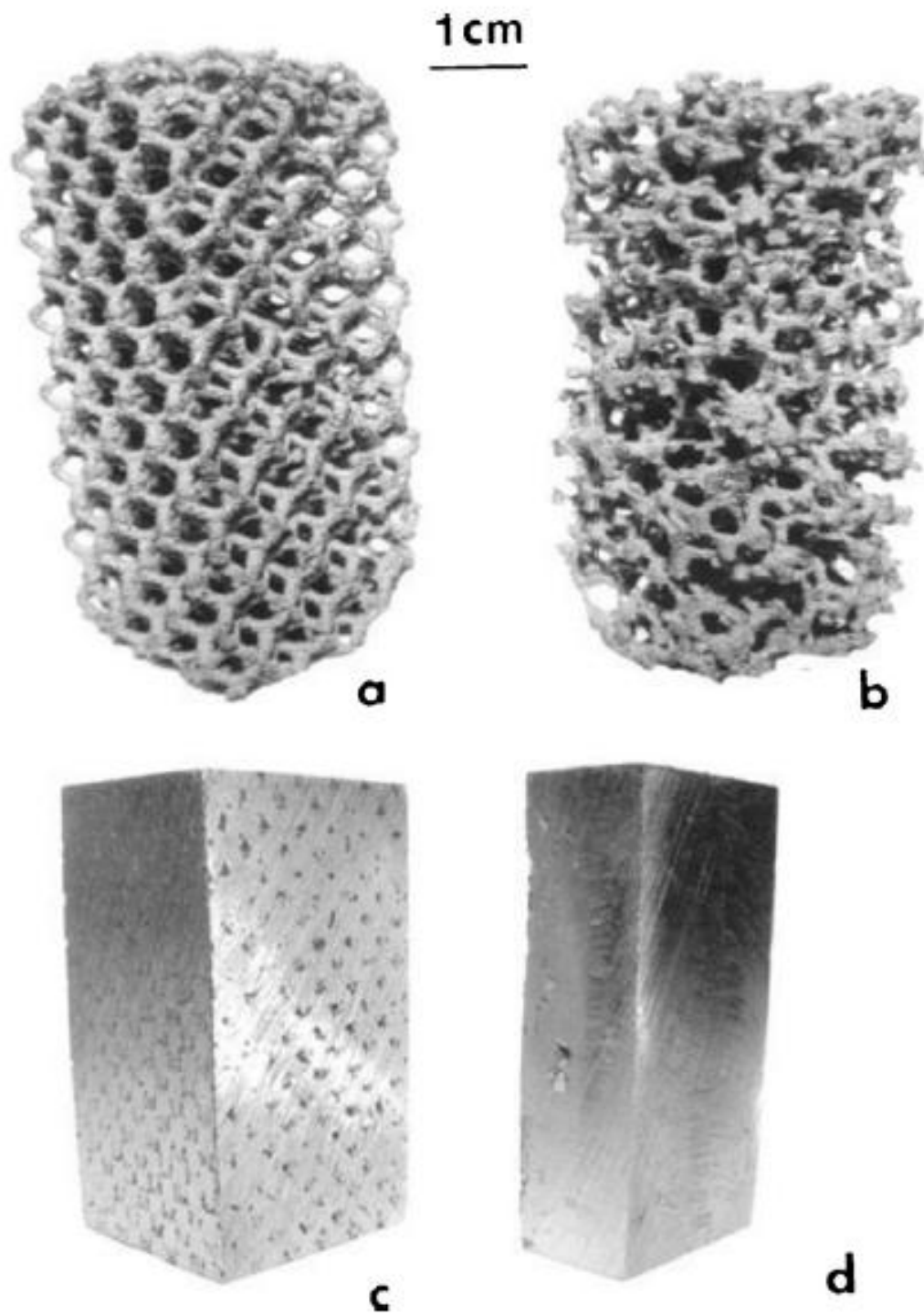


Figure 4.3.1 Reticulated mesh structures (a) and (c) in comparison to stochastic open cellular foam (b) and “solid build” (d)

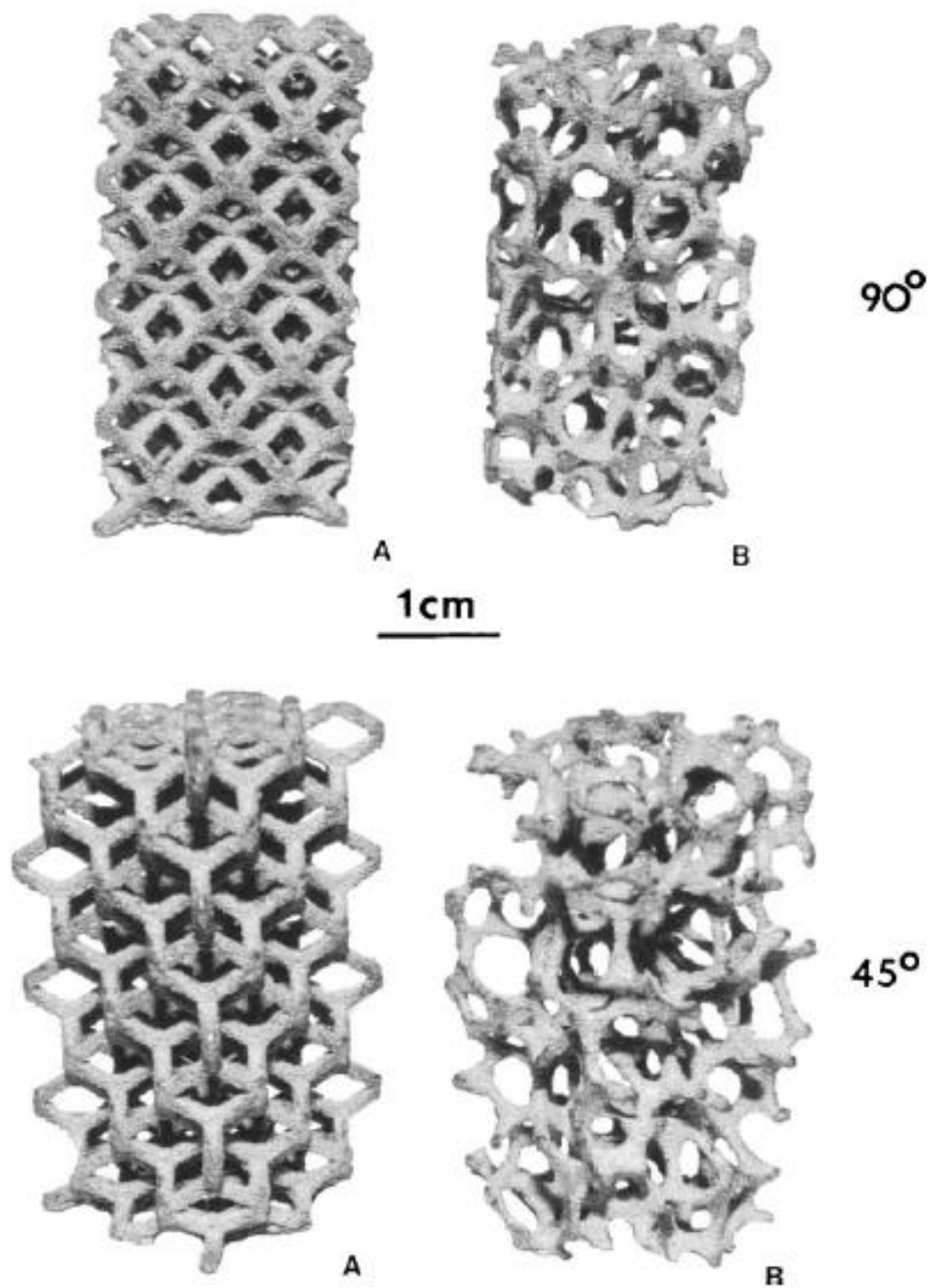


Figure 4.3.2 Comparison of EBM fabrication non-isotropic-geometry for reticulated mesh (a) and isotropic stochastic, open cellular foam samples (b) and 90° and 45° respectively.

Optical metallography was also performed on the mesh strut and foam ligament microstructures and was used in comparison as shown in figure 4.3.3. These microstructures analysis corresponds to the mesh and foam samples illustrated in 4.3.1 (a) and (b) respectively. It is important to note that the Cu_2O precipitate microstructural arrays continue to have an average spacing of $2\mu\text{m}$ in the horizontal plane in comparison to the same Cu_2O precipitate microstructures in the build vertical plane as indicated by the arrow. Note that these same microstructural regimes are also observed in the solid sample with the density of (8.02 g/cm^3).

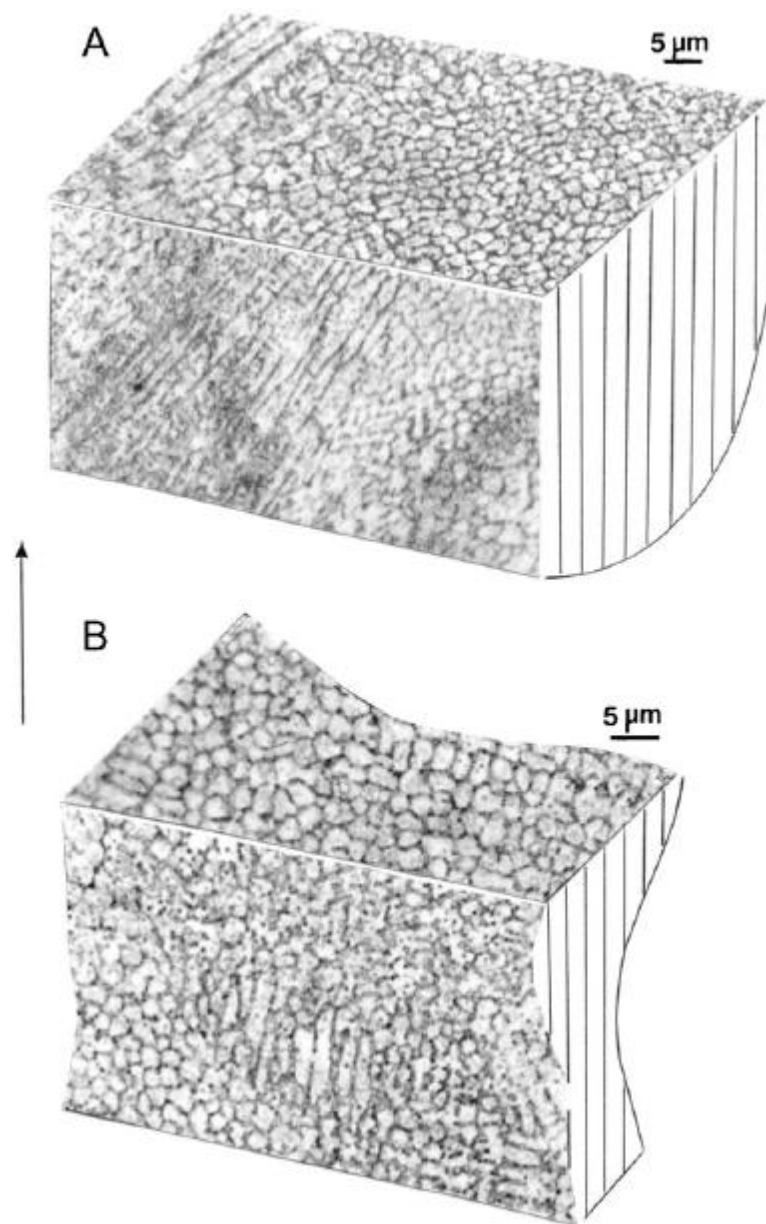


Figure 4.3.3 Horizontal and vertical plane constructions typical of reticulated mesh strut microstructure (a) and stochastic foam ligament microstructure. The build direction is shown by the arrow (left) [34]

Using the solid sample from Fig 4.3.1, TEM sections were prepared following the same method as with the Cu components procedure. These showed the same results as previously seen from the TEM analysis also performed on the Cu components fabricated by TEM. Figure 4.3.4 illustrates a bright-field TEM image consisting of Cu_2O precipitates as well as unique dislocation cell-like microstructures with a spacing of $\sim 2\ \mu\text{m}$. This cell-like arrays exhibit a homogeneous distribution of vacancies created by the rapid cooling during the build process.

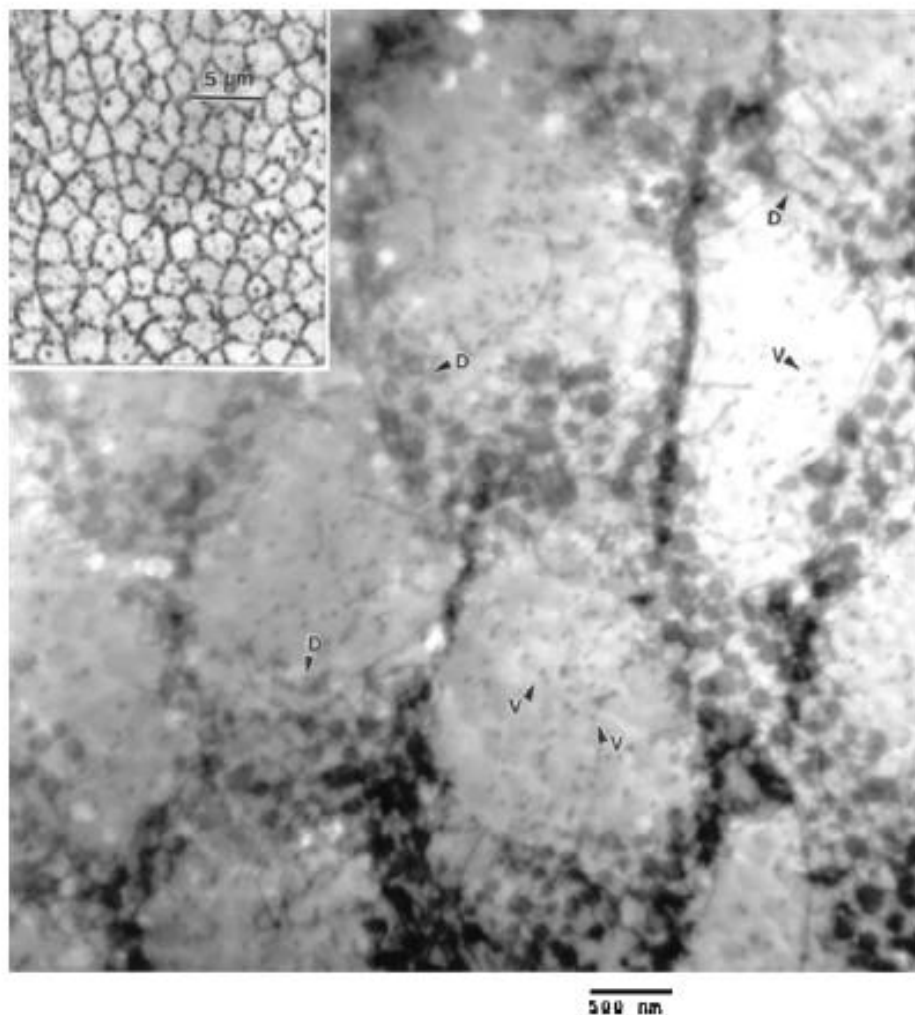


Figure 4.3.4 TEM bright-field image for horizontal plane microstructural arrays observed in the “solid” sample in Fig.4.3.1 ($8.02\ \text{g/cm}^3$) showing Cu_2O precipitate and dislocation cell-like microstructures. The insert shows a corresponding horizontal plane view of these microstructural arrays observed by optical metallography. Vacancies or vacancy dislocation loops are noted by arrows (V), while dislocations intermixed with the Cu_2O precipitates are noted by arrows labeled (D) [40]

The average hardness was measured in the residual microindentation hardness for the solid structure in the horizontal plane having a hardness measurement of HV 85 (0.85 GPa). The corresponding hardness of the precursor powder was measured as HV 72 (0.72 GPa) which resulted in a 18% increase from the precursor powder and the solid specimen. Furthermore the mesh strut and foam ligament hardnesses were also measured and resulted in having an average of HV 161 (1.61 GPa) and HV 70 (0.70 GPa) for all orientations. In comparison of annealed Cu and heavily deformed Cu respectively, the microindentation hardness ranges from HV 55 to HV 60 and annealed Cu was ~HV 115 (1.15 GPa). Considering that yield stress is estimated as $\sim HV/3$, the creation of Cu_2O microstructure in EBM-fabricated Cu mesh and foam components contributes to improved strength, both in tension and compression for the open cellular structures [34].

4.4 YOUNG'S MODULI (E)

Figure 4.4.1 compares the measured stiffnesses or Young's moduli (E) versus their corresponding densities for the reticulated mesh and stochastic foam samples in (a) and the relative stiffnesses (E/E_0) versus the relative densities (ρ/ρ_0) for the Cu samples for both the mesh and foam. The Cu foams were prepared by a lost carbonate sintering (LCS) process in powder metallurgy [35] as well as the measured values for Ti-6Al-4V mesh and foam samples fabricated by EBM. The extrapolated intercept for E to a density (ρ_0) of 8.9 g/cm^3 for the open cellular Cu samples correspond to $E_0=110 \text{ GPa}$ and 4.43 g/cm^3 as well [34]. As previously discussed, the slopes of these mesh and foam plots are illustrated in comparison to the idealized slope for stochastic, open cellular foams given by Ashby, where $n=2$. The Cu plots followed a corresponding slope of $n=2$ for the reticulated mesh samples and $n=2.4$ for stochastic foams. The LCS Cu foam data, corresponded to a slope of ~ 1.2 being way below the range of open-cellular Cu structures fabricated by EMB process. This slope was also below more conventional foam samples which is (~ 1.8). Ti-6Al-4V having a slope range in $n \equiv 2.2$ serving as a

calibration reference for the Cu stiffness measurements. Note these measurements are offset for the different open cellular materials in fig. 4.4.1.

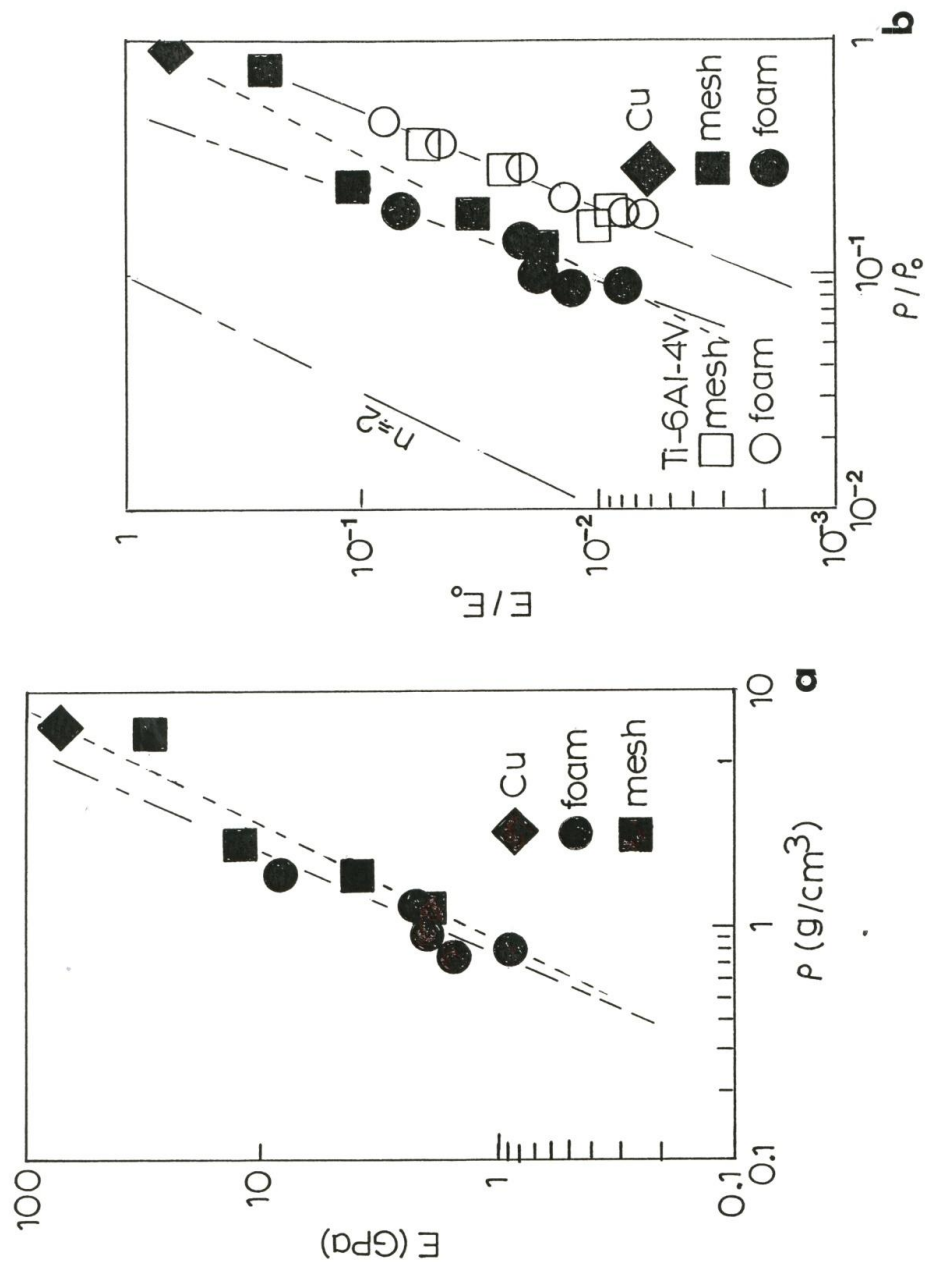


Figure 4.4.1 Stiffness (E) vs density (ρ) for Cu and relative stiffness (E/E_0) versus relative density (ρ/ρ_0) for Cu and Ti-6Al-4V. Portion of this data is from Murr et al. [28]

These multi-functional micro-strut/ligament sandwich or related multi-component assemblies, especially complex heat exchange devices and related thermally engineered materials structures [34]. The mesh or foam structure has conductive pathways through the strut or ligament microstructures which determines their buckling or collapse under stress. This has been explained by Ashby et al.[23] showing the relationship between the thermal conductivity and the relative density of a metal foam given by the equation:

$$K_s \left(\frac{\rho}{\rho_0} \right)^{1.8} < K_f < K_s \left(\frac{\rho}{\rho_0} \right)^{1.65}$$

where K_s and K_f correspond to the solid (fully dense) material thermal conductivity and foam conductivity, (ρ/ρ_0) is referred to the relative density. The heat transfer by metal foams due to thermal dispersion effect is proportional to the cell size and the thermal conductivity is proportional to the electrical conductivity which gives scales linearly with absolute temperature [34]. Thus the open cellular structures of Cu have gives one of the highest conductivities in both thermal and electrical which give electronic thermal management system. Figure 4.4.2 illustrate the Cu open strut and ligament microstructure showing considerable micro-roughness due to the unmelted and sintered surface particles. The heat transfer rate will highly depend upon the pore size and the strut or ligament surface roughness but the surface structure will also increase the surface area and thus allows for improvement in heat transfer.

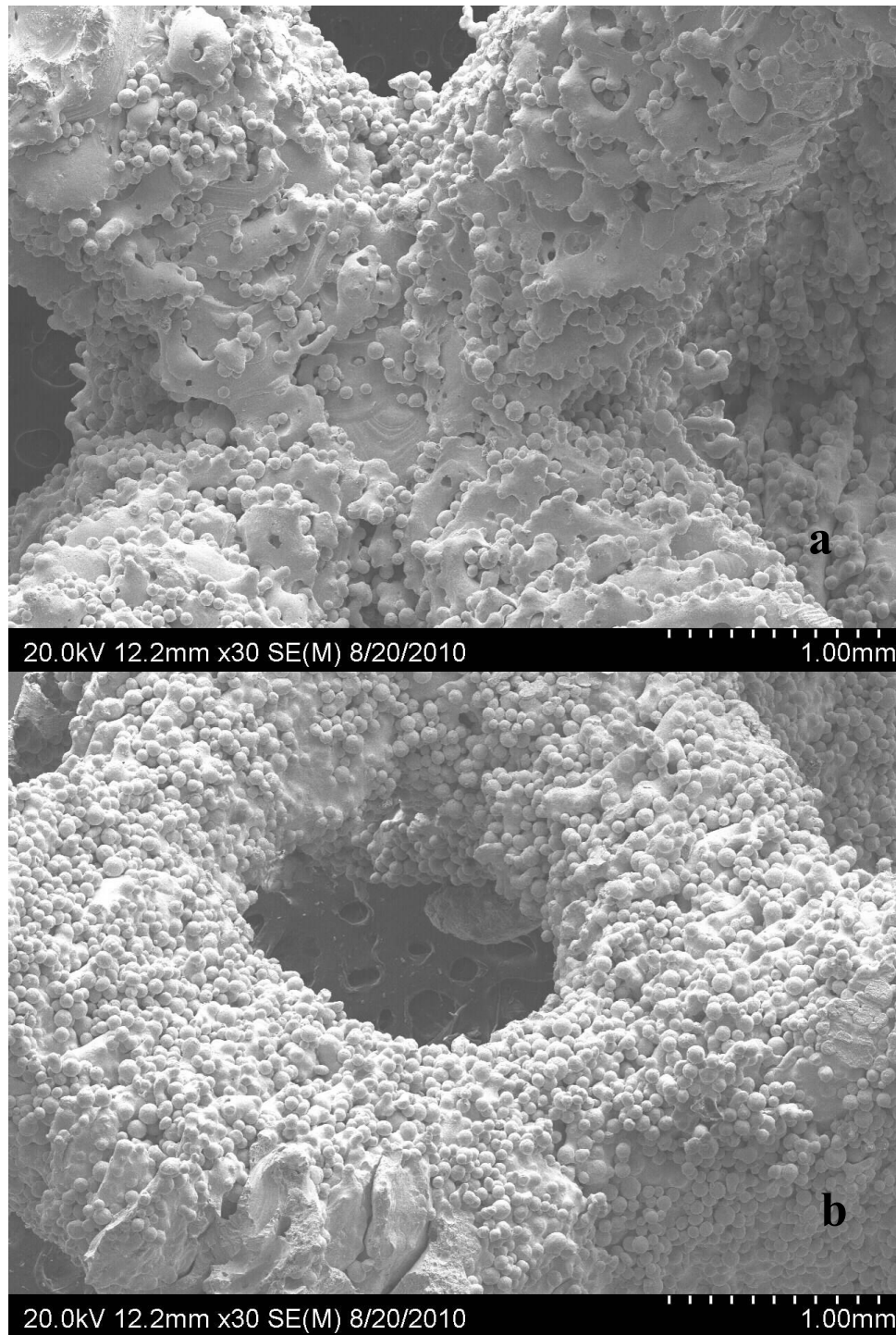


Figure 4.4.2 SEM image comparison for a reticulated mesh strut microstructure (a) and stochastic open cellular foam ligament microstructure (b).

However, this can also be influenced by cell crushing due to strut or ligament collapse which is terrible for brittle materials. This is illustrated in figure 4.4.3 which shows a classical ductile behavior for Cu mesh and foam structures showing shear type failure. This was performed by a modified Charpy test system. The ductile dimple fracture features are dominant in these regions. These dimple/shear dimple spacing averages a spacing $\sim 2\ \mu\text{m}$ which is consistent with the Cu_2O dislocation array and shown in previous figures.

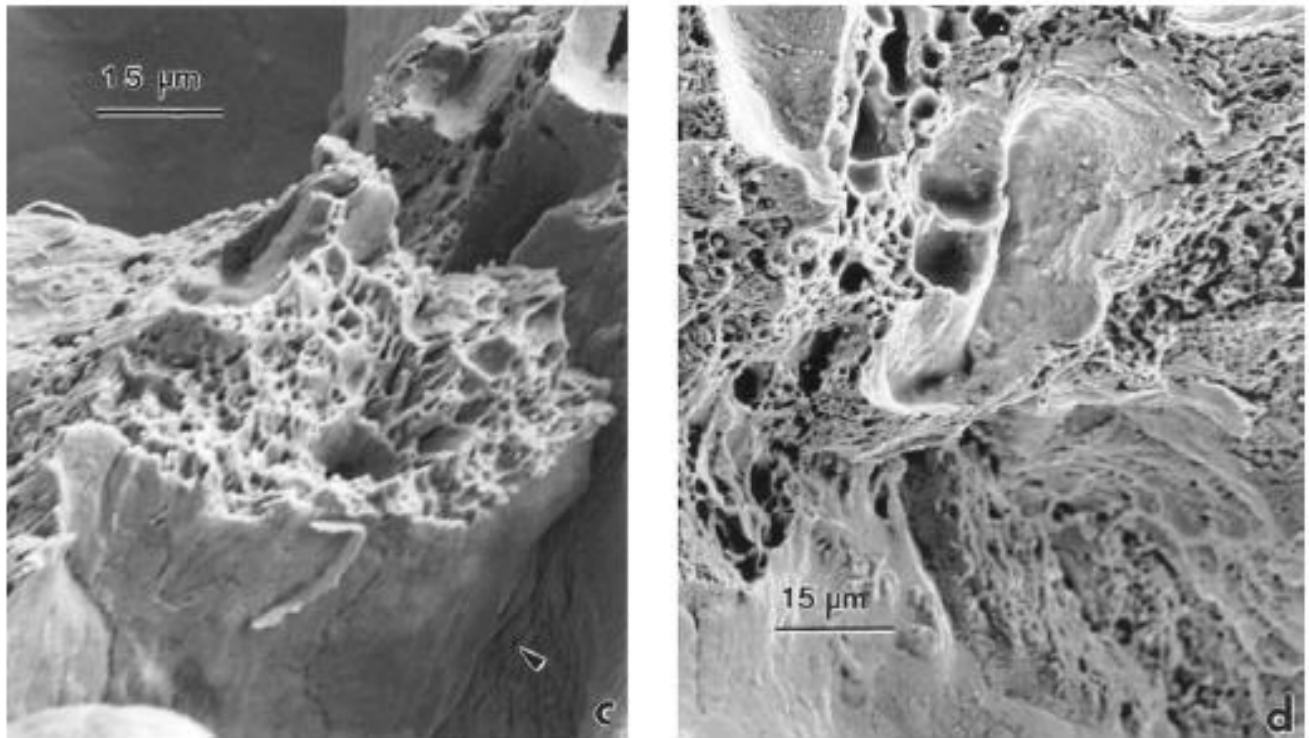


Figure 4.4.3. SEM micrograph showing impact-shear fractography views for mesh strut (c) and foam ligament (d) fracture surface.

Chapter 5

Summary and Conclusions

Cu atomized precursor powder containing high concentration of cuprite precipitation has been observed to form novel precipitate-dislocation architecture in the components fabricated by AM using EBM. This can be performed by optimizing the process parameters which can lead to controlled microstructural architectures with novel properties and performance features. These novel properties have also been supported by the Co-base and Ni-base alloys [30]. These cell-like equiaxed arrays in the horizontal reference plane perpendicular to the build direction having dimensions ranging from ~1 to 3 μ m allowing for an increase in hardness in EBM – fabricated Cu, ranging from a base plate hardness of 57 to an EBM part of HV 88. The precursor powder had a hardness average of 72 corresponding to a hardness extension of 54%. This method of achieving this microstructural architecture can be used to extend the materials science and engineering paradigm involving materials structure-properties-processing-performance.

MATERIALS SCIENCE & ENGINEERING PARADIGM EXTENSION

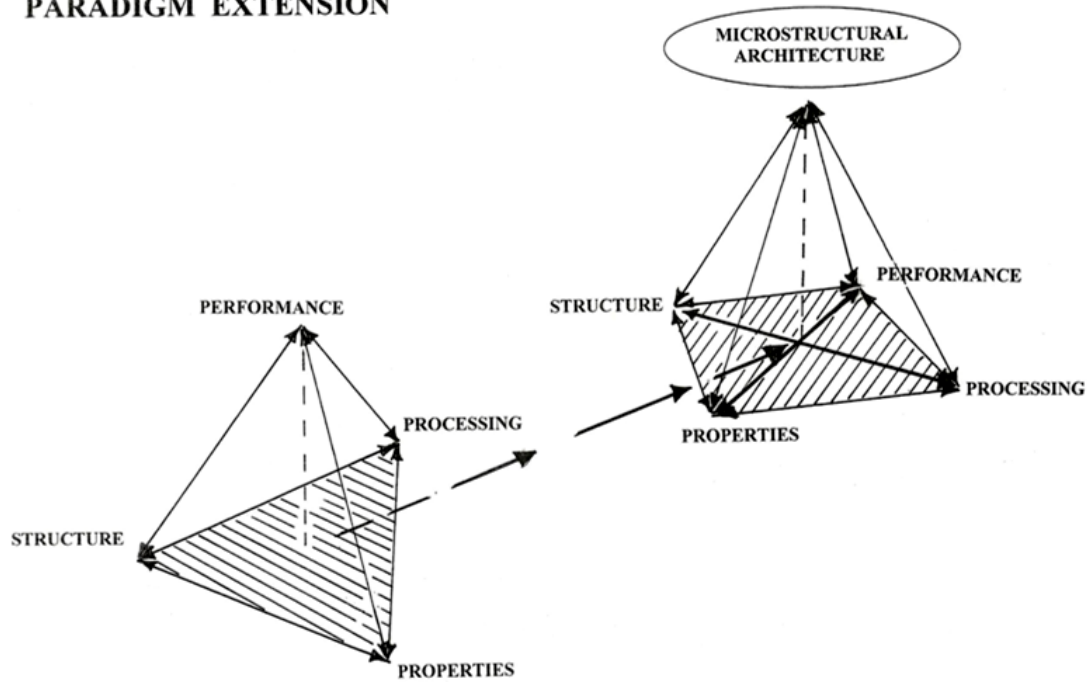


Figure 5.1: Novel property-performance an extension for the materials, science and engineering paradigm: structure – properties – processing – performance plus architectures

In addition, open cellular structures-reticulated meshes and stochastic foams by additive manufacturing using electron beam melting from precursor Cu powder were fabricated containing Cu_2O precipitates due to the Cu powder. These precipitates and the formation of additional precipitates created in the EBM melt scan process contributed to hardening and the strength of mesh struts and foam ligaments. The stiffness or Young's moduli (E) for the Cu open cellular structures vary with density and relative stiffness versus relative density plots for Cu compared very closely to Ti-6Al-4V for open cellular structures both mesh and foam. The Cu reticulated mesh structures showed a slope of $n=2$ in contrast to a slope of $n=2.4$ for the stochastic Cu foams which follow the ideal open cellular foam slope of $n=2$ given by Gibson-Ashby foam model.

The ability to fabricate complex monolithic structures and devices fabricated by additive manufacturing via electron beam melting composed of various open cellular structures suggest a wide range of thermal management or heat exchange applications. This is due to the higher thermal and electrical conductivity of Cu and its significantly higher operating temperature in comparison to Al or Al alloys.

References

- [1]. ASM International. ASM Handbook., Alloy Phase Diagrams, 2004, Vol. 03, pp. 752-754.
- [2]. O. D. Neikov, S. S. Naboychenko, G. Dowson., “*Handbook of Non-Ferrous Metal Powder: Technologies and Applications*, Chap. 5, Chap.16 (2009), Elsevier Publishing Co.,Oxford, UK
- [3]. ASM International. ASM Handbook, Properties and Selection: Nonferrous Alloys and Special-Materials, 2004, Vol. 02, pp. 1275-1278.
- [4]. ASTM. “ASTM F2792-10 Standard Terminology for Additive Manufacturing Technologies.” American Society for Testing and Materials (ASTM), <http://www.astm.org/DATABASE.CART/HISTORICAL/F2792-10.htm>.
- [5]. Lim, S, Buswell, R.A, Le, T.T, Austin, S.A, Gibb, A.G.F, Thorpe, T, Developments in construction-scale additive manufacturing processes, *Automation in Construction.*, in press.
- [6]. Wohlers Report 2009, State of the Industry Annual Worldwide Progress Report on Additive Manufacturing, Wohlers Associates, 2009, <http://www.wohlersassociates.com/>, ISBN 0-9754429-5-3
- [7]. D. T. Pham, S. S. Dimov, Rapid manufacturing, Springer-Verlag, 2001, ISBN 1-85233-360-X, page 6
- [8]. <http://www.bath.ac.uk/pr/releases/replicating-machines.htm>
- [9]. Strondl, A, Fischer, R, G. Fronmeyer, Schneider, A. Mater Sci Eng A,2008; 480 138–147.
- [10]. Ozmat, B., Leyda, B. and Benson, 2002, “Thermal Applications of Open Cell Metal Foams”, Personal communications with ERG Materials and Aerospace Corp. Oakland, CA.
- [11]. L.E. Murr, S.M. Gaytan, F. Medina, H. Lopez, E. Martinez, B.I. Machado, D.H. Hernandez, L. Martinez, M.I. Lopez, R.B. Wicker, J. Bracke, Philos. Trans. R. Soc. A 368 (2010) 1999–2032.
- [12]. Boomsma, K., Poulikakos, D. and Zwick, F., 2003, “Metal Foams as Compact high Performance Heat Exchangers”, *Mechanics of Materials*. Vol.35, pp1161-1176
- [13]. Bastawros, A F., 1998, “Effectiveness of Open-Cell Metallic Foams for high Power Electronic Cooling”, *Proceeding Symposium on the Thermal Management of Electronics*, IMECE. Anaheim, CA.
- [14]. Writz, R.A., 1997 “A Semi-Empirical Model for Porous Media Heat Exchanger Design”, *Preceedings of the American Society of Mechanical Engineers National Heat Transfer Conference*, Baltimore, MD.

- [15] J.Banhart, JOM 52 (2000) 22-27.
- [16] O. Cansizoglu, O. Harrysson, D. Cormier, H. West, T. Mahale, Mater. Sci. Eng. A492 (2008) 468.
- [17] J. Banhart, J. Baunmeister, Production methods for metallic foams in: D.S. Schwartz, D.S. Shih, A.G. Evans, H.N.G. Wadley (Eds.) Porous and Cellular Materials for Structural Applications, MRS Symposium Proceedings, 521 (1998) p.121-132.
- [18] J. Baumeister, J. Banhart, M.Weber, Mater. Des. 18 (4) (1997) 217–220.
- [19] A.H. Brothers, D.C. Dunand, Scripta Mater. 54 (2006) 513–520.
- [20] H.N.G.Wadley, Proceedings of the International Conference on Cellular Metals and Metal Foaming Technology, Bremen, Germany, 2001, pp. 137–146.
- [21] H.N.G. Wadley, N.A. Fleck, A.G. Evans, Compos. Sci. Technol. 63 (2003) 2331–2343.
- [22] D.T. Queheillalt, H.N.G.Wadley, Acta Mater. 53 (2005) 303–313.
- [23] M.F. Ashby, A. Evans, N.A. Fleck, L.J. Gibson, J.W. Hutchinson, H.N.G. Wadley, Metal Foams: A Design Guide, Butterworth-Heinemann, Boston, 2000.
- [24] L.J. Gibson, M.F. Ashby, Cellular Solids: Structure and Properties, Cambridge Univ. Press, New York, 1997.
- [25] H.P. Degischer, B. Kriszt (Eds.), Handbook of Cellular Metals, Wiley, Weinheim, 2002.
- [26] A. Ghosh, T. Sanders, D. Claar (Eds.), Processing and Properties of Lightweight Cellular Metals and Structures, TMS, Warrendale, PA, 2002.
- [27] D.C. Dunand, Adv. Eng. Mater. 6 (6) (2004) 369.
- [28] L.E. Murr, S.M. Gaytan, F. Medina, E. Martinez, J.L. Martinez, D.H. Hernandez, B.I. Machado, D.A. Ramirez, R.B. Wicker, Mater. Sci. Eng. A 527 (2010) 1861-1868.
- [29] MCP Tooling Technologies Ltd., England, MCP realizer datasheet, <http://www.mcp-group.com/rpt/rpttslm1.html>.
- [30] Ramirez, D.A, Murr, L.E, Martinez, E, Hernandez, D.H, Martinez, J.L, Machado, B.I, Medina, F, Frigola, P, Wicker, R.B, Acta Mater. 59 (2011) 4088-4099.
- [31] Murr, L.E, Martinez, E, Gaytan S.M, Ramirez, D.A, Machado, B.I, Shido, P.W, Metall and Mat Trans A (2011) 42: 3491-3508

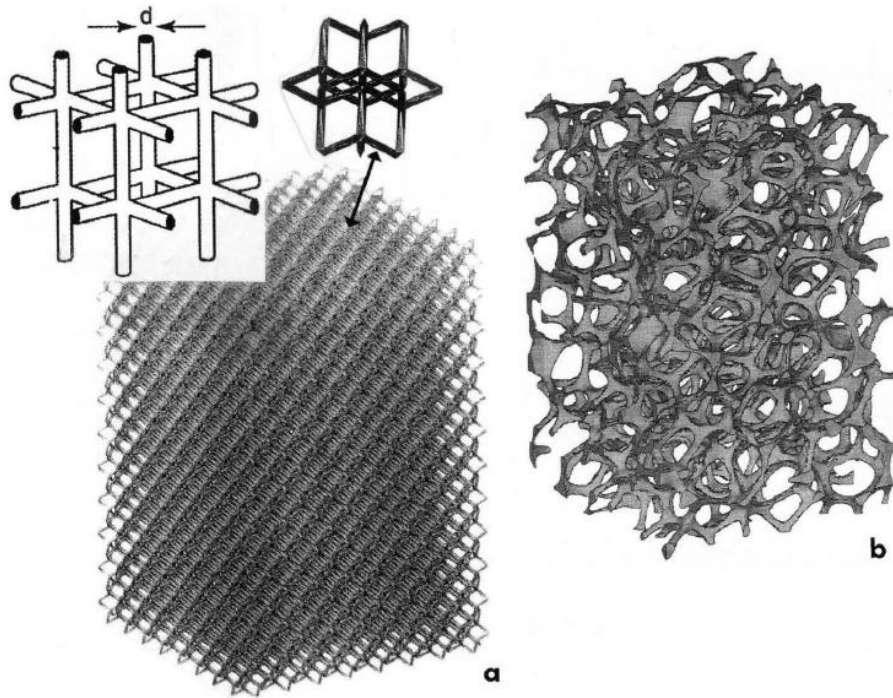
- [31] L. J. Gibson and M. F. Ashby, *Cellular solids: structure and properties*, 1997, New York, Cambridge Univ. Press.
- [32] Thijs, L, Verhaeghe, F, Craeghs, T, Hambeeck, J.V Kruth, J-P. Acta Mater, 58 (2010), pp. 3303–3312
- [33] Verhaeghe, F, Craeghs, T, Heulens, J, Pondelaers, L. Acta Mater, 57 20 (2009), pp. 6006–6012.
- [34] Ramirez, D.A, Murr, L.E, Martinez, Li, S.J, Tian, Y.X, Martinez E, Martinez J.L, Machado, B.I, Medina, F, Gaytan, S.M, Frigola, P, Wicker, R.B, Mater. Sci. Eng. A 528 (2011) 5379-5386.
- [35] M.A. El-Hadek, S. Kaytbay, Int. J. Mech. Mater. Res. 4 (2008) 63–69.
- [36] Murr, L.E., Li S., Tian Y., Amanto, K, Martinez, E, Medina F, Materials 4 (2011) 782-790

Appendix

Simple Unit Cell



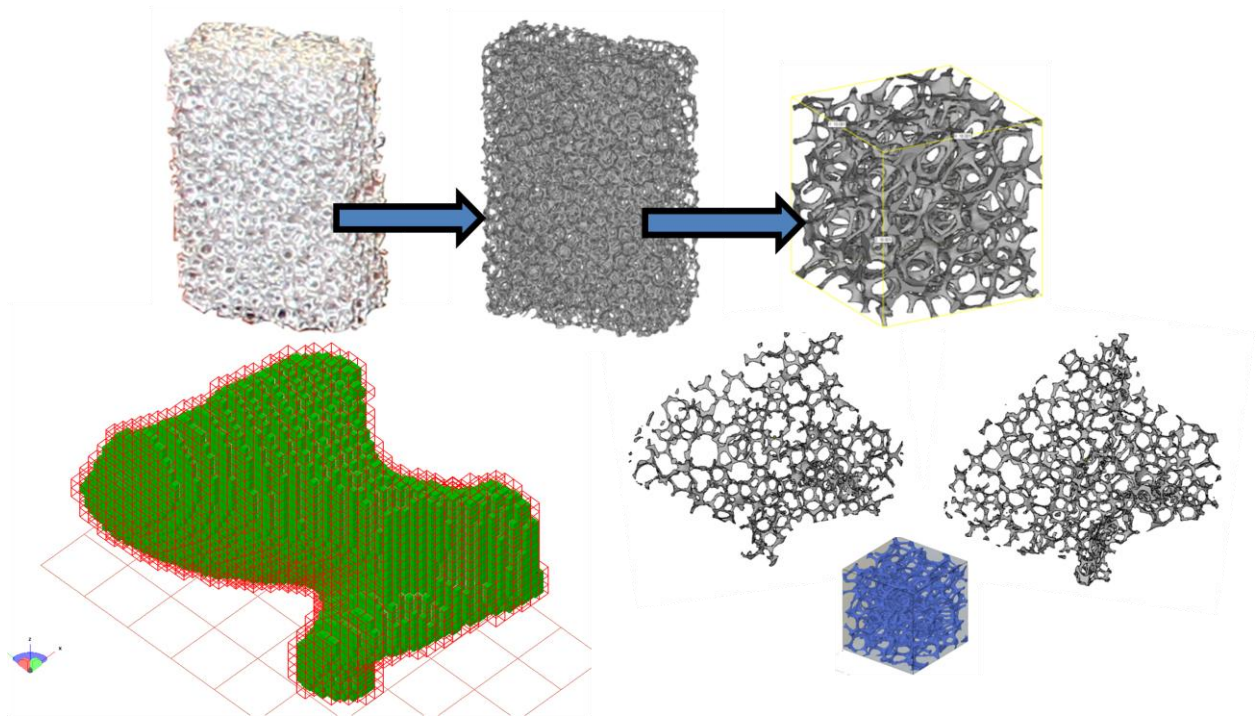
Different type of unit cells



Samples for EBM fabrication of open-cellular structures using CAD. (a) Using Materialise™ software shows the fabrication of strut structure indicated by arrow. (b) microCT scan element of cellular foam model.

Advantages	Disadvantages
<ul style="list-style-type: none"> – Controlled structures – Lightweight – Reduces the number of process steps in manufacturing 	<ul style="list-style-type: none"> – Hard to design functional cells – Limited designs – Cleaning – Non isotropic structure

Foam Process



Advantages	Disadvantages
<ul style="list-style-type: none"> – Random – Easy to reproduce – Semi isotropic structures 	<ul style="list-style-type: none"> – Surface geometry dictated by repeating cell and cell size

DYNAMIC YOUNG’S MODULUS MEASUREMENT

dynamic E	$E = \frac{\sigma}{\epsilon}$ (under vibratory conditions)
For a cantilever beam of length L with a clamped boundary condition:	
$E = \frac{12\rho L^4 f_r^2}{a_n^2 t^2}$: f_r = resonant frequency	
ρ	ρ = sample density; a_n is a characteristic number of the nth mode; t is the beam thickness (standardized specimen dimensions)
$E = c\rho f_r^2$	C is a measuring constant

Novel precipitate–microstructural architecture developed in the fabrication of solid copper components by additive manufacturing using electron beam melting

D.A. Ramirez^{a,b}, L.E. Murr^{a,b,*}, E. Martinez^a, D.H. Hernandez^a, J.L. Martinez^a,
B.I. Machado^a, F. Medina^b, P. Frigola^c, R.B. Wicker^b

^a Department of Metallurgical and Materials Engineering, University of Texas at El Paso, El Paso, TX 79968, USA

^b W.M. Keck Center for 3-D Innovation, University of Texas at El Paso, El Paso, TX 79968, USA

^c Radiabeam Technologies, Santa Monica, CA 90404, USA

Received 25 June 2010; received in revised form 17 December 2010; accepted 10 March 2011

Available online 2 April 2011

Abstract

The fabrication of Cu components by additive manufacturing using electron beam melting (EBM) from low-purity, atomized Cu powder containing a high density of Cu₂O precipitates exhibits a novel example of precipitate–dislocation architecture. Such architectures are seen by optical metallography, and scanning and transmission electron microscopy, to consist generally of equiaxed precipitate–dislocation cell-like arrays (1–3 μm) in the horizontal reference plane perpendicular to the build direction with elongated or columnar-like arrays extending from ~12 to >60 μm in length and corresponding spatial dimensions of 1–3 μm. The hardnesses for these architectures ranged from ~HV 83 to 88, in contrast to the original Cu powder microindentation hardness of HV 72 and the commercial Cu base plate hardness of HV 57. These observations illustrate the prospect for creating some form of controlled microstructural architecture by EBM parameter alternation or optimization.

© 2011 Acta Materialia Inc. Published by Elsevier Ltd. All rights reserved.

Keywords: EBM (electron beam melting); SEM (scanning electron microscope); TEM (transmission electron microscope); Equiaxed precipitate; Copper

1. Introduction

It has recently been demonstrated in a Co-base alloy containing 0.2% C, fabricated from precursor powder by additive manufacturing (AM) using electron beam melting (EBM), that the electron beam raster and melt scan parameters create spatial carbide arrays [1]. These arrays are extended into carbide columns as the layers grow. Similar spatial precipitate arrays have also been observed in Inconel 718 (a Ni-base alloy) fabricated by EBM [2], while in a selective laser melting (SLM) study of Ti–6Al–4V alloy,

elongated, textured grain formation was shown to be directly related to the process parameters, including heat input [3]. These observations provide unique if not revolutionary examples of the prospects for controlled microstructural architecture development in material processing. This concept extends the traditional materials science and engineering paradigm of microstructure–property–processing–performance to include microstructural architecture. Although the growth in a controlled manner of columnar grains might be considered a form of microstructural architecture, it represents the spatial and geometrical manipulation of grains or grain structures [1–3]. Dislocation arrays can also be manipulated to form cell structures in metals and alloys whose sizes and cell-wall thickness (or dislocation density in the cell walls) can be manipulated by strain, but these are not true architectures

* Corresponding author at: Department of Metallurgical and Materials Engineering, University of Texas at El Paso, El Paso, TX 79968, USA. Tel.: +1 915 747 5468.

E-mail address: fekkberg@utep.edu (L.E. Murr).

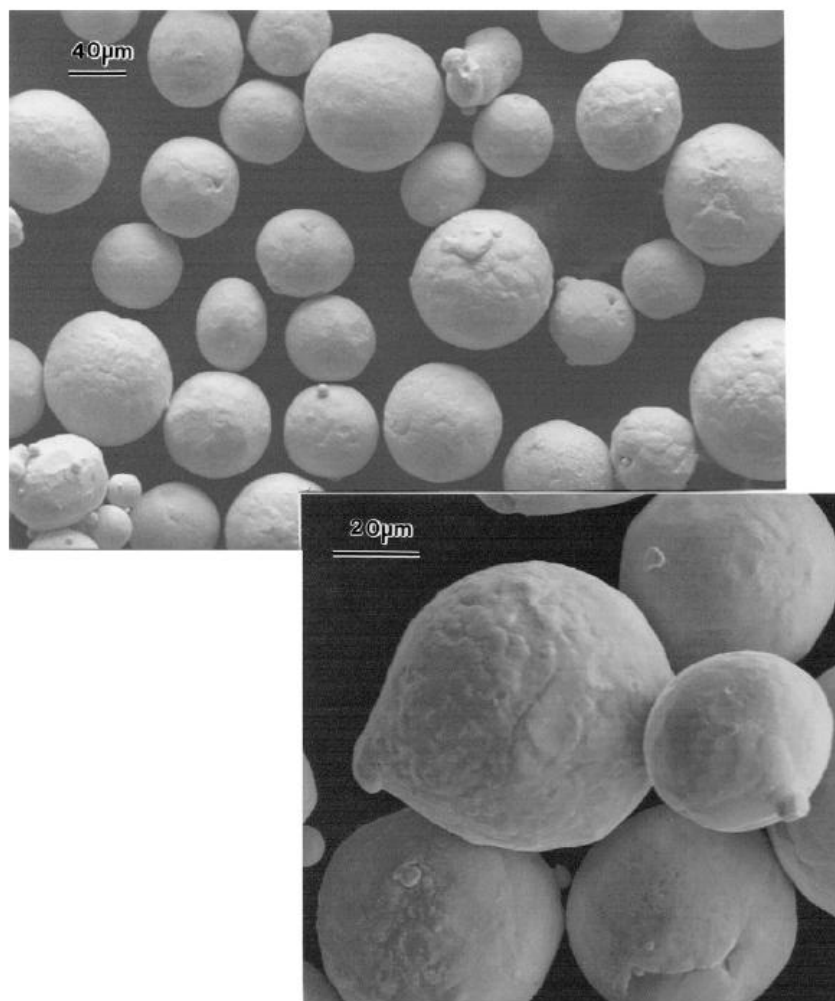


Fig. 1. Precursor copper powder (SEM images). The magnified inset shows particle surface features delineating grains having average diameters of $\sim 6 \mu\text{m}$.

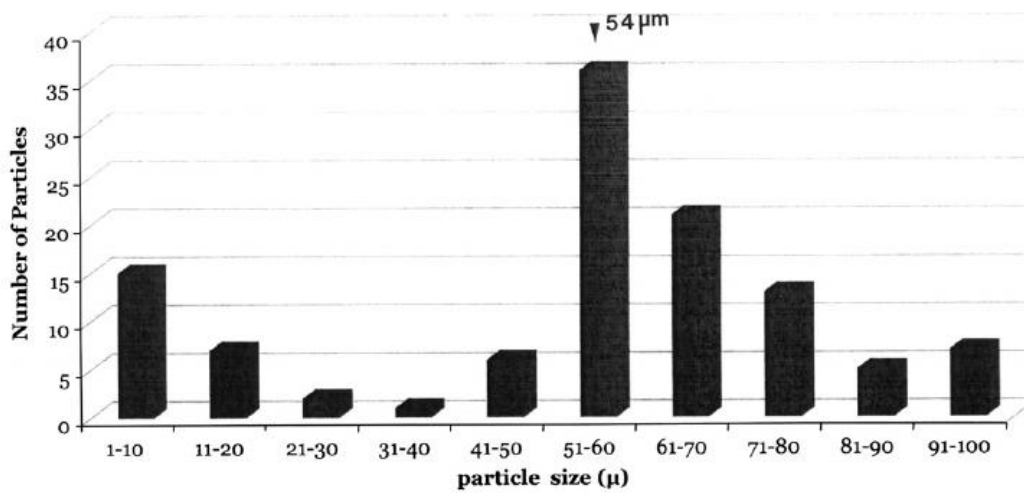


Fig. 2. Precursor copper powder particle size distribution with an average size of 60 μm (arrow).

since they represent only spatial arrays. Varieties of precipitate morphologies and microstructures have also been manipulated by heat treatment or aging in alloy compositions, but these are also not architectures, are confined to the grain matrix in polycrystalline alloys and often vary in geometry as a consequence of the crystal orientation of each grain, or similarly oriented grains.

Precipitates, either coherent or non-coherent, occur as spatial but random arrays which are not manipulated into some semblance of architecture by processing or process variations. The process manipulation of precipitates to form even simple architectures transgressing grain

structures or grain boundaries as illustrated conceptually in Co-base alloy and Ni-base alloy fabrication [1,2] illustrates the prospects for manipulating microstructures to form architectures which can extend the materials science and engineering paradigm alluded to earlier. The challenge in achieving these architectures involves the selection of candidate metals and alloys, and the manipulation or optimization of the process parameters necessary to achieve controlled microstructural architectures which can extend current performance parameters or desirable properties.

In this paper we illustrate the concept of a controlled microstructural architecture in a low-purity, high-

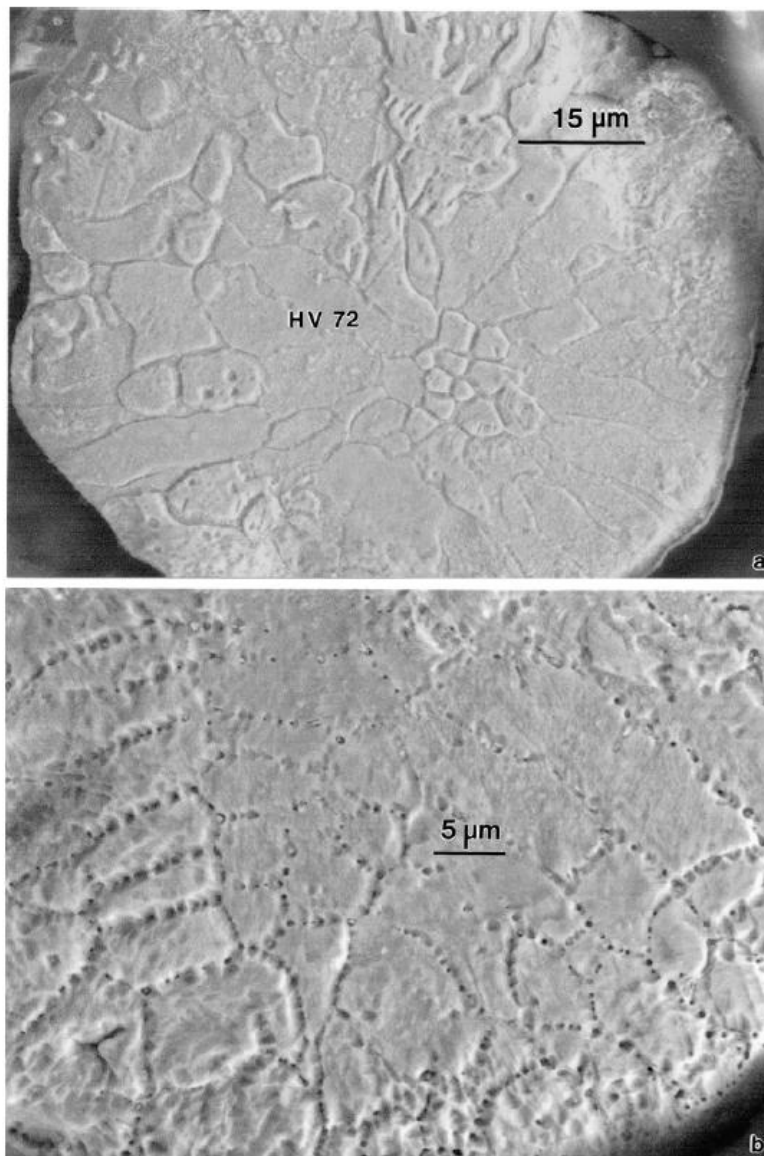


Fig. 3. Precursor copper powder particle internal microstructure for embedded, ground, polished and etched particles. (a) Single-particle observation in the SEM showing grain structures apparent from the surface views of Fig. 1 (inset). (b) Magnified view showing preferential etch/etch pits having regular (cubic-like) geometries within the grain boundaries.

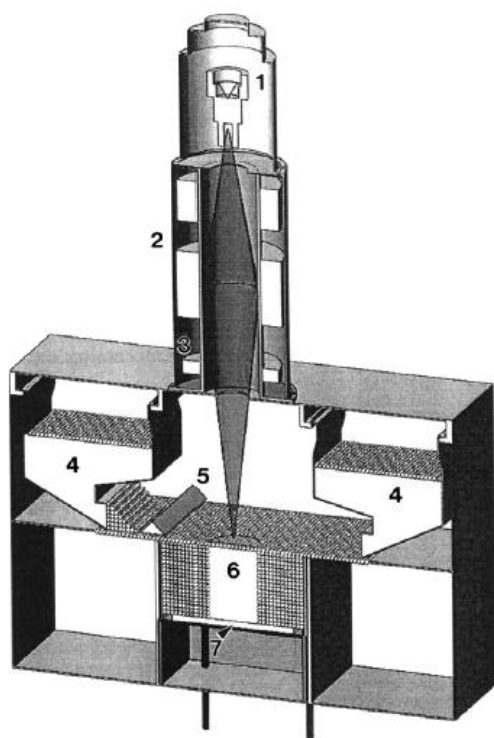


Fig. 4. Arcam A2 EBM system schematic rendering. Numbered components and machine functions are described in the text.

oxygen-containing copper fabricated by EBM. The precursor Cu powder contained a high volume fraction of Cu_2O precipitates, which were retained in the EBM products and distributed in spatial architectures, along with a dense dislocation substructure as a consequence of the powder-layer preheat and melt scan parameters for the electron beam. Here we develop a systematic analysis and characterization of these novel phenomena using optical microscopy and transmission electron microscopy.

2. Experimental details

In this investigation we used an atomized copper powder having a nominal purity of 99.8% Cu. The balance of this composition was primarily oxygen, which formed a high volume of copper oxides (Cu_2O ; cuprite) that segregated to the powder grain boundaries. Cu_2O has a cubic crystal structure, with a lattice parameter of 4.27 Å and space group $PN3M$. Typical Cu powder size and morphology are illustrated in the scanning electron microscope (SEM) image shown in Fig. 1. The particle size distribution consisted primarily of larger particles, ranging from roughly 40 to 100 μm , with smaller, satellite particles attached, as illustrated in Fig. 1. This size distribution is shown in Fig. 2, where the average particle size was 54 μm . Particles were encapsulated in mounting epoxy, which was ground, polished and etched to reveal the interior microstructures

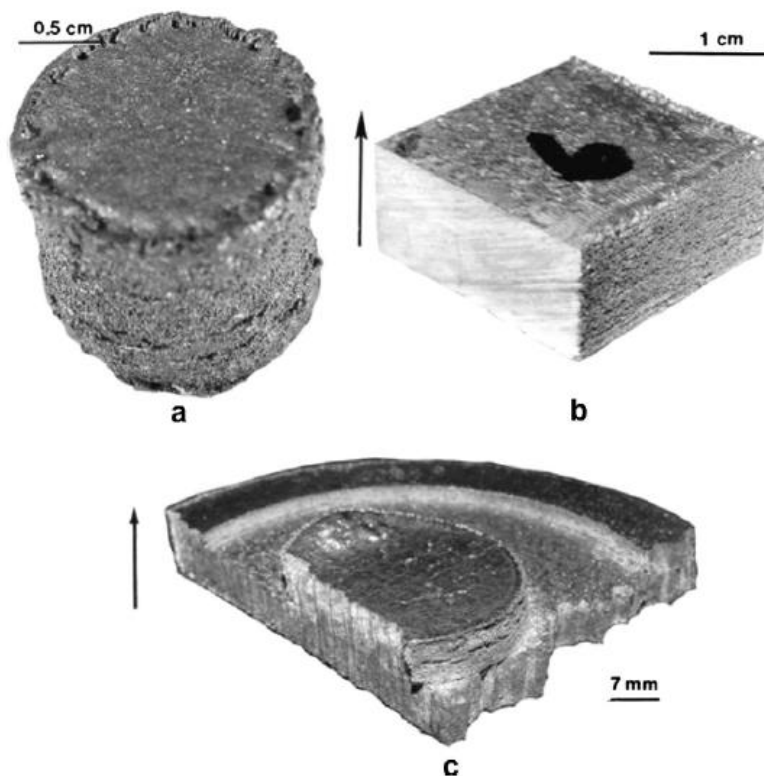


Fig. 5. Examples of components and component (build) geometries fabricated by EBM. (a) Small cylinder, (b) quarter section from 5 cm (25 cm^2) block, (c) structured-geometry prototype product.

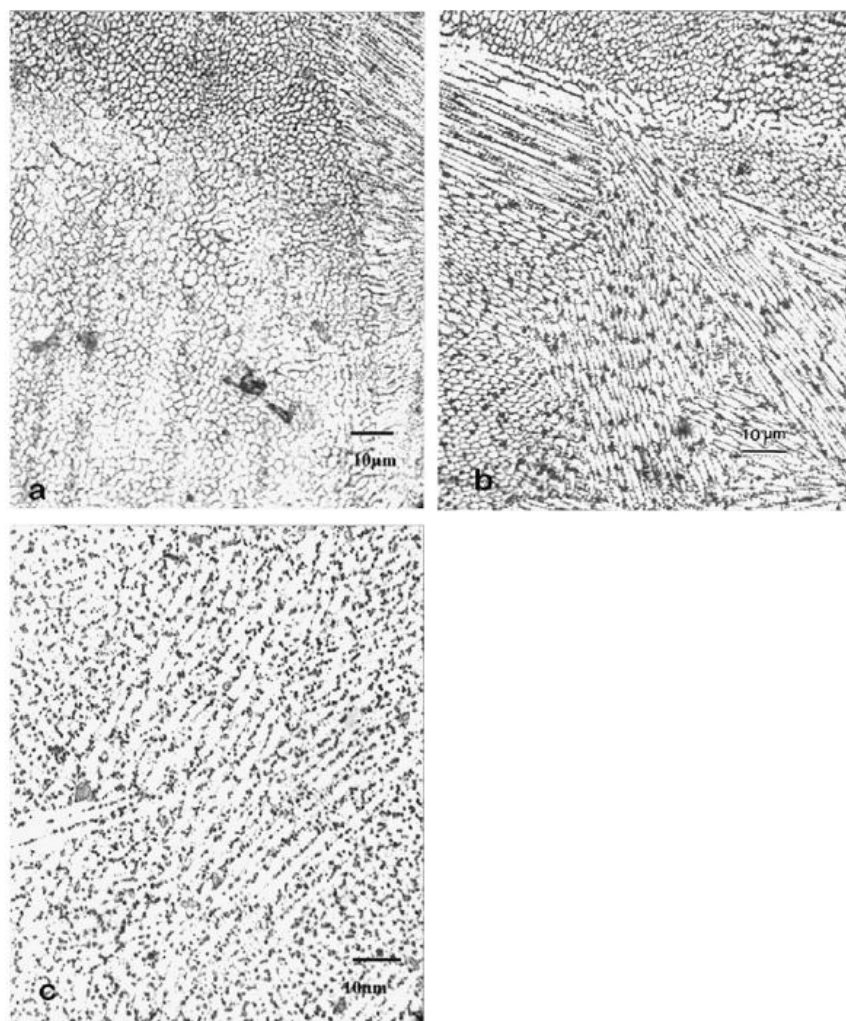


Fig. 6. Optical representation of the microstructure in the horizontal direction for the component in Fig. 5c. Beam offset: (a) 10, (b) 25 and (c) 35, with 35 being the deepest focal length.

of the particles as illustrated in Fig. 3, where the grain size averages $6\text{ }\mu\text{m}$, a relatively small size that gives rise to an instrumental Vickers microindentation hardness of 72, as indicated in Fig. 3a. The magnified view shown in Fig. 3b illustrates the selective etching of precipitates within the grain boundaries forming regular, often square or rectangular, pits.

Fig. 4 shows the Arcam A2 EBM system schematic. In this system the Cu precursor powder (Fig. 1) was contained in cassettes indicated at (4), where it was gravity fed to the build table to be raked (5) into successive layers roughly $100\text{ }\mu\text{m}$ thick. The electron beam is generated in the electron gun (1) at an accelerating voltage of 60 kV, focused by magnetic lenses at (2) and scanned by scan coils at (3) to preheat and selectively melt the powder layer using a computer-aided design (CAD) program. As the component (6) was fabricated, the build table (7) drops down. This table consisted of a commercial copper plate preheated

(with the beam) to $550\text{ }^{\circ}\text{C}$. Powder layers that had been raked and selectively melted were also preheated by scanning the beam (in a vacuum of $\sim 10^{-4}$ torr) at a rate of $\sim 10^4\text{ mm s}^{-1}$ in 10 passes at a beam current of 13.4 mA, while the melt scan followed at a scan rate of 80 mm s^{-1} at a beam current of 10 mA. A pre-melt scan was also employed at a scan rate of $2 \times 10^3\text{ mm s}^{-1}$ with a 30 mA beam current. Each of these beam-scanning steps involved orthogonal beam rastering over the powder bed in the x - and y -directions. The scan domain (the x - y zone) created especially in the melt scans is dependent on the beam focus, which directs maximum energy at varying depths within each powder layer for efficient melting. In this work we varied the so-called beam focus offset using focus numbers which ranged from 10 to 35, with 35 being the deepest focal length. There was no change in scan spacing; however, the change in scan spacing came from the beam focus offset and by varying the beam focus offset, the spacing

increases. These features are similar to the scanning strategies described by Thijs et al. [3] and Verhaeghe et al. [4] for SLM fabrication.

A variety of specimen geometries were fabricated in this study to allow for a range of build parameters to be examined. These included small cylinders and rectangular blocks, as well as other geometry variations. These are illustrated in Fig. 5. Coupons or smaller specimens were extracted from these components (Fig. 5b and c). The extracted test coupons/specimens were cut into sections that were perpendicular or parallel to the build direction. Sections viewed in these orientations were designated horizontal (H) or vertical (V), respectively. These oriented sections were mounted, ground, polished (using a final polish with 0.03 μm alumina) and etched using a solution consisting of 100 ml of water, 8 ml of sulfuric acid, 4 ml of sodium chloride (as a saturated solution) and 2 g of potassium perchlorate. Etching times varied from ~ 2 to 3 s. Etched and rinsed (in H_2O) samples were observed in a Reichert MF4 A/M optical metallograph utilizing a digital image converter. Polished and etched samples were also observed in a Hitachi H-8500 field emission SEM operating at 20 kV in the secondary electron emission mode.

Sections cut from various build geometries (Fig. 5) were also sliced into thin sections using a thin-blade diamond

saw and ground and polished to a thickness of ~ 0.2 mm. Three-millimeter discs were then punched from these thin sections, mechanically dimpled on each side and electropolished to electron transparency in a Tenupol-3 dual-jet electropolishing unit operated at 8 V and a solution temperature of 15 $^{\circ}\text{C}$. The electropolishing solution consisted of 825 ml of water, 375 ml of ethanol, 300 ml of phosphoric acid, 75 ml of propanol and 2.5 g of urea. The electropolished discs were examined in a Hitachi H-9500 transmission electron microscope (TEM), operating at 300 kV accelerating potential, utilizing a goniometer-tilt stage and a CCD digital imaging camera.

The residual Vickers microindentation hardness (HV) of the mounted, polished and etched samples corresponding to the horizontal and vertical reference planes was measured in a Struers Dornamin A-300 digital test station using a 100 gf load, with a dwell time of 10 s.

3. Results and discussion

Fig. 6 illustrates an optical representation of the microstructure in the horizontal direction for the components (Fig. 5c) with beam offsets (focus setting) of (a) 10, (b) 25, and (c) 35, with 35 being the deepest focal length. This feature follows similar processing variations for SLM fabrication [3,4], and illustrates a refinement in microstructure with thermal variations implicit in beam focus variations. Fig. 7 shows a three-dimensional (3-D) image composite

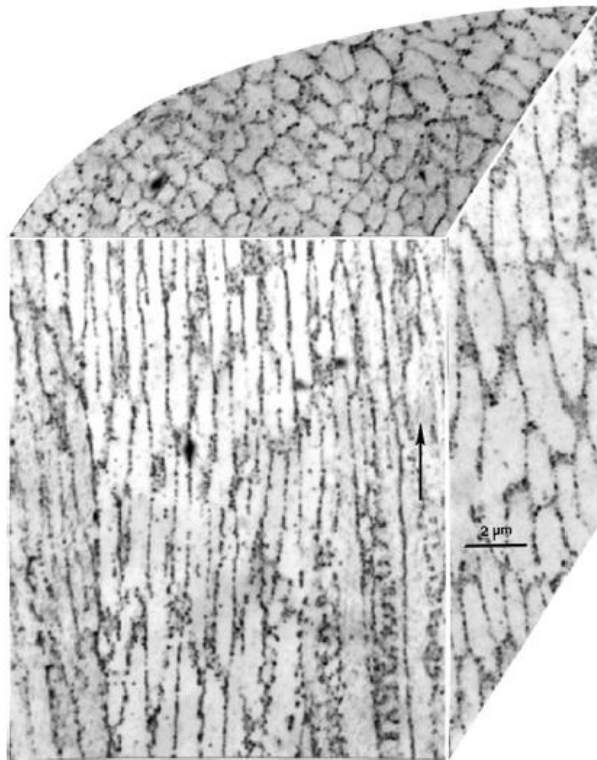


Fig. 7. 3-D image composite representing a typical section of the cylindrical component illustrated in Fig. 5a. Corresponding horizontal and vertical reference-plane microindentation hardness (HV) averages are indicated. The arrow indicates the layer building direction.

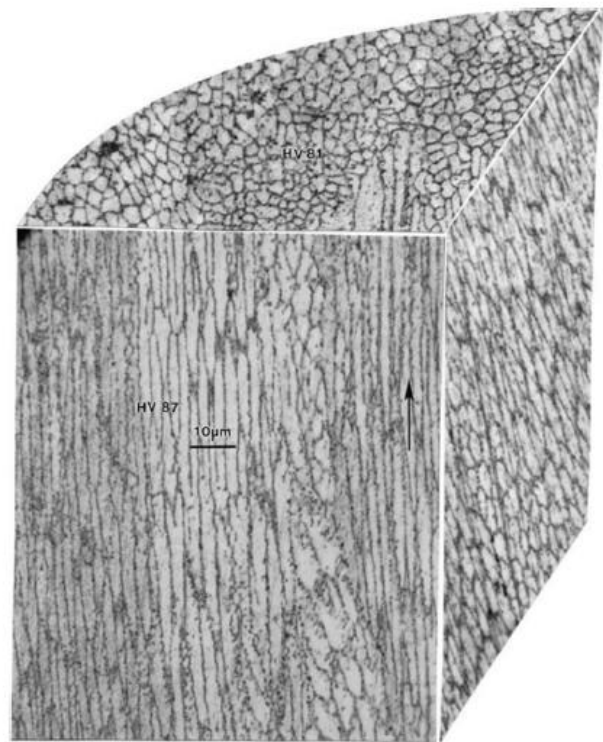


Fig. 8. Magnified 3-D image composite as in Fig. 7.

representing a cylindrical section from Fig. 5a which illustrates small, equiaxed cell or domain structures in the horizontal plane (perpendicular to the build direction shown by the arrow at the right) and connected (or corresponding) elongated structures or structure variations in the vertical plane parallel to the build direction. These domains are considerably smaller than the equiaxed grain structure typical of the precursor powder illustrated in Fig. 3, and account in part for the considerable hardness increase in both the horizontal and vertical planes, as indicated in Fig. 7. In addition, while the average (horizontal and vertical planes) microindentation hardness is \sim HV 83 and a 15% increase over the precursor powder in Fig. 3), there is a 7% difference between the softer horizontal plane and the vertical plane.

Fig. 8 shows a magnified view of a 3-D image composite section as in Fig. 7, illustrating irregular etching features

(etch pits) delineating cellular-like structures, while Fig. 9 shows these etch-pit features to be regular cubic or rectangular pits similar to those etched in the grain boundaries in the precursor powder in Fig. 3. These features are more specifically delineated in the TEM images provided in Figs. 10 and 11. In Fig. 10 a corresponding horizontal plane optical metallograph image inset shows the cell/domain spatial reference for the TEM image which shows a unique precipitate/dislocation-like cell structure. Non-coherent (Cu_2O) precipitates attached to dislocations (possibly generated at the precipitate/matrix interface) form these spatial arrays, which are selectively etched and form pits in the optical microscope and SEM images (Figs. 8 and 9). The cell or domain centers contain a high density of dislocation/vacancy loops, as illustrated at the arrow near the top of Fig. 10. Fig. 11 shows these features magnified, including the vacancy dislocation loops (arrow bottom

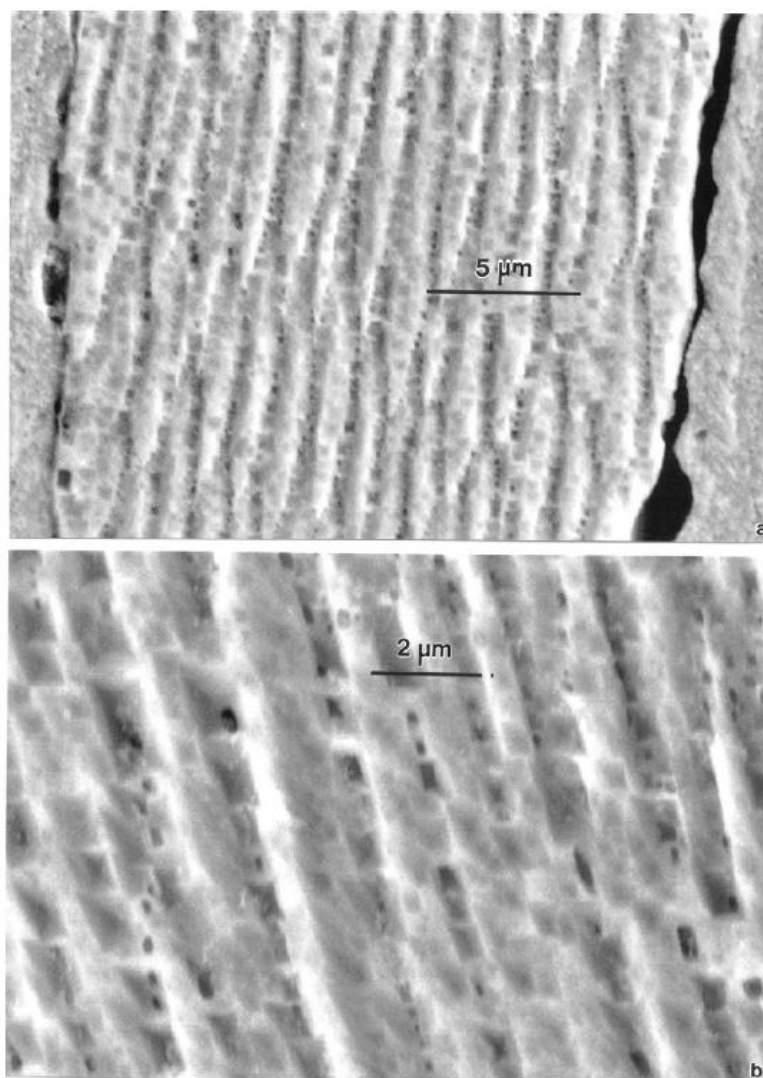


Fig. 9. SEM views of regular, cubic/rectangular etch pits corresponding to the elongated cell-like structures in Fig. 7. (a) Vertical reference plane structures matching those in Fig. 7. (b) Magnified view showing the etch-pit geometry.

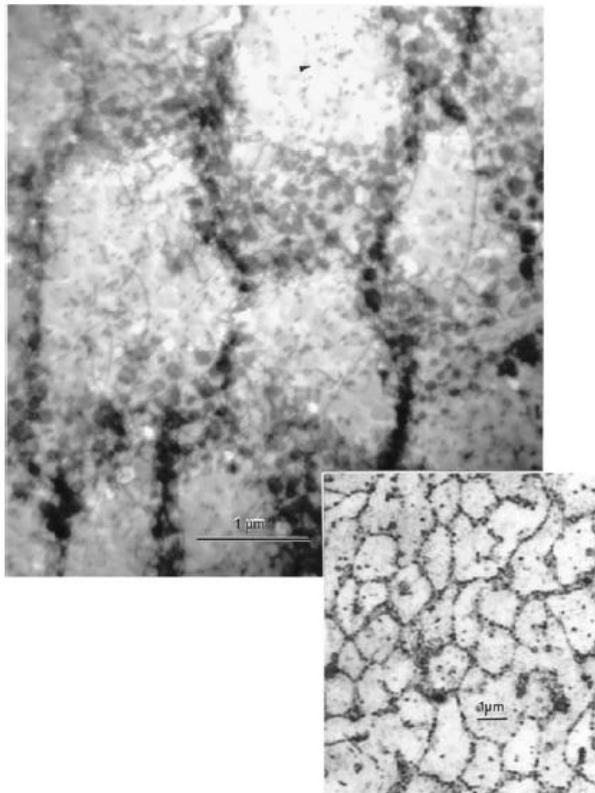


Fig. 10. TEM bright-field image showing precipitate-dislocation arrays corresponding to the horizontal reference plane (Fig. 8), as illustrated in the optical metallographic image shown in the inset.

right). It can be noted in Fig. 11 that selective precipitates have been variously etched out (white areas) and some exhibit the cubic or cube-related geometry illustrated in the etch pits of Fig. 9. The etching shown in Fig. 9b suggests that these precipitate particles have a relatively common orientation, and this is confirmed on examining the precipitate morphologies and their geometric or crystallographic coincidence in the (1 1 0) grain surface orientation, as represented in the selected-area electron diffraction (SAED) pattern inset in Fig. 11. The operating reflection, g , in the Fig. 11 inset indicates the $[\bar{1}10]$ trace direction, which many precipitates appear to be associated with along one edge.

Fig. 12 illustrates the precipitate-dislocation (microstructural) architecture features in the vertical plane reference, showing elongated cell-like precipitate/dislocation arrays that are exaggerated by precipitate etching along or close to the build direction. These are closely associated with Fig. 9b, and effectively the same as shown in Figs. 10 and 11. It should be noted that the H_2SO_4 in the surface etch (Fig. 9b) is more aggressive than the phosphoric acid etching in the TEM sample preparation. Consequently, only the precipitates or volumes near them create etch pits.

This unique microstructural architecture, especially in the context provided in the observations of Figs. 7–12,

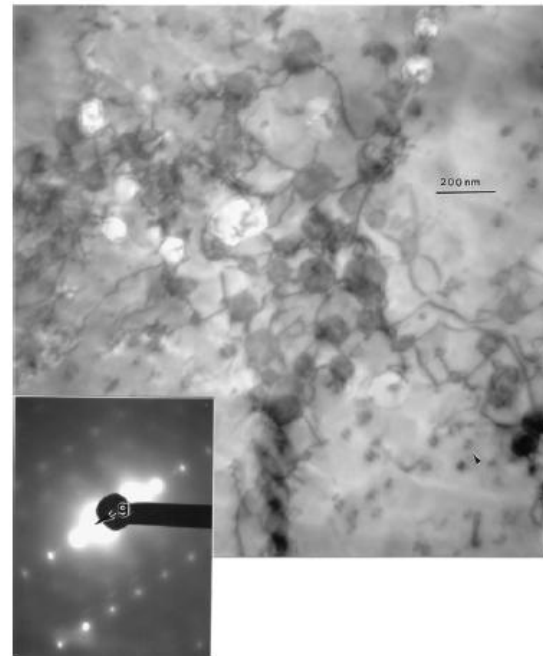


Fig. 11. Magnified TEM bright-field image showing the horizontal reference plane precipitate-dislocation array microstructure (as in Fig. 10). The inset SAED pattern is a $[1\ 1\ 0]$ zone axis with $g = [\bar{1}11]$. The arrow (lower right) shows typical dislocation loops.

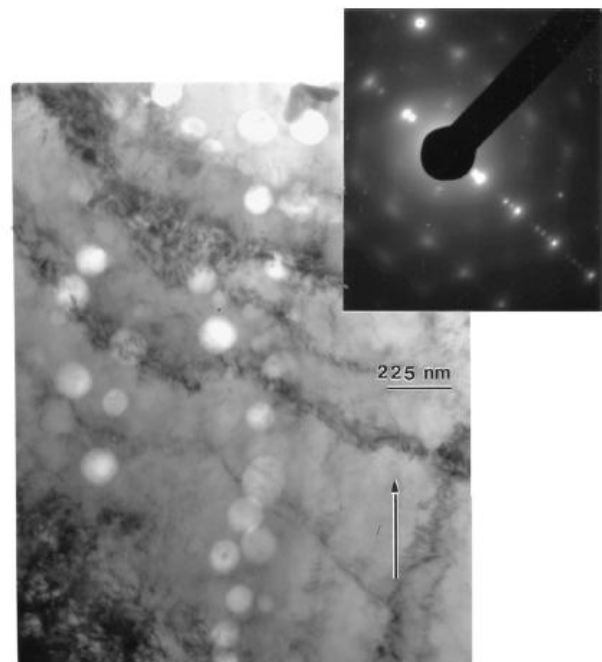


Fig. 12. TEM bright-field image showing precipitate-dislocation architecture features in the vertical reference plane (Fig. 7). Especially prominent is the linear, selective etching at the precipitates. The inset SAED pattern shows the Cu_2O precipitate diffraction spots.

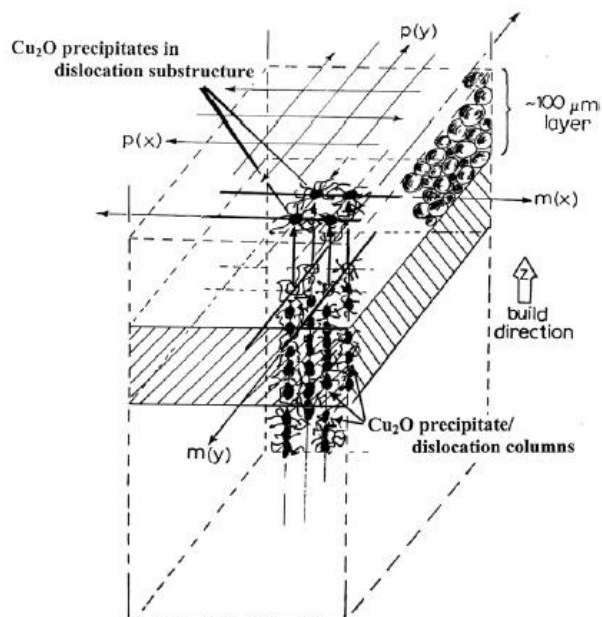


Fig. 13. EBM scan geometry ideally forming precipitate-dislocation architectures in fabricated Cu components (Fig. 5). Preheat scans are marked $p(x)$ and $p(y)$, while the corresponding melt scans are denoted $m(x)$ and $m(y)$.

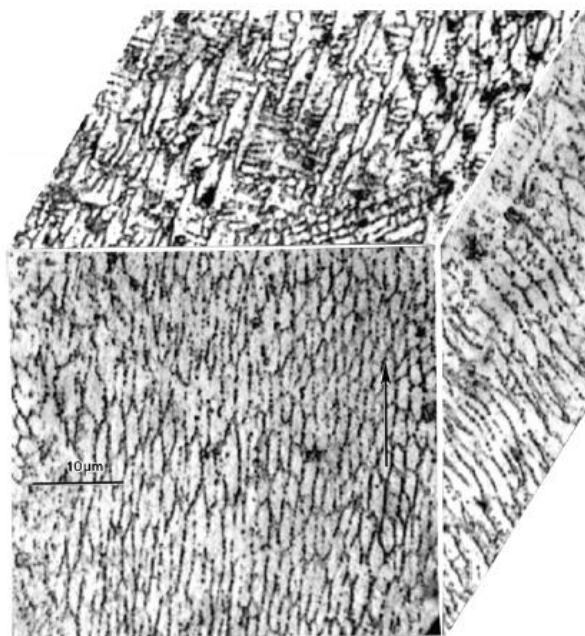


Fig. 15. The 3-D image composite in Fig. 14 under higher magnification.

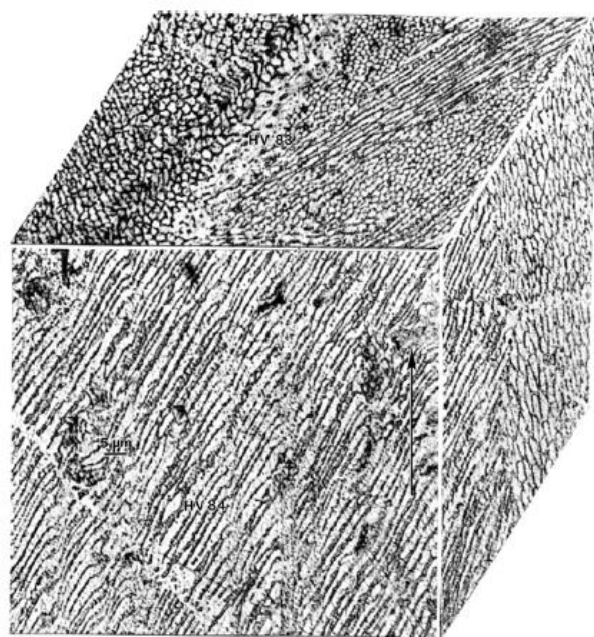


Fig. 14. 3-D optical microscope image composite section typical of the extracted rectangular block specimens represented in Fig. 5b.

appears to be the result of either reprecipitation in the preheat and melt scans or the rearrangement of the precipitates during the melt scan, or both. The spatial precipitate-dislocation arrays observed in the horizontal plane

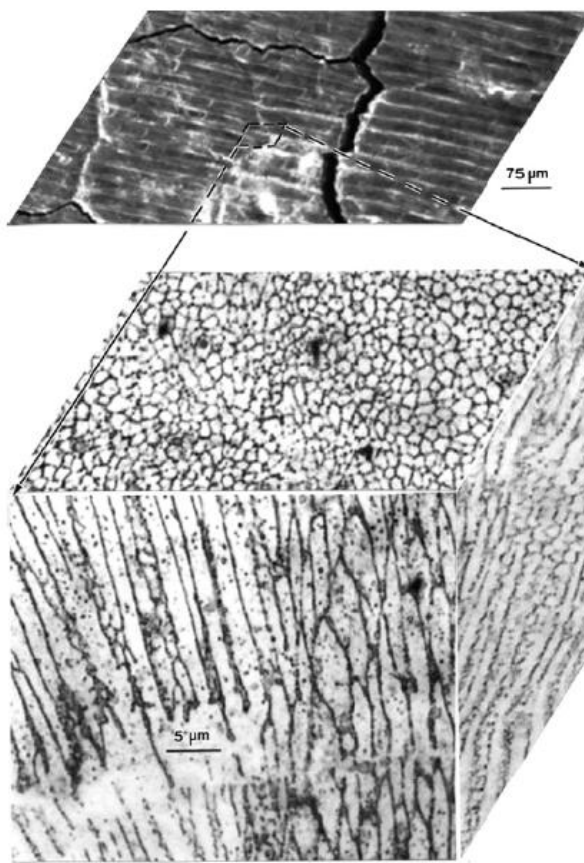


Fig. 16. Spatial composite showing a typical horizontal reference plane section in an intergranular-like domain along with 3-D image composite for the EBM component illustrated in Fig. 5c.

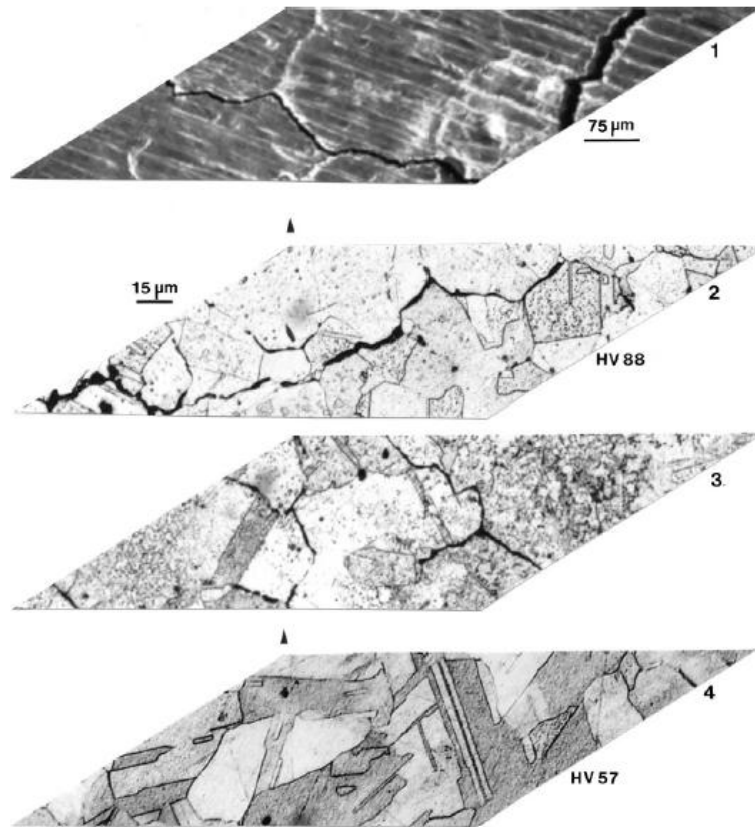


Fig. 17. Spatial array illustrating the surface structure of the EBM component (1) in Figs. 5c and 16 in relation to the upper base plate microstructure/grain structure (2 and 3) and the bottom of the plate (4). Corresponding microindentation hardness averages (HV) are also indicated.

and illustrated in Figs. 7–12 appear to be related to, and controlled by, the preheat and melt scan parameters, especially the change in direction (x, y). This scan geometry creates thermokinetic zones whose spatial features are particularly dependent on the EBM-scan dimensions or spacing. Fig. 13 illustrates these features schematically in creating the microstructural architectures. As these electron beam parameters are altered, the regularity of the architectures can vary as well. Similar features have been discussed for the SLM fabrication of Ti–6Al–4V components by Thijs et al. [3], who describe the parameter variations, etc. in the context of beam-scanning strategies, while similar precipitate architectures have also been described for an Ni-base alloy fabricated by EMB [2].

On examining the rectangular EBM-fabricated test blocks, irregular architectures can be seen to occur (Fig. 5b), as represented in the 3-D optical microscope image composites for a test block section (as shown in Fig. 5b) corresponding to a more energetic melt scan, with a different beam focus from that in the initial cylindrical sample illustrated in Fig. 5a (see Fig. 6). A typical example of this feature is represented in Figs. 14 and 15 for a section from Fig. 5b where the architecture varies in both the horizontal and vertical reference planes in contrast to Figs. 7

and 8. The Vickers microindentation hardness shown in Figs. 14 and 15 is essentially the same, on average, as that shown in Fig. 8, although there is less variance between the horizontal and vertical reference planes. Figs. 14 and 15 highlight these microstructural architecture variations in comparison with Fig. 8.

Fig. 5c, corresponding to an electron beam focus offset of 35, particularly illustrates considerable embrittlement, as evidenced by the features which resemble a large intergranular fracture. These features are illustrated in Fig. 16, which shows a failed section from Fig. 5c. The large, intergranular fracture features are apparent in the upper view of Fig. 16, while the 3-D image composite represented in the lower part of the figure is similar in most respects to Figs. 7 and 14. The large, column-like grains evident in Figs. 16 and 5c seem to grow in two column sections roughly 0.8 cm in height (Fig. 5c) and suggest some degree of epitaxial growth from the copper base plate (Figs. 4–17)). In order to investigate this feature, a base plate specimen was cut and mounted to allow images to be obtained from the back of the plate, and from selective sections near the build or build interface. Fig. 17 illustrates these section views from 1 to 4, with 4 being the back of the base plate furthest from the build. Fig. 17(1) represents



Fig. 18. Typical grain and sub-grain spatial precipitate-dislocation arrays in the horizontal reference plane corresponding to Figs. 16 and 17. Note the irregular grain boundaries.

the top of the build and exhibits an intergranular-like fracture similar to Fig. 16, while Fig. 17(2) and (3) shows upper base plate sections at and just below (~ 1 mm) the build base. While the grain structure is not significantly changed from the base plate bottom (Fig. 17(4)), there is clear evidence of oxygen or oxide precipitate segregation at the grains and grain boundaries, especially the high-angle or high-energy grain boundary portions. In this respect, note in Fig. 17(2) and (3) that there is no cracking along the straight-appearing, coherent twin boundaries, which in copper have an interfacial free energy significantly less than the nominal grain boundary free energy: roughly 75 vs. 750 mJ mm^{-2} [5]. It should also be noted in Fig. 16 that the hardness between the base plate bottom (HV 57) and the top (HV 88) increases by 53%. The base plate bottom hardness is also 26% softer than the precursor powder (HV 57 vs. HV 72, respectively). This illustrates the precipitation-related hardening effect also observed in the EBM products (Fig. 5).

While there does not appear to be any clear evidence for epitaxial growth for the build (as described for elongated grains in the SLM fabrication of Ti–6Al–4V [3]), the rich oxygen content of the build appears to influence the upper

build grain structure significantly. Interestingly, the apparent large, columnar grains suggested in Figs. 16, 17 and 5c are not single-crystal regimes but, rather, irregular, polycrystalline arrangements with average grain sizes of $\sim 60 \mu\text{m}$, consistent with the starting (or precursor) powder diameter (Fig. 2) and larger than the base plate grain size (Fig. 17(2)–(4)) of $\sim 15 \mu\text{m}$. This feature is shown in Fig. 18, which represents a section view of Fig. 17(1). Note that the magnified horizontal plane section views of Figs. 7, 8 and 14–16 correspond to a grain interior region in Fig. 18. The grain structures and grain sizes implicit in Fig. 18 were also confirmed by X-ray diffraction in both the horizontal and vertical reference planes.

Whereas high concentrations of oxygen and especially copper oxide precipitates in copper are normally detrimental and generally avoided in high-purity Cu, this investigation suggests prospects for revolutionary developments in precipitation-hardenable or precipitation-rich metals and alloys. By adjusting or optimizing the process parameters, these features may lead to controlled microstructural architectures with novel properties and performance features. This has been demonstrated previously for carbide architectures in a Co-base alloy and columnar precipitates in a

Ni-base alloy [1,2], and is confirmed by the observations presented in this paper.

4. Summary and conclusions

A relatively impure (98.5%) Cu (atomized) precursor powder containing a high concentration of Cu₂O (cuprite) precipitates has been observed to form unique and unusual precipitate–dislocation architectures (or regular, spatial arrays) in a variety of component geometries fabricated by AM using EBM. These spatial arrays occur within regular grain structures and demonstrate the prospect of precipitate–dislocation (microstructural) architecture control for achieving novel property–performance extensions using a select, optimized process (EBM) to extend the many decade materials science and engineering paradigm involving the connectivity of material structure–properties–processing–performance. The precipitate–dislocation architecture observed in EBM-fabricated products has very similar spatial and geometrical arrays to the columnar carbide arrays created in a Co-base, carbon-containing alloy by EBM: cell-like, equiaxed arrays in the horizontal reference plane perpendicular to the build direction having dimensions ranging from ~1 to 3 μm. These precipitate–dislocation architectures create increased hardness in EBM-fabricated

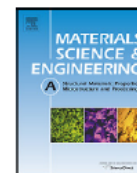
Cu, ranging from a base-plate hardness of HV 57 to an EBM product hardness of HV 88, referenced to the precursor powder containing Cu₂O precipitates that has a hardness of HV 72. This corresponds to a hardness extension of 54%.

Acknowledgments

This research was supported by the Airforce Research Laboratory through Clarkson Aerospace Contract #UTEP – 10-5567-013-02-C2 (Task Order 2.10.2). Copper EBM fabrication was also partially supported by the US Department of Energy SBIR Grant DE-SC0000867.

References

- [1] Gaytan SA, Murr LE, Martinez E, Martinez JL, Machado BI, Ramirez DA, et al. *Metall Mater Trans A* 2010;41:3216–27.
- [2] Strondl A, Fischer R, Fronmeyer G, Schneider A. *Mater Sci Eng A* 2008;480:138–47.
- [3] Thijs L, Verhaeghe F, Craeghs T, Hambeeck JV, Kruth J-P. *Acta Mater* 2010;58:3303–12.
- [4] Verhaeghe F, Craeghs T, Heulens J, Pondelaers L. *Acta Mater* 2009;57(20):6006–12.
- [5] Murr LE. *Interfacial phenomena in metals and alloys*. Reading, MA: Addison Wesley Publishers; 1975.



Open-cellular copper structures fabricated by additive manufacturing using electron beam melting

D.A. Ramirez^{a,b,*}, L.E. Murr^{a,b}, S.J. Li^c, Y.X. Tian^c, E. Martinez^{a,b}, J.L. Martinez^{a,b}, B.I. Machado^a, S.M. Gaytan^{a,b}, F. Medina^b, R.B. Wicker^{b,d}

^a Department of Metallurgical and Materials Engineering, The University of Texas at El Paso, El Paso, TX 79968, USA

^b W. M. Keck Center for 3D Innovation, The University of Texas at El Paso, El Paso, TX 79968, USA

^c Shenyang National Laboratory for Materials Science, Institute of Metal Research, Chinese Academy of Sciences, 72 Wenhua Road, Shenyang 11016, China

^d Department of Mechanical Engineering, The University of Texas at El Paso, El Paso, TX 79968, USA

ARTICLE INFO

Article history:

Received 29 September 2010

Received in revised form 9 February 2011

Accepted 11 March 2011

Available online 21 March 2011

Keywords:

Additive manufacturing

Electron beam melting

Precipitates

ABSTRACT

Cu reticulated mesh and stochastic open cellular foams were fabricated by additive manufacturing using electron beam melting. Fabricated densities ranged from 0.73 g/cm³ to 6.67 g/cm³. The precursor Cu powder contained Cu₂O precipitates and the fabricated components contained arrays of Cu₂O precipitates and interconnected dislocation microstructures having average spacings of ~2 μm, which provide hardness values ~75% above commercial Cu products. Plots of stiffness (Young's modulus) versus density and relative stiffness versus relative density were in very close agreement with the Gibson–Ashby model for open cellular foams. These open cellular structure components exhibit considerable potential for novel, complex, multi-functional electrical and thermal management systems, especially complex, monolithic heat exchange devices.

© 2011 Elsevier B.V. All rights reserved.

1. Introduction

Two common types of open-cellular structures include reticulated (grid-like or network) mesh structures and stochastic (or random) foam structures. Key physical features of these open-cellular mesh and foam structures include strut or ligament (cross-section) dimensions, surface area (specific surface area: m²/g), low porosity and relative density, high thermal conductivity and strain isolation (and buffer) between structures (including so-called stress shielding in metal or next generation biomedical implants [1]), and often attractive specific strength. Metal foams in particular have been manufactured for many years by metallic sintering of powder, metal deposition by physical or chemical vapor (PVD or CVD respectively; including electron beam-directed vapor deposition), investment casting, and other novel techniques. The most common metal foams over the past several decades have been aluminum or aluminum alloys manufactured by liquid or semi-liquid foaming technologies [2]. These foams have provided light-weight supporting structures in aerospace applications as well as heat exchanger applications where their compact, light weight, open cellular structures provide efficient heat transfer [3,4].

Heat transfer by conduction involves energy transfer without any material motion, and the rate of heat transfer is dependent upon the temperature gradient as well as the thermal conductivity of the material. At some specific temperature, the thermal and electrical conductivities of metals are proportional. Raising the temperature however increases the thermal conductivity while decreasing the electrical conductivity. Correspondingly, metals with high electrical conductivity would represent high thermal conductivity at a given temperature. Consequently, copper becomes an obvious candidate for mesh or foam structure applications for a variety of thermal management systems, including of course electronic thermal management applications. Contemporary metal foam manufacturers have fabricated open cellular copper foams by a variety of powder metallurgy techniques for these purposes [5].

In the case of actively cooled vehicle skin structures, particularly open-cellular metal core sandwich panel wingskins for aeronautic or aerospace applications, copper is especially unique because of its high thermal conductivity and reasonable specific strength. The development and fabrication of mesh and foam structures with densities one-tenth that of bulk copper therefore make these concepts attractive not only for wingskin applications but a host of other multifunctional truss or ligament structures. However, unlike aluminum and aluminum alloys [2,6] there is no similar data comparing copper mesh or foam structure stiffness or specific strength with density or relative density and other properties [7,8]. For aluminum and its alloys, plots of relative stiffness (or modulus) versus

* Corresponding author at: Department of Metallurgical and Materials Engineering, The University of Texas at El Paso, El Paso, TX 79968, USA. Fax: +1 91574748002. E-mail address: daramirez2@miners.utep.edu (D.A. Ramirez).

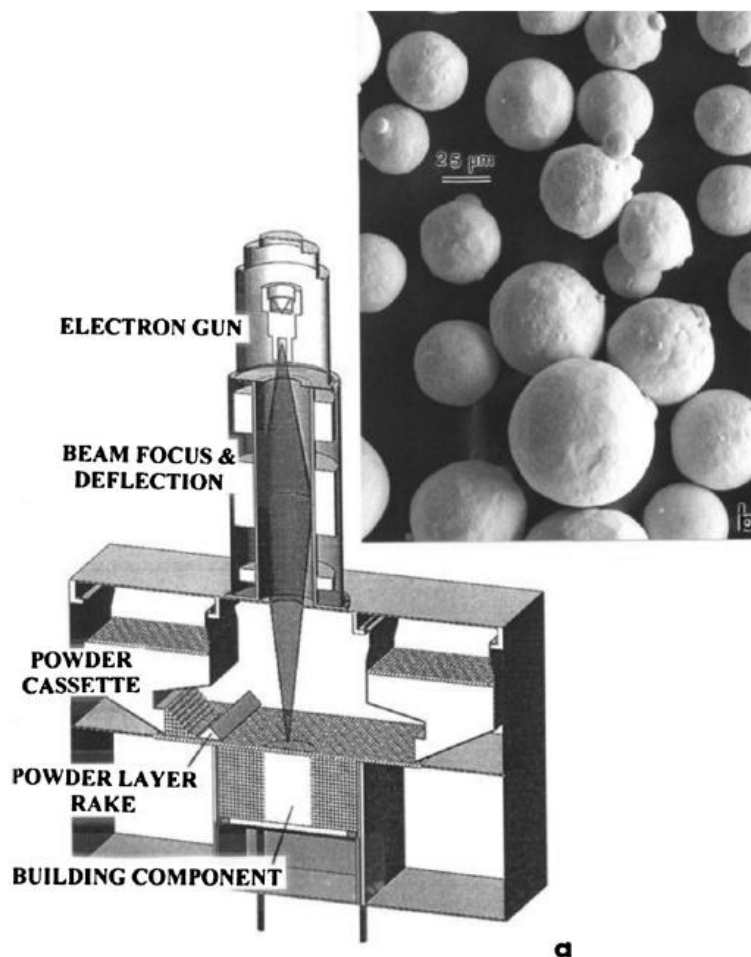


Fig. 1. Arcam A2 EBM facility (a) and Cu precursor powder (b). The Cu powder (b) is gravity fed from cassettes and raked into a layer $\sim 100 \mu\text{m}$ where the focused electron beam rasters to pre-heat the layer and finally melt prescribed areas.

relative density are characterized by the Gibson–Ashby model for open cellular foams [6]:

$$\frac{E}{E_0} = \left(\frac{\rho}{\rho_0} \right)^n, \quad (1)$$

where E and E_0 are the Young's modulus for specific, open-cellular materials with density ρ , and the fully dense, bulk material (E_0) with a density of ρ_0 . Values of n for Al and Al-alloys vary from ~ 1.8 to 2.2 , but $n \cong 2$ generally applies to a wide range of aluminum and aluminum alloy data [2,6]. Murr et al. [1,9] have also recently demonstrated that both regular, reticulated mesh structures as well as open cellular foam structures of Ti–6Al–4V follow a similar log–log plot, with $n \cong 2.4$. Ti–6Al–4V is also a prominent aerospace material with a density of 4.43 g/cm^3 in contrast to Al where $\rho_0 = 2.7 \text{ g/cm}^3$. Correspondingly, open-cellular and multi-functional structures fabricated from Ti–6Al–4V have specific advantages over aluminum and its alloys.

While open cellular Cu foams have been commercially available for at least a decade using sintered Cu powder as a precursor to produce lace microstructures or other open microstructures [5], there are no examples of complex Cu open-cellular structures fabricated as multi-functional monoliths. In this research paper, we

describe the systematic fabrication of various Cu open cellular mesh and foam structures from a powder precursor by layer or additive manufacturing (AM) using electron beam melting (EBM). In addition, we have characterized these components using optical and electron microscopy (both scanning and transmission electron microscopy: SEM and TEM, respectively) along with measurements of the dynamic Young's modulus or stiffness as a function of density.

2. Experimental methods/procedures

Fig. 1(a) illustrates the basic AM-EBM system while Fig. 1(b) shows the Cu precursor powder with an average particle diameter of $\sim 65 \mu\text{m}$. This powder, with a purity of 99.8%, contained Cu_2O precipitates and residual oxygen as a consequence of the atomization production process. The EBM system (Fig. 1(a)) was an Arcam A2 which builds monolithic structures layer-by-layer using computer-aided design (CAD) software/models to melt specific, spatial arrays in each layer – raked from gravity fed powder cassettes. This is achieved by scanning the focused electron beam in multiple pre-heat scans prior to the melt scan [2]. In this research program we used materialize/magic Materialise/Magic® software

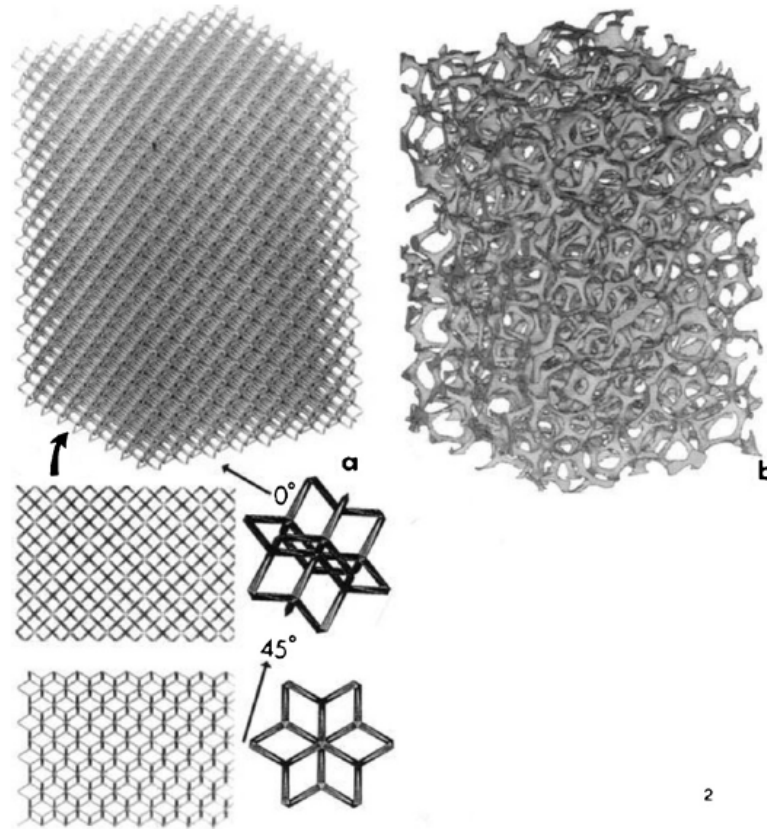


Fig. 2. Software (CAD) model renderings of Materialize dodec-thin mesh build (a) and open cellular foam model (b). The unit and extended cell views for (a) are at 45° from (0) to (45°) normal to the face (0) and along a diagonal (edge) (45°).

to create reticulated mesh structures based on geometry elements or a build lattice unit cell which can be dimensionally scaled to produce density or porosity variation. Computed-tomography (CT) scans of commercial, open-cellular aluminum alloy foams created a stochastic open-cellular foam build unit which was geometrically scaled to create monolithic density or porosity variations [1]. Fig. 2 compares 3D-CAD models characteristic of these open-cellular mesh and foam structures. In this study we built reticulated mesh structures ranging in density from 1.20 to 6.67 g/cm³; including a virtually solid component having a density of 8.02 g/cm³ (in contrast to fully dense Cu having an ideal density of 8.9 g/cm³). Stochastic foams modeled from Fig. 2(b) ranged in density from 0.73 to 1.70 g/cm³.

The elastic moduli (E) (or Young's moduli), also referred to as a stiffness-related number, for the fabricated open-cellular structures were measured using a resonant frequency analyzer RFDHTVP1750-C. This system measures the resonant frequency in the specimen arising from a mechanically induced vibration where the stiffness (E) is given generally by

$$E = \xi m f_r^2 \quad (2)$$

where ξ is a geometrical, specimen shape factor (generally constant for these measurements), m is the sample mass and f_r is the measured, resonant frequency. Ideally, this non-destructive testing measures the dynamic stiffness in contrast to the static stiffness for more conventional, destructive, tensile or compression testing. The sample design for open cellular structures fabricated in this study (Fig. 2) followed the general metal foam requirements described

by Ashby et al. [2]: height/width > 1.5, height > 7 times the cell size, pore size, or open channel size. Specimen sizes were either fabricated to 2.3 cm × 2.3 cm × 3.6 cm, or carefully machined to size for oversize specimens.

Following stiffness measurements, selective or representative fabricated test structures were sliced into sections which were mounted, polished, and etched for optical metallographic examination in a Reichart MF4 A/M metallography unit. The etchant consisted of a solution composed of 100 mL water, 8 mL sulfuric acid, 4 mL saturated sodium chloride solution, and 2 g potassium perchlorate. The polished and etched specimens as well as unmounted specimen sections were also examined in a Hitachi S-8500 field-emission scanning electron microscope (SEM) operating at 20 kV in the secondary electron emission mode. Vickers microindentation hardness (HV) measurements were also made on the mounted samples using a Shimadzu HMV-2000 diamond indenter test station employing a 25 g (0.245 N) load applied for ~10 s.

Finally, sections sliced from the most dense specimens (8.02 g/cm³) using a thin-blade diamond saw were ground and polished to a thickness of ~200 μm, and 3 mm discs were punched from these thin sections, mechanically dimpled on both sides, and electropolished to electron transparency using a Tenupol-3, dual-jet electropolishing unit. The electropolishing solution consisted of 825 mL water, 375 mL ethanol, 300 mL phosphoric acid, 75 mL propanol, and 2.5 g of urea. The electropolished discs were examined in a Hitachi H-9500 transmission electron microscopy (TEM) operated at 300 kV, utilizing a goniometer-tilt stage and a CCD digital imaging camera.

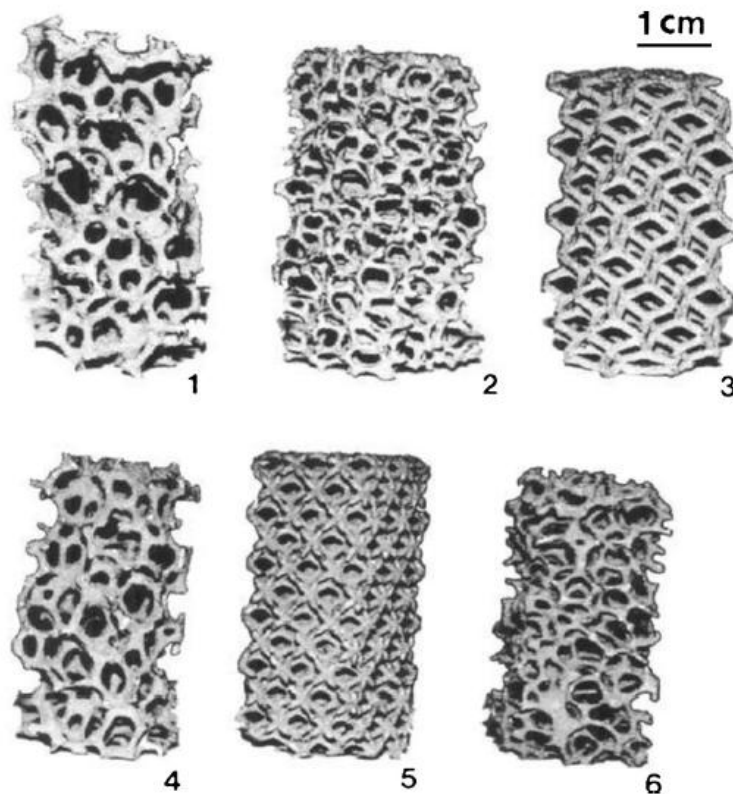


Fig. 3. Examples of open cellular Cu mesh and foam specimens fabricated from CAD models in Fig. 2 by EBM (Fig. 1). The corresponding densities, ρ , and pore densities in pores/inch [ppi], are as follows: (1) 0.84 g/cm^3 [4 ppi]; (2) 0.73 g/cm^3 [6 ppi]; (3) 1.20 g/cm^3 [3 ppi]; (4) 1.28 g/cm^3 [3 ppi]; (5) 1.69 g/cm^3 [5 ppi]; (6) 0.93 g/cm^3 [6 ppi]. Stochastic foams are shown in (1), (2), (4) and (6); reticulated mesh samples are shown in (3) and (5).

3. Results and discussion

Figs. 3–5 illustrate the range of open cellular mesh and foam structures having a range of densities noted. These structures correspond to four different articulated mesh arrays. The most dense mesh array is illustrated in Fig. 5(c) along with a more dense solid section having a density of 8.02 g/cm^3 . While these components contained some porosity as a consequence of unconsolidated or unmelted regions, the Cu_2O precipitates also contributed to a reduced density. The approximate volume fraction of Cu_2O precipitates estimated from a comparison of X-ray diffractometer spectral peaks was estimated to be $\sim 2\%$. The corresponding foam arrays had a range of densities from 0.73 to 1.70 g/cm^3 . The anisotropic strut structures for the reticulated mesh samples along with ligament structures for the isotropic stochastic foam samples are shown for comparison in Fig. 4, corresponding to reference planes of 90° (sample face views) and 45° (sample edge or diagonal views).

Fig. 6 compares optical metallographic views of the mesh strut and foam ligament microstructures, corresponding to the mesh and foam samples illustrated in Fig. 5(a) and (b), respectively. Note the Cu_2O microstructural arrays in the horizontal plane views having an average spacing of $2 \mu\text{m}$ perpendicular to the build direction in contrast to the same Cu_2O precipitate microstructures in the build direction indicated by the arrow in Fig. 6. These Cu_2O precipitate arrays in a horizontal plane perpendicular to the build direction are also observed in the solid (8.02 g/cm^3) sample shown in Fig. 5(d) from which TEM sections could be extracted and electron transparent discs prepared. Ramirez, et al. [10] have discussed the details of the precipitation features of EBM fabrication of Cu components in prior work.

Fig. 7 shows a bright-field TEM image for precipitate arrays which consist of Cu_2O precipitates and connecting dislocations which form a unique dislocation cell-like microstructure spaced $\sim 2 \mu\text{m}$. The optical metallographic image insert in Fig. 7 corresponds to the horizontal plane arrays shown in Fig. 6 for the associated mesh and foam open cellular structures. The centers of these cell-like arrays (shown in Fig. 7) exhibit a homogeneous distribution of vacancies created by the thermal quench (or rapid cooling) associated with the build process.

The initial powder microindentation hardness was measured by placing the powder in a mounting material and grinding, polishing, and etching powder cross-sections. The average hardness was measured as HV 72 (0.72 GPa). Correspondingly, the residual microindentation hardness for the solid (8.02 g/cm^3) specimen in a horizontal plane perpendicular to the build direction was HV 85 (0.85 GPa), an 18% increase. The mesh strut and foam ligament hardnesses (Fig. 6) were measured to average HV 161 (1.61 GPa) and HV 70 (0.70 GPa) for all orientations for each, respectively. The microindentation hardness for annealed Cu nominally ranges from HV 55 to HV 60, while heavily deformed Cu can have a microindentation hardness of $\sim \text{HV } 115$ (1.15 GPa) [11]. Considering that yield stress is estimated as $\sim \text{HV}/3$, the creation of a Cu_2O microstructure in EBM-fabricated Cu mesh and foam components contributes to improved strength, both in tension and compression for the open cellular structures.

Fig. 8(a) compares the measured stiffnesses or Young's moduli (E) versus their corresponding densities for the reticulated mesh and stochastic foam samples (Figs. 3–5). Similarly, Fig. 8(b) compares the relative stiffnesses (E/E_0) versus the relative densities (ρ/ρ_0) for the Cu samples (mesh and foam) with copper foams

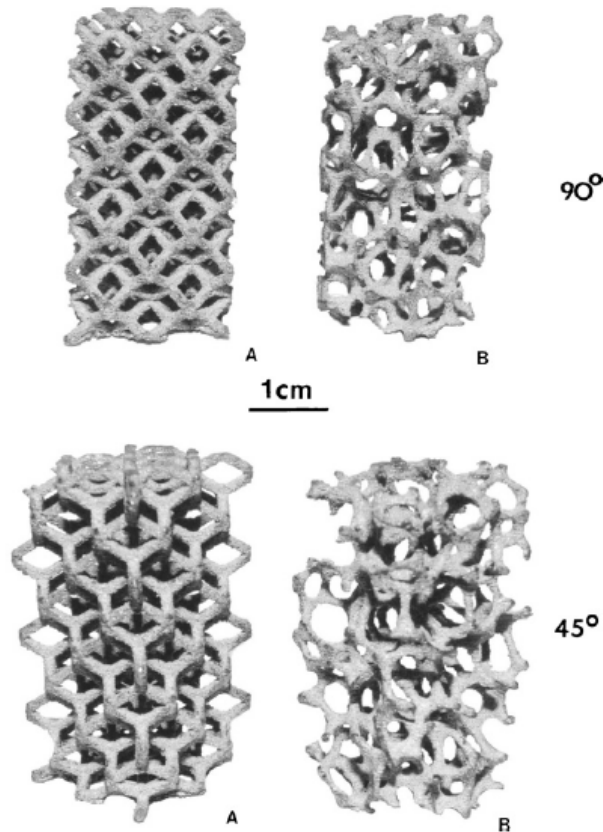


Fig. 4. Comparison of non-isotropic geometry for reticulated mesh (a) and isotropic stochastic, open cellular foam samples (b): at 90° (normal face view) and 45° (along sample diagonal), all fabricated by EBM. Corresponding densities are 1.2 g/cm³ (a) and 1.28 g/cm³ (b).

prepared by a lost carbonate sintering (LCS) process in powder metallurgy [8], and measured values for Ti–6Al–4V mesh and foam samples fabricated by EBM as illustrated in this study, using the same build elements [1,9]. The extrapolated intercept for E to a density (ρ_0) of 8.9 g/cm³ for the open cellular Cu samples in Fig. 8(a) corresponds to $E_0 = 110$ GPa. The corresponding values for E_0 and ρ_0 for the Ti–6Al–4V were 110 GPa and 4.43 g/cm³, respectively [1,9]. The slopes for these comparative mesh and foam plots (Fig. 8(b)) are illustrated in contrast to the idealized slope for stochastic, open cellular foams in Eq. (1), where $n = 2$. The Cu slopes correspond to $n = 2$ for the reticulated mesh samples and $n = 2.4$ for the stochastic foams, respectively. However, the LCS Cu foam data correspond to a slope of ~ 1.2 , well below the range for the open-cellular Cu structures fabricated by EBM in this work and the lower range of slopes (~ 1.8) for many other more conventional foams [2,6]. The fitted line for both the Ti–6Al–4V mesh and foam samples corresponds to a slope of $n \cong 2.2$. The Ti–6Al–4V data plotted in Fig. 8(b) from Murr et al. [1,9] was also supplemented by data for an additional mesh and foam sample ($\rho = 0.67$ and 1.56 g/cm³, respectively) in this work to serve as a calibration (reference) for the Cu stiffness measurements. Note that the slope lines for the different open cellular materials in Fig. 8(b) are offset. This results from different structure–property relationships [2,6], and is especially notable for the comparative EBM and LCS-fabricated Cu samples in Fig. 8(b).

Figs. 3 and 8(a) illustrate the ability to fabricate Cu open cellular structures with densities as low as 0.73 g/cm³, and prospects for much lower densities are tractable. In addition, the AM process using EBM allows for the fabrication of complex monolithic products consisting of graded or integrated mesh and/or foam

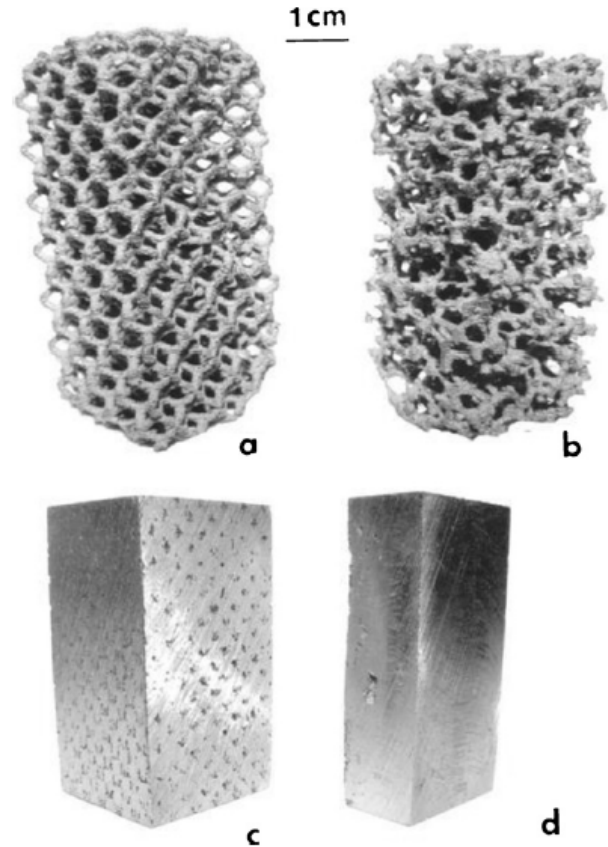


Fig. 5. Comparative reticulated mesh samples (a) and (c), stochastic, open cellular foam (b), and "solid" build (d). Corresponding densities are: (a) 2.18 g/cm³; (b) 1.70 g/cm³; (c) 6.67 g/cm³; (d) 8.02 g/cm³. All sample examples shown were fabricated by EBM.

components joined to various solid structures (e.g. face-sheets). These produce multi-functional micro-truss/ligament sandwich or related multi-functional micro-truss/ligament sandwich or related multi-component assemblies, especially complex heat exchange devices and related thermally engineered materials structures. For mesh or foam structures, conductive pathways through the strut or ligament architectures (including of course the strut or ligament cross-section geometries and dimensions) also determine their buckling or collapse under stress. Ashby et al. [2] have demonstrated a simple functional relationship between the thermal conductivity and the relative density of a metal foam in the form:

$$K_s \left(\frac{\rho}{\rho_0} \right)^{1.8} < K_f < K_s \left(\frac{\rho}{\rho_0} \right)^{1.65} \quad (3)$$

where K_s and K_f are the solid (fully dense) material thermal conductivity and foam conductivity, and ρ/ρ_0 is the relative density illustrated in Fig. 8. In addition, heat transfer by metal foams due to thermal dispersion effects is proportional to the cell size [12]. The thermal conductivity is also proportional to the electrical conductivity, and scales linearly with absolute temperature [13]. Consequently, open cellular structures of Cu have one of the highest conductivities: both thermal and electrical, and are specially suited for electronic thermal management systems.

Fig. 9(a) and (b) illustrates the Cu open cellular strut and ligament microstructures which show considerable micro-roughness as a consequence of unmelted and sintered surface particles. The inserts in Fig. 9(a) and (b) illustrate typical mesh strut and foam ligament cross-sections, respectively. Heat transfer media perfor-

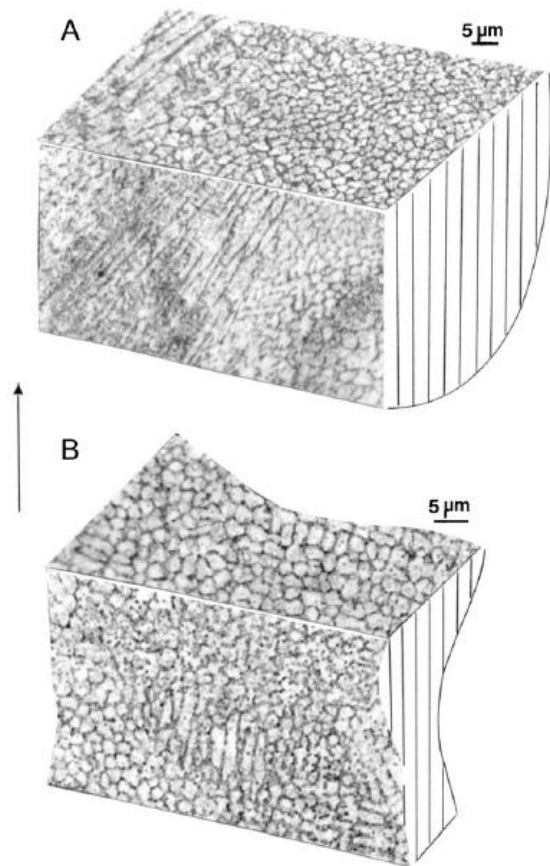


Fig. 6. Horizontal and vertical plane constructions typical of reticulated mesh strut microstructure (a) and stochastic foam ligament microstructure. The build direction is shown by the arrow (left).

mance (heat transfer rate) relating to a pressure drop in these open cellular structures will be highly dependent upon the pore size and the strut or ligament surface roughness. However, the surface structure illustrated in Fig. 9(a) and (b) will also increase the surface

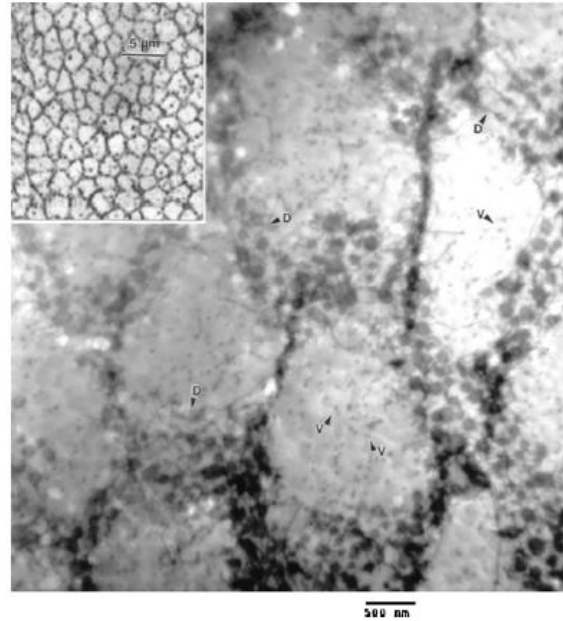


Fig. 7. TEM bright-field image for horizontal plane microstructural arrays observed in the "solid" sample in Fig. 5(d) (8.02 g/cm³) showing Cu₂O precipitate and dislocation cell-like microstructures. The insert shows a corresponding horizontal plane view of these microstructural arrays observed by optical metallography. Vacancies or vacancy dislocation loops are noted by arrows (V), while dislocations intermixed with the Cu₂O precipitates are noted by arrows labeled (D).

area and thereby improve heat transfer. In practice, these issues may also be influenced by cell crushing due to strut or ligament collapse which can be catastrophic for brittle materials. Fig. 9(c) and (d) illustrate a relatively classical ductile behavior for these Cu mesh and foam structures under impact – shear type failure; using a modified Charpy test system. While ductile dimple fracture features dominate, these are regions of simple separation of unmelted, unsintered, or poorly sintered particles. It can also be noted that the ductile dimple/shear dimple spacing averaged ~2 μm, consistent with the Cu₂O/dislocation array spacing shown in Figs. 5–7.

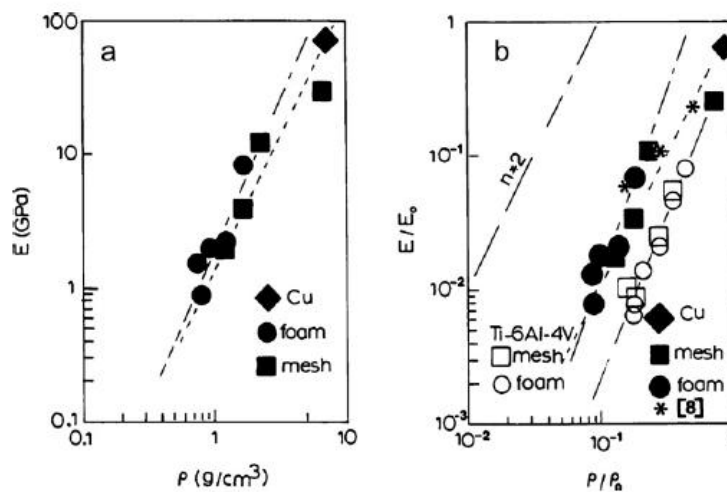


Fig. 8. Stiffness (E) versus density (ρ) for Cu (a), and relative stiffness (E/E_0) versus relative density (ρ/ρ_0) for Cu and Ti-6Al-4V (b). A portion of Ti-6Al-4V data in (b) is from Murr et al. [1]. The solid diamond represents the solid sample shown in Fig. 5(d).

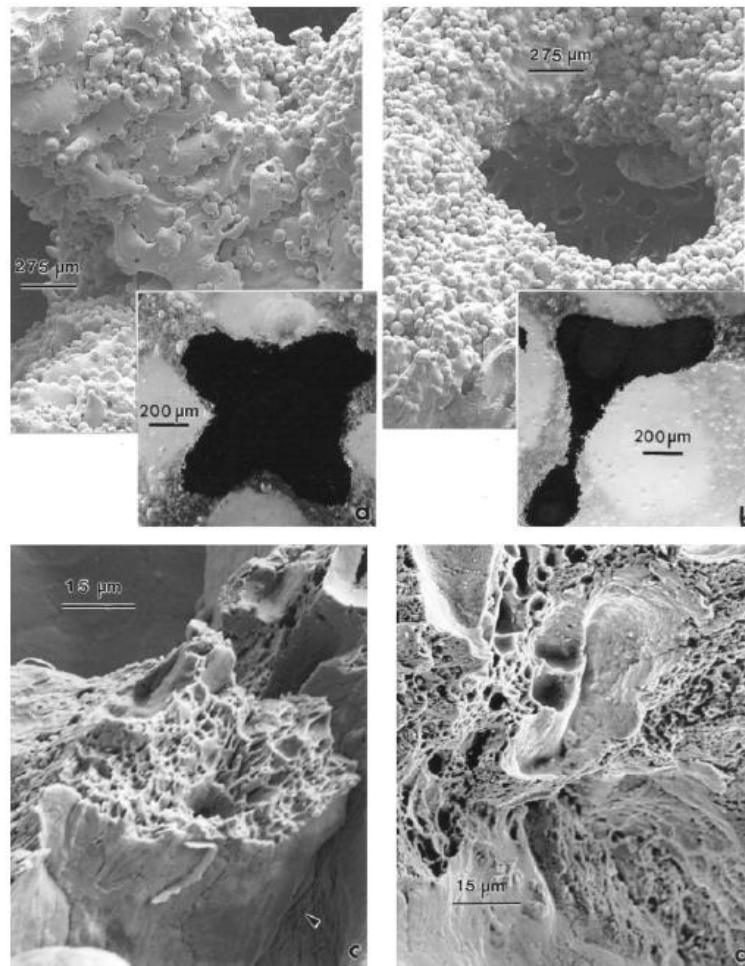


Fig. 9. SEM image comparison for a reticulated mesh strut microstructure (a) and stochastic open cellular foam ligament microstructure (b). Inserts in (a) and (b) show strut and ligament cross-sections viewed by optical metallography. (c) and (d) show impact-shear fractography views for mesh strut and foam ligament fracture surfaces, respectively.

4. Conclusions and summary

In this study we have fabricated open cellular structures – reticulated meshes and stochastic foams by AM using EBM from precursor Cu powder – containing Cu_2O precipitates. These precipitates and additional precipitates created in the EBM melt scan formed microstructural arrays which contributed to hardening contributing to the strength of mesh struts and foam ligaments. The stiffness or Young's moduli for these Cu open cellular structures vary with density, and relative stiffness versus relative density plots for Cu compared very closely with EBM fabricated Ti–6Al–4V open cellular structures – both mesh and foams. The Cu reticulated mesh structures exhibited a slope of $n=2$ in contrast to a slope of $n=2.4$ for the stochastic Cu foams, consistent with the ideal, open cellular foam slope of $n=2$ for the Gibson–Ashby foam model [6].

The ability of AM-EBM to fabricate complex monolithic structures and devices composed of various open cellular structures and sandwich or other conformal compartmentalization suggests a wide range of thermal management or heat exchange applications. This is a consequence of the superior thermal and electrical conductivity of Cu and its considerably higher operating temperature in contrast to Al or Al alloys.

Acknowledgements

This research was supported by Mr. and Mrs. MacIntosh Murchison Endowments at the University of Texas at El Paso. Support for research at the Institute of Metal Research, Shenyang, China was provided by the Chinese Academy of Science (CAS). We are also grateful to Pedro Frigola, Radiabeam Technologies, Santa Monica, CA for the provision of the Cu powder.

References

- [1] L.E. Murr, S.M. Gaytan, F. Medina, H. Lopez, E. Martinez, B.I. Machado, D.H. Hernandez, L. Martinez, M.I. Lopez, R.B. Wicker, J. Bracke, *Philos. Trans. R. Soc. A* 368 (2010) 1999–2032.
- [2] M.F. Ashby, A. Evans, N.A. Fleck, L.J. Gibson, J.W. Hutchinson, H.N.G. Wadley, *Metal Foams: A Design Guide*, Butterworth-Heinemann, Boston, MA, 2000.
- [3] K. Boomsma, D. Poalidakos, F. Swick, *Mech. Mater.* 35 (2003) 1161–1176.
- [4] T.J. Lu, H.A. Stone, M.F. Ashby, *Acta Metall.* 46 (10) (1998) 3619–3635.
- [5] See Metafoam (Metal foam manufacturer) and Mitsubishi Materials Corp. (Japan) for example.
- [6] L.J. Gibson, M.F. Ashby, *Cellular Solids: Structure and Properties*, Cambridge University Press, New York, 1997.
- [7] X.F. Tao, L.P. Zhang, Y.Y. Zhao, *Mater. Sci. Forum* 539–543 (2007) 1863–1867.
- [8] M.A. El-Hadek, S. Kaytbay, *Int. J. Mech. Mater. Res.* 4 (2008) 63–69.
- [9] L.E. Murr, S.M. Gaytan, F. Medina, E. Martinez, J.L. Martinez, D.H. Hernandez, B.I. Machado, D.A. Ramirez, R.B. Wicker, *Mater. Sci. Eng. A* 516 (2009) 205–216.

- [10] D.A. Ramirez, L.E. Murr, E. Martinez, D.H. Hernandez, J.L. Martinez, B.I. Machado, F. Medina, R.B. Wicker, P. Frigola, Novel-precipitate-microstructural architecture developed in the fabrication of solid copper components by additive manufacturing using electron beam melting, *Acta Mater.*, in press.
- [11] J.C. Sanchez, L.E. Murr, K.P. Staudhammer, *Acta Mater.* 45 (8) (1997) 3223–3235.
- [12] M.L. Hunt, C.L. Tien, *Int. J. Heat Mass Transfer* 31 (1988) 301–309.
- [13] X. Ma, A.J. Peyton, Y.Y. Zhao, *NDT E Int.* 24 (5) (2006) 447–450.

Curriculum Vita

Diana A. Ramirez was born in Chihuahua, Chihuahua Mexico and is the oldest daughter of Maria Del Rosario Olivas and Luis A Ramirez. She enrolled at the College of Engineering affiliated to the University of Texas at El Paso (UTEP), El Paso TX, USA in August 2003, where she obtained a Bachelor of Science in Metallurgical and Materials Engineering in August of 2008.

As an undergraduate student, she worked as research assistant for the Department of Metallurgical and Materials Engineering working on various projects. She also had a co-op with Chaparral Steel in 2006 and an internship with GM Powertrain Foundry in 2007. She decided to pursue higher education and remained at The University of Texas at El Paso where she joined the Fast Track Materials Science and Engineering (MASE) interdisciplinary program under the guidance of Dr. L.E. Murr in 2008.

She has been achieved numerous honors and awards such as Murchison Graduate Engineering Scholarship and the John R. Serrano Memorial Endowed Copper Research Award and APO (Alpha Pi Omega) Outstanding Engineering Award – Walter Roser Award. She was also a recipient of the Graduate Engineering Scholarship and the SHPE AHETEMS Scholarship in 2008. She has been part of Alpha Sigma Mu Metallurgical and Materials Engineering Honor Society since 2007 and Materials Advantage Society (TMS), Mexican American Engineers and Scientist Society of Hispanic Professional Engineers (MAES/SHPE), and American Foundry Society (AFS).

While pursuing her degree, she worked as a research assistant for the department of Metallurgical and Materials Engineering. She has presented her research in different international conferences. In 2010, she presented her research in the SFF International Conference in Austin TX and the MS&T Conference in Houston, TX and TMS in Seattle, WA and presented as well in the 2011 TMS Conference in San Diego CA. She has published several papers such as “Novel Precipitate – Microstructural Architecture Developed in the Fabrication of Solid Copper Components by Additive Manufacturing Using Electron Beam Melting” and “Open-cellular copper structures fabricated by additive manufacturing using electron beam melting”.

Permanent address: 1474 Pin Cushion

El Paso, TX, 79928

This dissertation was typed by Diana A. Ramirez.